Vapor phase hydrodeoxygenation of lignin-derived phenolic monomers to aromatics on transition metal carbides under ambient pressure

A DISSERTATION

SUBMITTED TO THE FACULTY OF

UNIVERSITY OF MINNESOTA

BY

Cha-Jung Chen

IN PARTIAL FULFILLMENT OF THE REQUIREMENTS

FOR THE DEGREE OF

DOCTOR OF PHILOSOPHY

Advisor: Aditya Bhan

August 2016

© Cha-Jung Chen 2016
ALL RIGHTS RESERVED

Acknowledgements

It has been an amazing experience pursuing my PhD at the University of Minnesota-Twin Cities, and at the CEMS department. This journey has been challenging, unexpected, and fun. With the abundant resources the community has given, I have become a researcher I am today.

The constant guidance and rigorous training in critical thinking, research, and presentation from my advisor, Aditya Bhan, are invaluable to me. His commitment and dedication to science has inspired me to not give up in the face of challenges and uncertainty. I would like to thank the enormous support from the Bhan group members: Rachit Khare, Minje Kang, Joseph DeWilde, Mark Sullivan, Udit Gupta, Linh Bui, Andrew Hwang, Anurag Kumar, Sukaran Arora, Brandon Foley, Jake Miller, Dr. Mark Bachrach, and Dr. Praveen Bollini. I also enjoyed working with former Bhan group members: Dr. Mark Mazar, Dr. Dario Prieto-Centurion, Dr. Samia Ilias, Dr. Jeremy Bedard, and Dr. Elizabeth Mallon. I really appreciate Dr. Hsu Chiang for answering all my questions before I decided to join the CEMS community; it made the decision making process a lot easier. Special thanks to Dr. Ian M. Hill, Dr. Srinivas Rangarajan, and Dr. Wen-Sheng Lee for introducing me to new research topics and sharing valuable experiences with me.

My time here would not be as colorful without the support and care from my friends at the CEMS department. I will miss my lunch time discussions with Stacey Saba under the sun. I enjoyed all the cuisine related activities and conversations with Jeff Peterson and Thu Le Tran. It has been a wonderful experience working with Alyssa McKenna in the CEMS Women's Group; her aspiration to achieve more for the student group has been a true inspiration for me. The authentic pasta that Maria McClintock shared with me was savory and delicious. My appreciations to many others who have touched my heart and have given me a hand are beyond words.

The support from my friends and relatives in Taiwan, Australia, and the US has been an anchor for me. With their understanding and encouragement, I have become stronger

and more courageous than ever. Special thanks to Ching-Yu Chen, Daphne Lin, Susan Hsu, and Dr. Yuan for always being there for me.

I am grateful for the love and support from my parents and siblings. Although we are ~12,000 km apart, our bonds have grown closer in the past years. The smiles and kisses from my nieces, Maggie Hsu and Claire Hsu, have been the best energy booster for me! I feel privileged to have my in-laws be part of this journey; thank you for being part of my family.

Last but not least, my husband, Chen-Yu Liu, has been an incredible partner and my best friend; thank you for embracing me as an independent individual. We grow and learn through the journey together, and we work wonderfully and efficiently in the kitchen where we make healthy and delicious meals, and many heavenly tasty desserts. I look forward to our life-long journey as soul mates.

To my husband, Chen-Yu Liu, and my family: Grandma Lin, Daniel Chen, Linna Lin, Sarah Chen, Sasha Chen, and Anita Chen.

Abstract

Lignin is a sustainable source to produce aromatics such as benzene, toluene, and xylenes (BTX). Vapor phase hydrodeoxygenation (HDO) of depolymerized lignin monomers can directly upgrade pyrolysis vapor without processing corrosive and viscous bio-oil. Selective cleavage of Ar–O bonds, however, is challenging because Ar–O bonds are strong (422-468 kJ mol^{-1}). Severe reaction conditions of high H_2 pressure (~1–5 MPa) and high temperatures (~473–723 K) thus limit the yields of BTX from HDO of lignin pyrolyzates by successive hydrogenation of the aromatic ring or direct hydrogenolysis of C–C bonds. This dissertation reports kinetics, mechanism, and in situ chemical titration studies on HDO of lignin-derived phenolic compounds on molybdenum and tungsten carbide formulations for selective synthesis of benzene and toluene under ambient H_2 pressure and low temperatures (420–553 K).

High aromatics yield (>90%, benzene and toluene) was obtained from vapor phase HDO of phenolic compound mixtures containing m-cresol, anisole, 1,2-dimethoxybenzene, and guaiacol over Mo_2C under atmospheric pressure at 533–553 K, even with H_2 to phenolic compound molar ratios of ~3,300. Toluene selectivity increased proportionately (4%–66%) to m-cresol content in HDO of phenolic compound mixtures (molar composition: 0%–70%) at quantitative conversion. Low selectivity to cyclohexane and methylcyclohexane (<10%) across the conversions investigated (18–94%) demonstrates that undesired successive hydrogenation reactions of aromatics over Mo_2C were inhibited, presumably due to in situ oxygen modification, as inferred from titration studies of aromatic hydrogenation reactions using methanol and water as titrants.

Kinetic studies of anisole and m-cresol HDO on molybdenum and tungsten carbide formulations show that high benzene and toluene selectivity (>80% C_6^+ selectivity) are a result of selective cleavage of aromatic-oxygen bonds (Ar–OH and Ar–OCH_3). The same reactant dependencies, zero order on oxygenate pressure and half order on H_2 pressure, for both benzene and toluene synthesis from anisole and m-cresol HDO, respectively, demonstrates that two distinct sites are involved in HDO of phenolic compounds on

molybdenum and tungsten carbides. In situ CO titration studies under reaction conditions showed that metallic sites are required for selective HDO of phenolic compounds.

Oxygenate-modified Mo_2C catalysts were prepared by pretreating fresh Mo_2C catalysts in 1 kPa of O_2, H_2O, and CO_2 at 333 K and were employed to study the effect of oxygenate-modification on the metal-like function of Mo_2C using m-cresol HDO as a probe reaction. Molecular oxygen was found to have a higher propensity to deposit oxygen (O/Mo_{bulk} before HDO = 0.23 ± 0.02) on fresh Mo_2C compared to CO_2 and H_2O (O/Mo_{bulk} before HDO ~ 0.036) as assessed from temperature-programmed surface reactions with H_2 before m-cresol HDO. Oxygen adsorbed in amounts exceeding ~ 0.06 ± 0.01 of O/Mo_{bulk} was found to poison the active sites for toluene synthesis and the effect of adsorbed oxygen on turnover frequency of toluene synthesis was found to be agnostic to the source of oxygen, as inferred from in situ CO titration and m-cresol HDO reactions on fresh and oxygenate-modified Mo_2C catalysts.

Table of Contents

List of Tables

List of Figures

.

List of Schemes

1. Introduction

1.1. Motivation*

Transition metal carbides that have been shown to catalyze hydrogenolysis,[1,2] hydrogenation,[2–8] and isomerization[9–12] reactions and to exhibit both metallic and acidic characteristics are now finding applications in electrocatalytic hydrogen evolution (HER)[13–15] and hydrodeoxygenation (HDO) of biomass-derived oxygenates to fuels and chemicals.[16–26] These interstitial compounds[27] display extensive non-uniformities, including distinct binding sites,[28–33] thermodynamically stable surfaces with varying terminations,[34] and non-stoichiometric compositions in the ratios of transition metal, C, and O both in the bulk and surface structures[8,35] (Scheme 1.1) as evinced by spectroscopic and mechanistic studies of specific reaction systems, ultra-high vacuum surface science studies, and computational calculations. HDO of lignocellulosic or triglyceride-based biomass requires selective cleavage of strong carbon-oxygen bonds (>385 kJ mol^{-1})[36] without successive hydrogenation and/or undesired C-C scission. Severe reaction conditions such as high temperature (~700 K) and high hydrogen pressures (1–10 MPa) are often employed for HDO reactions using noble metal catalysts, resulting in the loss of carbon and/or excess use of hydrogen in concurrent decarboxylation, hydrogenation, and hydrocracking reactions.[36–39] The co-existence of metallic and acidic functionalities on transition metal carbides is attractive for HDO as it has been noted that the presence of oxygen on/in carbides can simultaneously inhibit the metallic function and enhance acidic character,[7,10–12,40] which potentially allows for selective deoxygenation at ambient pressure and low temperatures (420–553 K).

*Reproduced from Catal. Sci. Technol., 2016, 6, 602-616, with permission from the Royal Society of Chemistry.

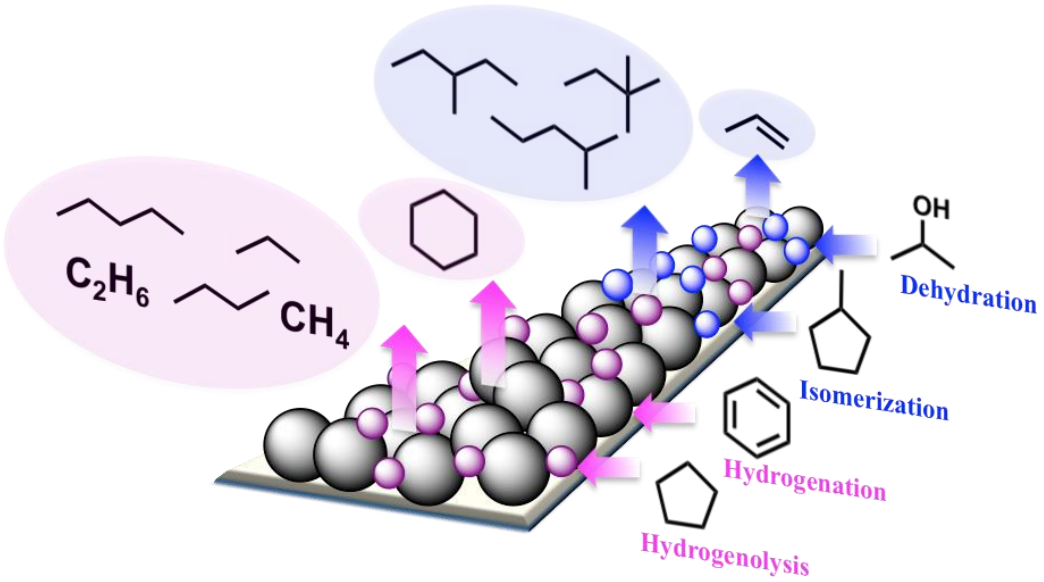

Scheme 1.1 Catalytic reactions – including hydrogenolysis, hydrogenation, isomerization, and dehydration – that are catalyzed by carbidic and oxycarbidic molybdenum carbide formulations

HDO of phenolic compound mixtures on Mo_2C catalyst is reported in Chapter 3 in which titration studies using methanol and water as titrants were employed to probe the effect of in situ oxygen modification on Mo_2C for hydrogenation reactions. The kinetics of anisole HDO on Mo_2C and W_2C are presented in Chapter 4 in which in situ CO titration technique was used to investigate the site identity and density. The effect of oxygenate modifications on the metal-like function of Mo_2C using m-cresol as a probe reaction is addressed in Chapter 5. I have also studied the kinetics and thermochemistry of olefin cracking on H-ZSM-5 in earlier part of my PhD, and this work is reported in Chapter 2.

1.2. Background

1.2.1. Transition metal carbides: synthesis and structure

Self-supporting and high surface area (60–100 m^2 g^{-1}) molybdenum carbide catalysts can be prepared via temperature programmed reaction (TPR) method developed by Boudart and coworkers.[41] This method involves treating a Mo-oxide precursor under continuous flow of H_2 and hydrocarbon with differing compositions during which varying temperature ramp rates up to 1023 K are employed.[7,41] Self-supporting tungsten carbides can be synthesized from W-oxide precursors by TPR method using similar H_2/hydrocarbon flow conditions with higher final synthesis temperatures (1000–1200 K).[42–44] The surface area for WC_x (~15–30 m^2 g^{-1}), however, is typically lower than molybdenum carbides.[42–44]

The surface composition of the resulting molybdenum carbides vary with the thermodynamic potential of the synthesis gas mixture, which can result in surface carbon deposition or the formation of metallic Mo due to over-reduction.[41] Djéga-Mariadassou et al.[7] have also noted the challenges of synthesizing phase-pure carbides without residual oxygen as the reductive H_2 atmosphere cannot completely remove oxygen from the oxide precursor. The stable surface structure of molybdenum carbide formulations also vary with the carburizing potential of the synthesis gas environment, demonstrated by Wang et al.[34] using DFT calculations for orthorhombic Mo_2C. Surfaces with mixed Mo/C termination are noted to be favored over Mo-terminated surfaces under high carburizing potential.[34] Ribeiro, Iglesia, and Boudart have also reported the existence of carbon deficient centers, surface carbon, and a diversity of oxygen-binding sites on tungsten carbides.[10–12] These reports demonstrate that the bulk and surface structure of transition metal carbides are a function of synthesis or reaction conditions.

Transition metal carbides synthesized via TPR method in the H_2/hydrocarbon flow are oxophilic and pyrophoric in nature. Passivation of these carbides, freshly synthesized and/or spent but treated in a reducing environment, is required prior to ex situ characterization studies.[2,27,41,45] Passivation is typically carried out in dilute O_2 flow to prevent bulk oxidation and the bulk crystal structure is reported to retain on the passivated catalysts as evidenced by X-ray diffraction.[7,46] The carbidic surface, however, is oxidized

by passivation treatments as demonstrated by the inhibited benzene hydrogenation rate on a passivated Mo_2C,[7] and the similar point of zero charge measured on a passivated Mo_2C and a MoO_2 (~ pH 3; fresh Mo_2C ~ pH 5).[46] The surface composition and structure of molybdenum and tungsten carbides under reaction conditions therefore, cannot be ascertained using ex situ surface characterization methods.

1.2.2. The effects of water on molybdenum carbide catalysis*

Water is ubiquitous in upgrading biomass to fuels and chemicals as bio-oil contains ~30 wt% of H_2O, and oxygen contained in biomass derivatives formed upon depolymerization/deconstruction of lignocellulosics is removed as water in HDO chemistries.[47] The stability and activity of molybdenum carbides during deoxygenation reactions in the presence of water, therefore, are important.

DFT studies have shown that H_2O can dissociate to OH* and H* (* represents an adsorption site), which can further dissociate to form O* and 2H* on β-Mo_2C(001),[48–50] consistent with the experimentally measured near zero order dependences on H_2O pressures for water-gas shift (WGS) over bulk Mo_2C.[51] Namiki et al.[52] demonstrated the dissociation of H_2O on carburized 4.8 and 8.5 wt% Mo/Al_2O_3 catalysts during WGS reaction, in which H_2, $^{13}C^{18}O$, $^{13}C^{18}O_2$ and $^{13}C^{18}O^{16}O$ were observed via mass spectrometry upon pulsing $H_2{}^{18}O$ into a continuous stream of ^{13}CO in He at 423 K. Ren et al.[19] showed using DFT calculations that adsorbed oxygen from oxygenates (O*) can be removed from a Mo_2C(0001) surface in presence of excess H_2 as hydrogen can dissociate onto an O*-occupied Mo_2C site to form OH*, which can subsequently react with another OH* to remove the adsorbed oxygen by forming H_2O* and O*, however, the activation barrier for OH* coupling is ~110 kJ mol^{-1}. Thermodynamic calculations show that $Mo_2C_{(s)}$ can be oxidized by both $H_2O_{(g)}$ and $H_2O_{(l)}$ to form MoO_2 ($\Delta G_{rxn,\ 573\ K}$ ~ -20 and ~ -130 kJ mol^{-1}, respectively), however, the oxidizing strength of O_2 ($\Delta G_{rxn,\ 573\ K}$ ~ -1300 kJ mol^{-1}) is much stronger than that of H_2O.[47,53]

*Reproduced from Catal. Sci. Technol., 2016, 6, 602-616, with permission from the Royal Society of Chemistry.

It has been reported that adsorbed oxygen on Mo_2C formulations, from oxygen-containing compounds including water, methanol, lignin-derived phenolics, or O_2, diminishes metallic functions[54,55] and generates acidic sites.[56] Hydrogenation rates of benzene and toluene on a passivated Mo_2C formulation that was H_2-treated at 573 K for 1 h prior to the reaction were completely inhibited in presence of a water co-feed, showing that the introduction of water to molybdenum carbide formulations can irreversibly inhibit the metallic hydrogenation function.[55] In situ synthesized Mo_2C was treated in 10 kPa of H_2O for 2.5 h before exposing the sample to isopropanol (IPA)/CH_4/He mixtures (1/3.5/Bal %) at 415 K and ambient pressure; dehydration rates to form propylene increased fourfold while the formation rates of C_6^+, which are metal/base catalyzed products, decreased by half compared to a fresh Mo_2C that had not been exposed to H_2O or O_2.[56] The effect of water treatment, however, is less severe than that noted upon exposing a fresh Mo_2C sample to O_2 (~13 kPa), which is accompanied by a temperature exotherm of ~100 K and concurrent elimination of C_6^+ formation rates in less than 20 min.[56] An independent experiment of 0.5 kPa IPA dehydration with 0.7 kPa of H_2O and 13.5 kPa of O_2 co-feed on a fresh Mo_2C demonstrated that water co-feed has no kinetic effects on IPA dehydration,[56] which is consistent with the reported involvement of Brønsted acid sites generated on Mo_2C upon O_2 exposure.[56] The effect of water co-feed is minimal as oxygen co-feed (~13.5 kPa) is the dominating contributor to the formation of Brønsted acid sites for IPA dehydration. The negligible effect of H_2O on IPA dehydration is also consistent with the experimentally measured zero order dependencies on IPA;[56] the IPA-saturated Mo_2C surface (0.5 kPa) shows negligible IPA dehydration inhibition from a comparable water co-feed pressure (0.7 kPa), implicating that O*-induced Brønsted acid sites favor IPA adsorption over H_2O. Along the same lines, 31.8 mol % of water was co-fed with 5.7% CO during WGS reaction at atmospheric pressure between 493 K to 568 K; no deactivation of Mo_2C was observed for at least 48 h on-stream, and Mo_2C phases remained in the bulk structure as no oxide phases were observed from XRD patterns of the spent catalysts.[57,58] The negligible deactivation effect of water on WGS reaction reported by Moon and coworkers[57,58] is presumably ascribed to the surface dominating O* species derived from

H_2O dissociation[48–51] participating in the catalytic cycle as has also been suggested by DFT calculations on β-Mo_2C(001)[50] and by the near zero H_2O pressure dependency measured experimentally.[51]

The inhibitive effect of water on aromatic hydrogenation is analogous to the oxidation-induced suppression of hydrocarbon hydrogenolysis and contrasts the case studies on IPA dehydration and WGS reactions in which oxygenates are involved as reactants/products. We postulate that a more carbidic and less oxidized surface is required for catalytic hydrogenation and that reactant feeds devoid of oxygenates are necessary to retain this carbidic surface; adsorbed oxygen alters the surface stoichiometry and electronic structure, thereby altering the adsorption properties of hydrocarbon reactants such as benzene and toluene. This oxidation-induced inhibition of hydrocarbon hydrogenation was also noted by Choi et al.[7] when studying the effect of carburization on benzene hydrogenation. The inhibitory effect of adsorbed oxygen on aromatic hydrogenation in conjunction with the selective Ar–O cleavage of O*-modified Mo_2C formulations result in the high selectivity of aromatics (>90%) in hydrodeoxygenation of lignin-derived phenolic compounds.[55]

Hydrothermal stability and activity of Mo_2C formulations for aqueous-phase hydroprocessing of acetic acid were studied extensively by Choi et al.[59] The bulk structure of molybdenum carbide formulations remained as hcp Mo_2C after hydrothermal treatment in liquid water under N_2 at 523 K and ~47 bar for 48 h, demonstrating that molybdenum carbide structures are resistant to bulk oxidation at high pressure liquid water conditions. Surface oxidation of the samples, however, was confirmed by XPS studies as the percentage of Mo 3d in Mo–O form increased fourfold after the hydrothermal treatment. Similar surface oxidation results were observed for a fresh Mo_2C tested for hydroprocessing (10% guaiacol in H_2O at 523 K and ~137 bar), suggesting that the oxidative effects of the guaiacol solution on the Mo_2C surface are comparable to that of pure water. Hydrothermal aging has a minimal inhibitory effect for acetic acid conversion (10 w/w % in H_2O at 523 K and ~137 bar) to ethanol and ethyl acetate under hydroprocessing conditions; acetic acid conversion remained constant at ~40% when using

both a fresh carbide catalyst and a hydrothermally treated carbide catalyst. The authors also noted that structural and activity changes to molybdenum carbides due to hydrothermal conditions are sensitive to the original Mo_2C structure which mirrors the observed severe deactivation in HDO of phenol and 1-octanol on Mo_2C/ZrO_2 when 30% H_2O was co-fed.[53] The results for IPA dehydration, WGS reaction, and hydrodeoxygenation of acetic acid and guaiacol suggest that the surface modification of Mo_2C by O* is agnostic to the source of oxygen, namely phenolic compounds, fatty acids, alcohols, or water; these oxygenates can dissociate and leave behind O* on the surface, inhibiting the metallic function and potentially generating Brønsted acid sties. The major difference between the oxygen sources is that the oxidizing strength of O_2 is much stronger than other oxygenates as demonstrated by the thermodynamic favorability of $Mo_2C_{(s)}$ oxidation using O_2 in reference to H_2O as discussed above.

2. Kinetics and thermochemistry of C_4-C_6 olefin cracking on H-ZSM-5*

2.1. Introduction

Olefin cracking is ubiquitous in acid catalyzed reactions of olefins, which is important especially in processes that upgrade light olefinic gases to high-quality gasoline products such as Lurgi's Methanol to Propylene process[60] and the MOGD[61] (Mobil olefins-to-gasoline and distillate) process. Quann et al.[62] in studying light olefin (C_3-C_6) conversion on H-ZSM-5 over a temperature range of 477–655 K and a pressure range of 0.01-100 bar observed products ranging from C_5-C_{30}, showing the complexity of acid catalyzed reactions of olefins, which has been described by Pines[63] using the term "conjunct polymerization." Bessell and Seddon[64] noted that light olefin conversion on H-ZSM-5 occurred via successive isomerization, oligomerization, cracking of higher oligomers, and hydrogen transfer. Guisnet et al.[65] also found that 1-butene conversion on medium pore zeolites like H-FER, H-TON, H-EU-1 and H-MFI at 623 K is highly selective to iso-butene, propene and pentenes as a result of a sequence of oligomerization, isomerization, and cracking steps. These parallel reactions (Scheme 2.1a) have hence precluded detailed experimental kinetic studies of olefin cracking on acidic zeolites.

β-scission is the predominant mechanism for olefin cracking on solid acid catalysts.[66–69] It involves the protonation of an olefin to form an alkoxide intermediate with the framework oxygen atom; subsequently, the β C bond relative to the adsorbed carbon breaks to form a smaller olefin and a carbocationic hydrocarbon, which forms another olefin via one of three pathways (Scheme 2.2)[70]: (1) immediate hydrogen transfer back to the zeolite, (2) physisorption on the zeolite with subsequent hydrogen transfer, or (3) chemisorption followed by β-hydrogen elimination. A recent computational study that accounts for

*Reprinted with permission from ACS Catal., 2014, 4 (7), pp 2319–2327. Copyright 2014 American Chemical Society.

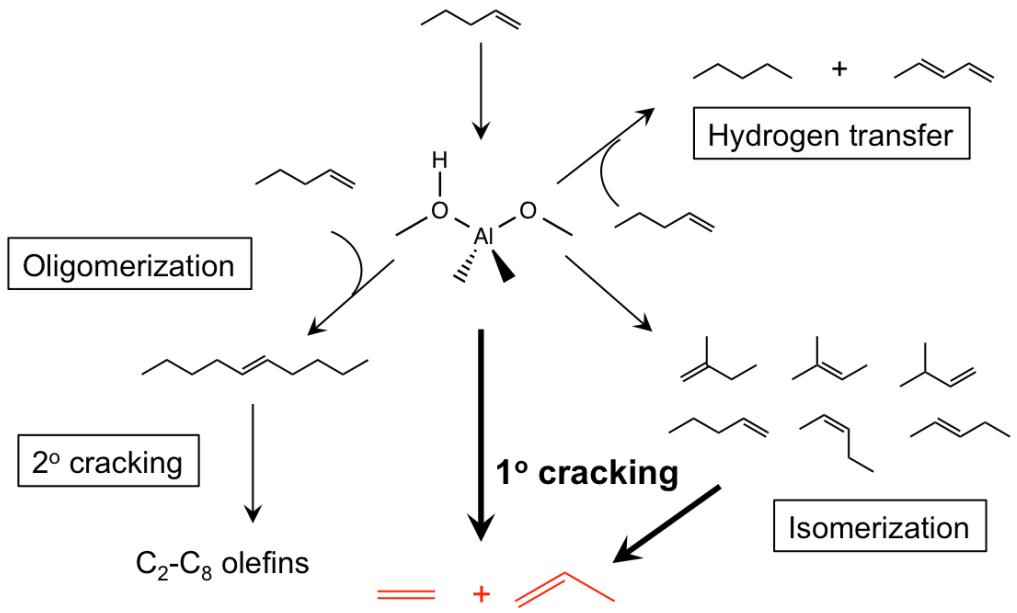

Cracking mode labels

A	3° → 3°
B_1	2° → 3°
B_2	3° → 2°
C	2° → 2°
D_1	1° → 2°
D_2	2° → 1°
E_1	1° → 3°
E_2	3° → 1°
*F	1° → 1°

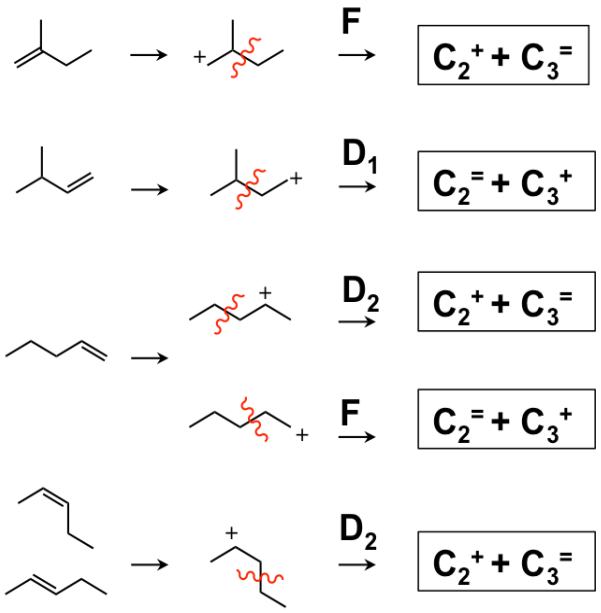

Scheme 2.1 (a) Olefin reactions on a zeolite acid site; (b) Modes of β-scission and their associated labels; (c) β-scission modes for pentene cracking. *Denotes undocumented label.

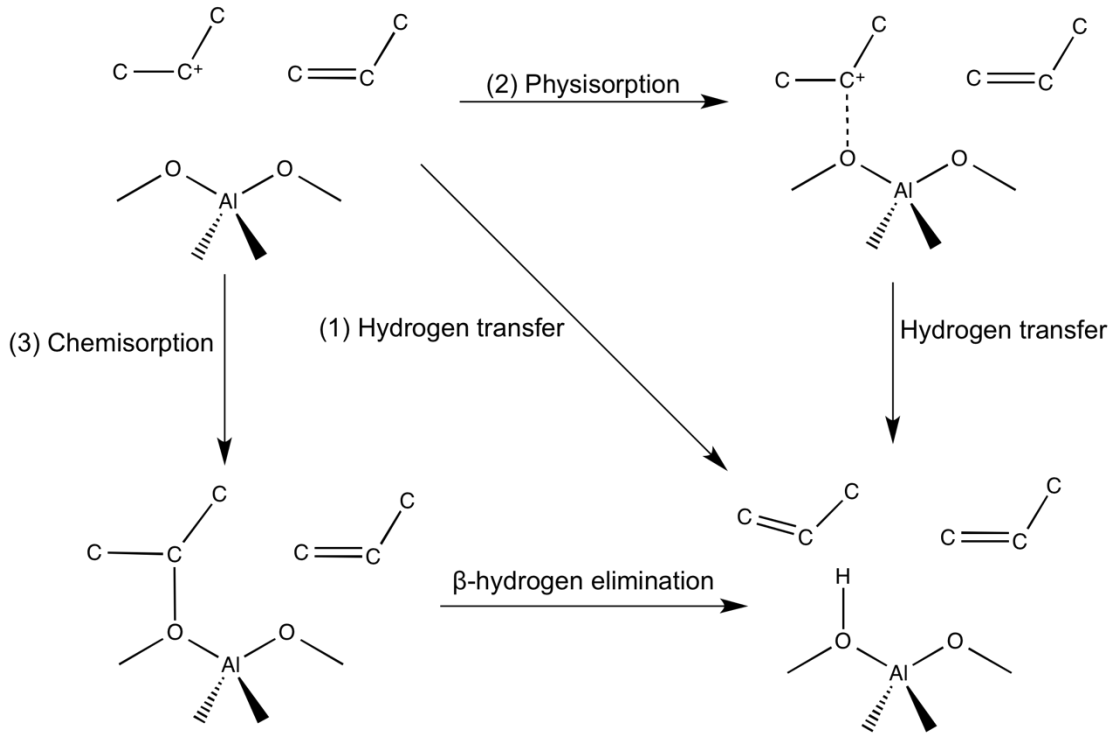

Scheme 2.2 Three pathways of forming olefin cracking products from the transition state of β-scission: (1) Direct hydrogen transfer; (2) Physisorption of β C, followed by hydrogen transfer; (3) Chemisorption of the β C, followed by β-hydrogen elimination. Reproduced from Mazar et al.[70] (copyright 2013 American Chemical Society)

dispersive corrections on an MFI supercell containing the full crystal structure shows that the transition state for β-scission occurs when the α C and β C are fully sp^2 hybridized.[70]

Weitkamp et al.[71] developed a nomenclature to describe the various modes of olefin cracking based on carbenium ion types involved in products and reactants when studying C_9-C_{16} n-alkane hydrocracking on Pt/H-ZSM-5. Buchanan et al.[72] extended this nomenclature (Scheme 2.1b: Nomenclatures include cracking mode A (the most substituted carbenium ions) to mode F (the least substituted ones).) in studying the relative rates of monomolecular alkene cracking for C_5-C_8 olefins on H-ZSM-5 at 783 K. Olefin isomerization was postulated to precede alkene cracking so an equilibrium distribution of alkene isomers was considered starting from an n-alkene feed. Relative rates of C_5: C_6: C_7: C_8 alkene cracking were evaluated to be 1: 24: 192: 603, which were rationalized on the

basis of carbenium ion stability wherein a more energetically favorable mode of cracking becomes available for larger olefins. Although larger hydrocarbons can access more stable transition states, we show here that adsorption constants of alkoxide intermediates that lead to these more stable transition states, however, are low, and the contribution of such modes may not be the predominant olefin cracking pathway (Section 2.3.4).

Intrinsic activation barriers for different β-scission modes were found to depend on the substitution order of the carbenium ions involved in the reactant and transition states.[70,72–75] Frash et al.[73] investigated β-scission mechanisms on zeolites using density functional theory (DFT) and ab initio Hartree-Fock calculations on 1T and 3T clusters and showed that the β-scission activation barrier of 2-pentoxide was 20.9 kJ mol^{-1} lower than that for 1-butoxide, indicating that the additional methyl group stabilizes the carbocationic transition state with respect to the reactant state. Mazar et al.[70] investigated β-scission modes A to E (Scheme 2.1b) for various C_6 and C_8 olefin isomers over H-ZSM-5 using dispersion-corrected density functional theory (PBE-D). The barrier heights for β-scission were found to monotonically increase with an increase of the change in the charge of the β C going from the physi- or chemisorbed reactant state to the transition state. Mazar et al.[70] also noted that the substitution order of the transition state has a greater influence on the intrinsic activation energy than the reactant state.

Gas-phase olefins were observed to undergo multiple protonation and deprotonation and hydride shifts (almost barrierless) or methyl shifts (intrinsic activation energy ~10 kJ mol^{-1}) before cracking into smaller olefins.[69,72,76] It has been shown both experimentally and computationally that hydride shifts of olefins on acid catalysts occur easier than methyl group migration, which is easier than direct branching rearrangements.[69,77–79] Buchanan et al.[69] studied 1-hexene (0.5 atm partial pressure) conversion on H-ZSM-5 and found that, at 589 K, 4% of the feed cracked to lighter olefins while 91% of 1-hexene converted into other C_6 isomers, with concentrations of linear hexenes being higher and of more branched isomers being lower than predicted gas-phase equilibrium calculations. Quann et al.[62] have also reported that the observed hexene isomer distribution when feeding 1-hexene at 500

K and low conversion (3%) on H-ZSM-5 deviated significantly from the predicted equilibrium distribution. The fast isomerization of olefins on acidic zeolites before cracking, therefore, does not guarantee a gas-phase equilibrium distribution among the isomers,[69,72,76,80] because size restrictions within microporous voids restrain the formation of certain branched molecules that are thermodynamically preferred.[62,69,80,81] Our findings in this work confirm the observation that equilibration of olefin isomers does not occur for C_4-C_6 olefin conversion on H-ZSM-5 at 783–813 K. We quantify the extent of alkene isomerization and account for the adsorption constants and cracking modes of each olefin isomer in studying olefin cracking to elucidate β-scission kinetics at differential reaction conditions (Section 2.2.4).

Group additivity methods, originally proposed by Benson,[82] have been used for rapid estimation of thermodynamic data of gaseous molecules from a limited set of parameters, called group additivity values (GAVs), in which a group is defined as a central atom with ligands. Group correction methods were developed to encompass structural features of the molecules that are difficult to incorporate into a group additivity scheme, such as non-bonded interactions, non-next-nearest neighbor interactions, ring strain effects, and symmetry corrections.[82] This semi-empirical method has been implemented extensively for gas-phase organic compounds and radicals;[83–85] the application in estimation of thermochemical properties of surface species was first developed by Kua et al.[86] for examining hydrocarbon adsorption on metal surfaces and was further extended by Salciccioli et al.[87,88] for studying the conversion of oxygenates (carboxylic acids, ethers, esters etc.) on group VIII transition metals. Linear scaling relationships for relating the binding energy of a species on one transition metal surface to that of another were developed by Nørskov and coworkers[89,90] to semi-empirically estimate reaction energies. Thermochemical data for surface species on zeolites, however, are scarce and are derived mostly from DFT calculations,[91–95] which precludes detailed kinetic studies of large hydrocarbon reaction systems on zeolites. Our study proposes linear group correction relationships based on thermochemical properties of gas-phase alkanes to calculate enthalpy and entropy of formation of surface alkoxide species on H-ZSM-5. Thereby,

olefin adsorption enthalpy and entropy values can be obtained to rigorously assess the contributions of adsorption and kinetics to observed β-scission rates for C_4-C_6 olefin cracking.

In this work, intrinsic rate constants and activation energies of β-scission modes C, D, E, and F were analytically inferred from butene, pentene, and hexene cracking at 773–813 K on H-ZSM-5, accounting for the concentration of each alkene isomer in the effluent stream. Linear relationships for estimating enthalpy and entropy of formation for surface alkoxides were proposed to assess adsorption constants for each olefin isomer based on group additivity methods implemented in Rule Input Network Generator (RING).[96,97] Dominant olefin cracking pathways and kinetic parameters for the different modes of β-scission were assessed and are compared with recent computational chemistry reports to infer that (i) intrinsic β-scission rate constants and activation energies follow the rules of carbenium chemistry: $E_{inE} < E_{inC} < E_{inD} < E_{inF}$ and k_E: k_C: k_D: k_F = 1094: 21: 8: 1 at 783 K, and (ii) tertiary alkoxides have the lowest adsorption constants amongst other surface adsorbates, restricting thereby the contribution from mode E cracking.

2.2. Materials and methods

2.2.1. Thermochemistry for surface alkoxides on H-ZSM-5

The enthalpy and entropy of formation for alkoxides on H-ZSM-5 were calculated using RING, developed by Rangarajan et al.,[96–98] which incorporates representation of surface intermediates and accommodates elementary step reaction rules to describe chemical transformations of organic molecules on surfaces. The inputs to RING are (i) the initial reactants, and (ii) a set of reaction rules describing the chemistry. Additional inputs including group additivity rules and group correction rules are used to calculate thermochemical quantities of the molecules and reactions on-the-fly. RING outputs an exhaustive list of species and reactions generated from the reactants and reaction rules provided. The GAVs for gas-phase molecules in RING were taken from Benson et al.,[82] Sabbe et al.,[99,100] and Khan et al.[101] In this study, group correction terms for surface species

on H-ZSM-5 were developed based on the structural similarity between gas phase alkanes and surface alkoxide intermediates, wherein an alkoxide replaces a hydrogen atom in the corresponding alkane with the framework oxygen (Scheme 2.3). Linear relationships between carbon number and enthalpy/ entropy differences between alkoxides and alkanes were assessed as follows (Scheme 2.3):

The enthalpy of formation for a surface alkoxide species was calculated as:

$$dH_{alkoxide} = dE_{chem} + 12 + dH_{olefin}, \quad (2.1)$$

where $dH_{alkoxide}$ and dH_{olefin} are the enthalpy of formation of the alkoxide and the olefin, respectively; dE_{chem} is the electronic energy of olefin chemisorption on H-ZSM-5; 12 (kJ mol^{-1}) is the correction term relating the chemisorption electronic energy to the chemisorption enthalpy resulting from the contribution of zero point vibrational energy and thermal corrections.[92] Values of dH_{olefin} (kJ mol^{-1}) were taken from RING at 298 K and dE_{chem} from Nguyen et al.[92] for secondary and internal secondary alkoxides at 298 K. For tertiary alkoxides, $dH_{alkoxide}$ values were directly calculated from $dH_{alkoxide} = -21.7 \times CN - 40.9$ as reported by Nguyen et al.[91]

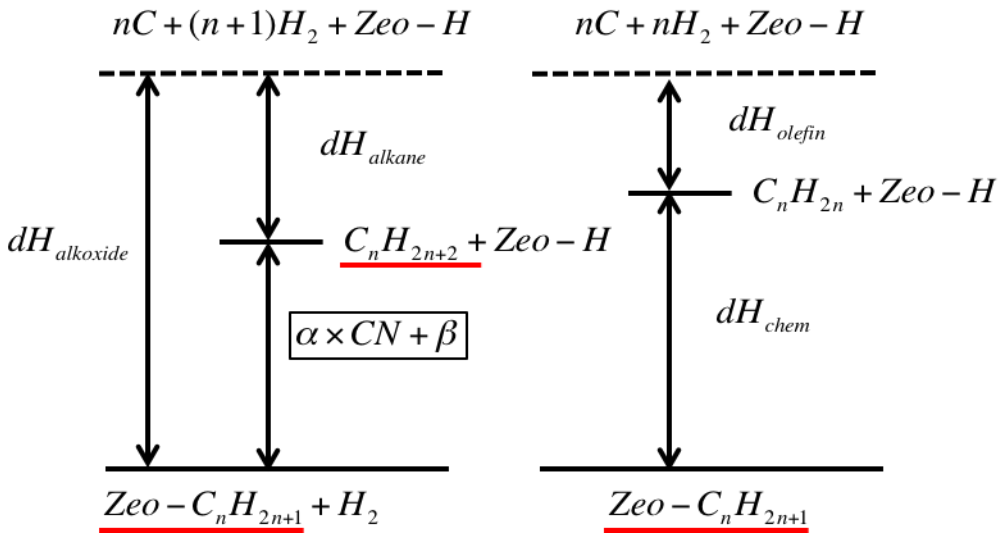

Scheme 2.3 A representation of enthalpies involved in developing linear relationships for alkoxides, which is based on the structural similarity between gas phase alkanes (underlined) and surface alkoxide intermediates (underlined), i.e., an alkoxide replaces a hydrogen atom in the corresponding alkane with the framework oxygen.

The enthalpy difference between an alkoxide and an alkane was found to be linearly dependent on carbon number for secondary, internal secondary, and tertiary alkoxides (Equation 2.2). A linear relationship for primary alkoxides was determined using the same slope as that used for secondary alkoxides with the intercept determined by referencing values for ethane computed using RING to that computed for ethoxide formation by Nguyen et al.[92] using density functional theory.

$$dH_{alkoxide} - dH_{alkane} = \alpha \times CN + \beta, \quad (2.2)$$

where $dH_{alkoxide}$ is as defined in Equation 2.1 and dH_{alkane} at 298 K was calculated using RING.

A linear relationship for entropy of formation of alkoxides was found in a similar manner and is reported in Equation 2.3 below:

$$dS_{alkoxide} - dS_{alkane} = \gamma \times CN + \eta, \quad (2.3)$$

where $dS_{alkoxide}$ values (J mol^{-1} K^{-1}) were taken from those reported by Nguyen et al.[92] at 298 K for secondary and internal secondary alkoxides and dS_{alkane} values at 298 K were calculated using RING.

The assumptions in this analysis are (i) linear relationships found for linear olefins are applicable for branched olefins, and (ii) the thermochemical values reported at 298 K are valid at higher temperatures.

2.2.2. Catalyst preparation

A ZSM-5 sample from Zeolyst International (CBV 8014) was sieved in the ammonium form to obtain aggregate particle sizes between 180 and 425 μm (40-80 mesh). The Si/Al ratio for the ZSM-5 sample was determined by elemental analysis using inductively coupled plasma optical emission spectrometry (ICP-OES) to be 42.6 (performed by Galbraith Laboratories in Knoxville, TN). Results from elemental analysis, N_2 adsorption experiments, and X-ray diffraction are reported in Table 2.6 and Figure 2.4 in Section 2.5. The samples were treated in flowing dry air (1.67 cm^3 s^{-1}, ultrapure, Minneapolis Oxygen; 0.0167 K s^{-1} ramp rate) at 773 K for 4 hours to thermally decompose NH_4^+ to H^+ and $NH_{3(g)}$ and form protonated zeolites, denoted as H-ZSM-5. Chiang et al.[102] performed dimethyl ether (DME) titration experiments at 438 K over the ZSM-5 sample used in this study and showed that 0.5 ± 0.05 DME molecules are adsorbed per acid site indicating that the Brønsted acid site concentration is nearly identical to the Al content determined from ICP-OES.

2.2.3. Steady-state catalytic reactions of olefin cracking

Steady-state olefin cracking reactions were carried out in a 10 mm inner diameter packed-bed quartz reactor at 180 kPa (Table 2.1). The catalyst was supported on a quartz frit at the bottom of the reactor, and the temperature was controlled using a furnace (National Electric Furnace FA120 type) connected to a Watlow Temperature Controller (96 series). The reactor temperature was measured using a K-type thermocouple placed in a thermal well in the middle of the reactor bed. Samples (the milligram catalyst sample was

obtained from a previously diluted catalyst mixture, which was further diluted in quartz sand to 0.8 g total weight in the reactor) were pretreated in flowing He (2.17 cm^3 s^{-1}, ultrapure, Minneapolis Oxygen) at 773 K (0.033 K s^{-1} temperature ramp) for 6 hours. A mixture of methane and argon (1:99, Matheson) was used as an internal standard and was combined with the olefinic reactant: 1-butene (Matheson Tri-Gas, chemical purity grade); 2-pentene or 2-methyl-2-butene (Sigma-Aldrich, analytical grade); 1-hexene, *trans*-4-methyl-2-pentene or 2,3-dimethyl-2-butene (Sigma-Aldrich, analytical grade). Pentene and hexene isomers were introduced using a syringe pump (kdScientific) with He as carrier gas to maintain the desired total flow rate (2.3 – 3.3 cm^3 s^{-1}). The reactor effluent composition was monitored using a gas chromatograph-mass spectrometer (GC-MS, Agilent 7890-5975C) through a methyl-siloxane capillary column (HP-1, 50.0 m x 320 μm x 0.52 μm) connected to a flame ionization detector and a (5% Phenyl)-methylpolysiloxane capillary column (HP-5, 50.0 m x 320 μm x 0.52 μm) connected to a mass spectrometer.

Table 2.1 Reaction conditions for olefin cracking over H-ZSM-5.

Olefin	Conversion	Temperature range	Catalyst amount (mg)	Olefin pressure (Pa)	Modes of cracking
1-butene	<0.1%	783 K–803 K	0.6	17	F
2-pentene	<1%	773 K–803 K	0.3	13	D, F
2-methyl-2-butene	<1%	773 K–803 K	0.3	13	D, F
1-hexene	<10%	773 K–803 K	0.3	38	C, D, E, F
trans-4-methyl-2-butene	<15%	773 K–813 K	0.3	34	C, D, E, F
2,3-dimethyl-2-butene	<3%	773 K–813 K	0.3	48	C, D, E, F

2.2.4. Method for obtaining intrinsic β-scission rate constants

Butene, pentene, and hexene cracking involve β-scission modes C, D, E, and F (Table 2.1), and form four sets of cracking products, which can be formulated into four independent equations (Equation 2.7-2.10) having four β-scission rate constants that are assumed to be independent of the olefin carbon chain length based on the consideration that in each β-scission mode a similar C-C bond is fragmented in a molecule with a similar carbon backbone structure. Sub-modes with the same carbenium ions involved, for instance, 1^o to 3^o (E_1) and 3^o to 1^o (E_2), are lumped as a single mode to reduce the number of unknowns for the four equations. Simultaneously solving four equations from the four sets of cracking products enables an analytical solution for calculating the rate constants of β-scission modes C, D, E, and F without parameter estimation. The equations involved are shown below with 2-pentene feed as an example.

The propene synthesis rate for 2-pentene cracking can be expressed as:

$$r_{C_3^=} = \sum_j k_i K_j (1-\theta) P_j, \tag{2.4}$$

where $r_{C_3^=}$ is in (mol (mol H^+)$^{-1}$ sec^{-1}); P_j is the partial pressure of pentene isomer j, resulting from 2-pentene isomerization, in (Pa) measured in the effluent stream; k_i is the rate constant of mode i (mode D or F) that corresponds to pentene isomer j in (s^{-1}); K_j is the adsorption equilibrium constant of isomer j (Pa^{-1}) evaluated at reaction temperature extrapolating adsorption enthalpies and entropies obtained at 298 K; θ is the fractional surface coverage of all pentene isomers, with the consideration that olefin chemisorption is fast and quasi-equilibrated.[72]

The mass balance of a catalyst bed in a continuous-flow reactor at differential conversion conditions (<15% conversion) is:

$$F_{C_3^= out} - F_{C_3^= in} = (r_{C_3^=})\, w_T, \tag{2.5}$$

where w_T is the total number of acid sites.

$F_{C_3^= in}$ is zero, $F_{C_3^= out}$ can be measured in the effluent stream, and $r_{C_3^=}$ is expressed as Equation 2.4 and subsequently Equation 2.5 becomes:

$$F_{C_3^= out} = \left[\sum_j k_i K_j (1-\theta) P_j\right] w_T \quad (2.6)$$

The enthalpy and entropy of each olefin isomer were calculated using RING by group additivity with group correction methods as described above (Section 2.2.1) to calculate the equilibrium constant, K_j. The fractional surface coverage, θ, was determined by considering the highest concentrations of the adsorbed species in the system: olefin feed pressure at the inlet and partial pressure of the cracking products at the outlet. θ was $<10^{-6}$ for butene, pentene, and hexene cracking, demonstrating that the catalyst surface is predominantly uncovered under the reaction conditions employed in this research.

2.2.5. Assessment of reactor bed dilution

Dilution of the catalyst bed would cause deviation of the conversion from an undiluted bed, which is a result of local bypass effects when catalyst particles are discretized in a local area by the surrounding inert. Berger et al.[103] investigated the relation between the extent of bed dilution and the deviation of the observed chemical conversion using a random particle distribution model and a first order irreversible reaction: N_2O decomposition on Co-La-Al mixed oxide. They found that the deviation would increase with the diluent fraction but decrease with conversion. Berger et al.[103] showed that bypass effects can be neglected when the dimensionless residence time (<0.25) and fractional conversion (<15%) in the bed are low. The deviation of fractional conversion was taken to be negligible in this study due to the observed conversions (<15%) and residence times (<0.03) remaining within the limits of differential conversion as outlined by Berger et al.[103]

2.3. Results and discussion

Linear relationships used for calculating enthalpy and entropy of surface alkoxides are shown in Table 2.2 and they are archived in the input group correction file to RING. Symmetry correction values, which are corrections to the rotational entropy that arise from

indistinguishable atoms in a molecule, were separately incorporated for calculating $dS_{alkoxide}$. Adsorption enthalpies and entropies obtained from RING showed good agreement with those reported by Nguyen et al.[92] using DFT calculations (Figure 2.1).

Table 2.2 Linear dependences of carbon number with enthalpy (Equation 2.2) and entropy (Equation 2.3) difference between alkoxide and alkane formation.

Enthalpy Difference			Entropy difference		
Alkoxide	α	β	Alkoxide	γ	η
1°	-4.4	26.80	All	-9.39	-157.43
2°	-4.4	9.13			
Internal 2°	-8.92	25.68			
3°	-1.78	25.86			

The kinetics of olefin cracking on H-ZSM-5 were quantitatively assessed for β-scission modes C, D, E, and F (Scheme 2.1b) by simultaneously solving four equations from butene, pentene (2-pentene and 2-methyl-2-butene feeds), and hexene (1-hexene, *trans*-4-methyl-2-pentene, and 2,3-dimethyl-2-butene) cracking (Table 2.1), assuming β-scission rate constants to be independent of carbon chain length, and β-scission modes to be lumped as a single mode, e.g., sub-modes E1 and E2 were lumped as mode E. These experiments were operated at differential conversion in the presence of olefin isomerization, however, with minimal olefin oligomerization and hydride transfer reactions as stoichiometric ratios of primary cracking products were observed in the effluent, and only trace amounts of higher olefins were observed, if any at all.

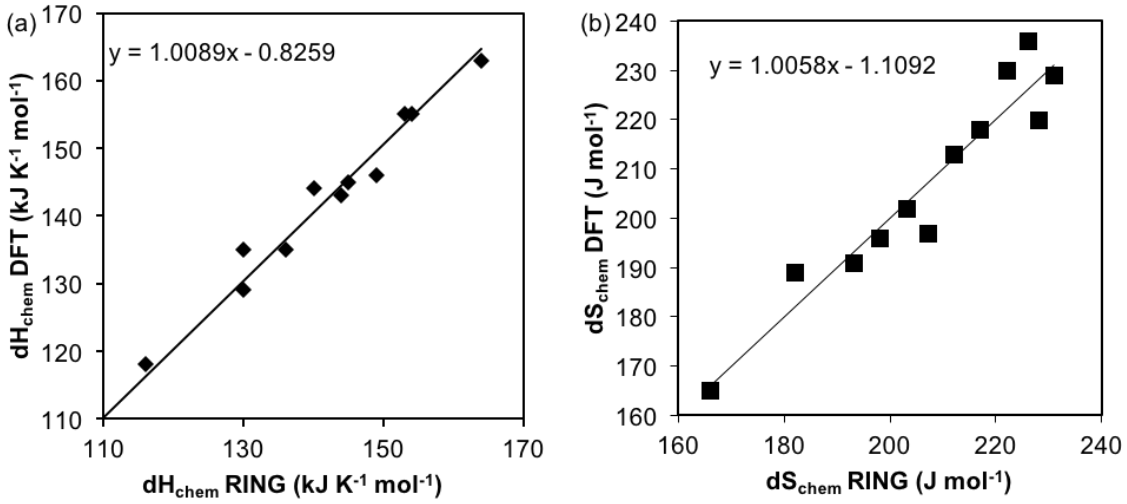

Figure 2.1 Parity plots of (a) chemisorption enthalpies and (b) entropies reported by Nguyen et al.[91,92] vs. those calculated using RING.

2.3.1. Butene cracking – kinetics of mode F

The rate constants for β-scission mode F were inferred from 1-butene cracking reactions on H-ZSM-5 (Table 2.3). Isomerization of 1-butene feed was observed; amongst the isomers of butene, only 1-butene undergoes β-scission reactions via cracking mode F to form 2 molecules of ethene. Higher olefins were absent in the effluent stream, indicating that ethene was formed from elementary step β-scission reactions and not from secondary oligomerization and cracking reactions. Intrinsic activation barriers of cracking mode F were obtained from intrinsic rate constant values at various temperatures calculated using Equation 2.7; an Arrhenius plot is shown in Figure 2.2a. The fractional surface coverage was low ($<10^{-6}$) and the partial pressure of 1-butene was determined from the effluent stream.

$$F_{oC_2^=} = k_F \, K_{1-C_4^=} \, P_{1-C_4^=} \, w_T \qquad (2.7)$$

The intrinsic activation energy of β-scission mode F (E_{inF}) on H-ZSM-5 obtained in this study (257 ± 19 kJ mol^{-1}) showed good agreement with previously reported results from theoretical calculations: 238 kJ mol^{-1} reported by Lesthaeghe et al.[76] using ONIOM(B3LYP/6-31g(d):MNDO) methods and 236 kJ mol^{-1} reported by Vandichel et

al.[104] using ONIOM(B3LYP/6-31+g(d):HF/6-31+g(d)) methods. The adsorption enthalpy of 1-butene (116 kJ mol^{-1})[92] has been added to both values that are reported as apparent activation energies.

Table 2.3 A comparison of kinetic parameters of β-scission modes C, D, E and F.

Cracking Mode	k_{in} (s^{-1})	E_{in} (kJ mol^{-1})	
	Experiment (783 K)	Experiment	Computational Studies
F (1^o to 1^o)	1.9×10^2	257 ± 19	238[76] 236[104]
D (1^o to 2^o and 2^o to 1^o)	1.5×10^3	193 ± 13	D_1: 196[70] D_2: 233[70] D_2: 183[105]
C (2^o to 2^o)	3.1×10^4	185 ± 4	161[70]
E (1^o to 3^o and 3^o to 1^o)	1.6×10^6	160 ± 7	E_1: 144[70] E_2: 200[70]

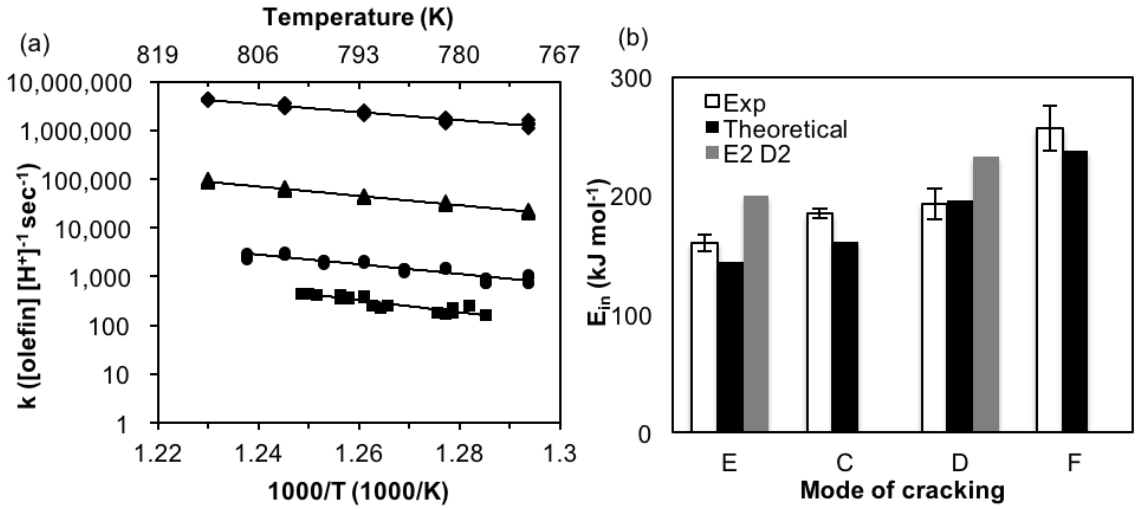

Figure 2.2 Intrinsic rate constant and activation energy of β-scission modes C, D, E and F from butene, pentene, and hexene cracking on H-ZSM-5 at 773–813 K. (a) Arrhenius plots of intrinsic rate constants: (◆) kE, (▲) kC, (●) kD, and (■) kF. (b) Comparison of intrinsic activation energies with DFT calculations. (□) Current finding, (■) Computational values for E_1 and D_1, (■) Computational values for E_2 and D_2.[70,76]

2.3.2. Pentene cracking – kinetics of mode D

An analogous set of experiments to those conducted for butene cracking was performed for pentene cracking over H-ZSM-5 (Table 2.1) to infer the rate constants of mode D cracking. The effluent streams when feeding 2-pentene and 2-methyl-2-butene over the zeolite (<1% conversion, at 773–803 K) contained a 1:1 ratio of ethylene and propene, and a non-equilibrium distribution of pentene isomers. Minimal C_{5+} hydrocarbons were detected in the effluent stream indicating that the ethylene and propene observed in the effluent are formed in elementary step β-scission reactions of C_5 isomers. The various pentene isomers can crack through either mode F or mode D and some isomers of pentene cannot undergo cracking: for example, 1-pentene can crack through mode F or D, depending on where the double bond is protonated (Scheme 2.1c). The identity and concentration of pentene isomers in the effluent stream was quantified by GC-MS to account for the individual contribution of each pentene isomer in synthesizing ethene and

propene. Cracking rate constants of mode D (k_D) were then determined from Equation 2.8 with k_F values taken from 1-butene cracking assuming that intrinsic β-scission rate constants do not vary significantly with an increase of the olefin chain length.

$$F_{oC_3^=} = (k_D\, K_{\frac{C}{T}-2-C_5^=}\, P_{\frac{C}{T}-2-C_5^=} + k_D\, K_{3-C_1-1-C_4^=}\, P_{3-C_1-1-C_4^=} + k_D\, K_{1-C_5^=}\, P_{1-C_5^=} + k_F\, K_{1-C_5^=}\, P_{1-C_5^=} + k_F\, K_{2-C_1-1-C_4^=}\, P_{2-C_1-1-C_4^=})w_T \quad (2.8)$$

Intrinsic activation energies of mode D (E_{inD}) on H-ZSM-5 (193 ± 13 kJ mol^{-1}) derived from an Arrhenius plot using k_D values assessed using both 2-pentene and 2-methyl-2-butene as feeds (Figure 2.2b) are comparable to the 196 kJ mol^{-1} and 233 kJ mol^{-1} values for modes D_1 and D_2 reported by Mazar et al.[70] using PBE-D DFT calculations and the 183 kJ mol^{-1} value for 1-hexene cracking via the D_2 mode reported by Guo et al.[105] using ONIOM(B3LYP/6-31G(d,p):UFF) and an 88T MFI cluster.

2.3.3. Hexene cracking – kinetics of mode C and E

A set of experiments to those conducted for butene and pentene cracking was performed for 1-hexene, *trans*-4-methyl-2-pentene, and 2,3-dimethyl-2-butene cracking over H-ZSM-5 (Table 2.1) to infer rate constants of cracking modes C and E. We observed a 1:1 molar ratio of ethene and butene and a non-equilibrium distribution of hexene isomers in the effluent stream. The concentrations of hexene isomers in the effluent depend strongly on the hexene feed (Figure 2.5 in Section 2.5): a more branched olefin isomer feed was less likely to isomerize into an olefin isomer with a different structural backbone, because of the size restrictions imposed by the microporous voids of the zeolite and thereby result in a non-equilibrium olefin isomer distribution. Product selectivity of the various hexene feeds at 783 K however, were consistent with each other (Table 2.4) and comparable to that reported by Buchanan et al.[72] for 1-hexene cracking on H-ZSM-5 at 783 K (ethene: propene: butene = 7: 83.6: 7.9 at 20.1% conversion). A total of 10 out of 17 possible hexene isomer peaks were identified in the effluent to close the carbon balance ± 5%.

Rate constants of cracking type C and E were obtained by taking the hexene partial pressures measured in the effluent stream and k_D and k_F values from pentene and butene cracking results to simultaneously solve Equation 2.9 and 2.10.

$$0.5F_{oC_3^=} = (k_C\, K_{T-4-C_1-2-C_5^=}\, P_{T-4-C_1-2-C_5^=} + k_C\, K_{4-C_1-1-C_5^=}\, P_{4-C_1-1-C_5^=} + k_D\, K_{2,3-diC_1-1-C_4^=}\, P_{2,3-diC_1-1-C_4^=} + k_F\, K_{2-C_1-1-C_5^=}\, P_{2-C_1-1-C_5^=})w_T \quad (2.9)$$

$$F_{oC_2^=} = (k_E\, K_{3,3-diC_1-1-C_4^=}\, P_{3,3-diC_1-1-C_4^=} + k_E\, K_{2-C_1-1-C_5^=}\, P_{2-C_1-1-C_5^=} + k_E\, K_{2-C_1-2-C_5^=}\, P_{2-C_1-2-C_5^=} + k_D\, K_{T-3-C_1-2-C_5^=}\, P_{T-3-C_1-2-C_5^=} + k_F\, K_{4-C_1-1-C_5^=}\, P_{4-C_1-1-C_5^=} + k_F\, K_{2-C_2-1-C_4^=}\, P_{2-C_2-1-C_4^=})w_T \quad (2.10)$$

Activation energies of mode C (E_{inC}) (185 ± 4 kJ mol^{-1}) and E (E_{inE}) (160 ± 7 kJ mol^{-1}) were obtained from temperature dependence plots of the rate constants using cracking data from the three hexene isomer feeds (Figure 2.2a). These numbers compare favorably with those calculated using PBE-D DFT calculations by Mazar et al.[70] who report values of 144 kJ mol^{-1} and 200 kJ mol^{-1} for modes E_1 and E_2, and 161 kJ mol^{-1} for mode C (Figure 2.2b). Rate constants, k_E and k_C, obtained using three different hexene isomers as feeds plotted in Figure 2.2a are consistent and this consistency in rate constants shows that even though the degree of isomerization varies when using different isomers as the primary feed, accounting for the adsorption and kinetics of each isomer in the effluent stream enables the rigorous evaluation of intrinsic β-scission rate constants.

Table 2.4 Selectivity to ethene: propene: butenes from hexene cracking at 783 K.

Hexene isomer feeds	Conversion	$C_{2=}$: $C_{3=}$: $C_{4=}$
1-hexene	10%	9.6 : 80.9 : 9.5
trans-4-methyl-2-butene	15%	9.0 : 82.0 : 9.0
2,3-dimethyl-2-butene	3%	9.6 : 80.8 : 9.6

Comparing activation energies of the submodes E_{inE1}, E_{inE2} and E_{inD1}, E_{inD2} from Mazar et al.[70] (Figure 2.2b) shows that experimental values reported here agree better with E_{inE1} and E_{inD1} modes where the primary alkoxide is involved in the reactant state and the more substituted β C (tertiary and secondary) is involved in the transition state,[70] implying that modes E_{inE1} and E_{inD1} are more dominant in the lumped groups E and D, respectively, due to lower activation barriers relative to E_{inE2} and E_{inD2}.

2.3.4. Chemisorption and apparent rate constants for cracking of hexene isomers

An examination of the chemisorption equilibrium constants of all adsorption modes of the 8 hexene isomers, among the 10 identified, that are viable for β-scission (Figure 2.3a) showed that, in general, the adsorption of secondary alkoxides is favored over primary and tertiary alkoxides, which are the least favorable ones. The ratio of the largest adsorption constants amongst internal secondary, secondary, primary, and tertiary alkoxides is 555: 314: 17: 1 from *trans*-4-methyl-2-pentene, 4-methyl-1-pentene, 4-methyl-1-pentene, and 2,3-dimethyl-1-butene, respectively, at 783 K. A closer examination of only the adsorption modes available to crack among the 8 hexene isomers against the four modes of cracking reveals that olefins that undergo cracking via mode E have the fastest intrinsic rate constant but the lowest adsorption constant (Figure 2.3b).

A comparison of the apparent rate constants of hexene cracking, $k_i K_j$ (s^{-1} Pa^{-1}) (i: mode E, C, D, or F; j: the corresponding hexene isomer) (Figure 2.3c) shows that (i) olefins that crack through mode C have larger apparent rate constants than mode E; (ii) the contributions from cracking modes D and F can be neglected under the reaction conditions considered (773–813 K). A comparison of cracking mode C which forms two propene molecules and mode E which forms ethene and butene from hexene cracking reveals that the largest apparent rate constants involve $k_C K_{3\text{-methyl-1-pentene}}$ and $k_E K_{2\text{-methyl-2-pentene}}$ in a 9: 1 ratio at 783 K, which is consistent with experimental observations wherein the measured ratio of propene to ethene synthesis is 8 : 1 at 783 K. This implies that the observed product distribution of olefin cracking involves the interplay between olefin chemisorption constants and the intrinsic β-scission rate constant. Hence, the assumption that the most

favorable mode of cracking, mode E, predominates over other modes is shown to be invalid in the case of H-ZSM-5 due to their unfavorable adsorption properties.

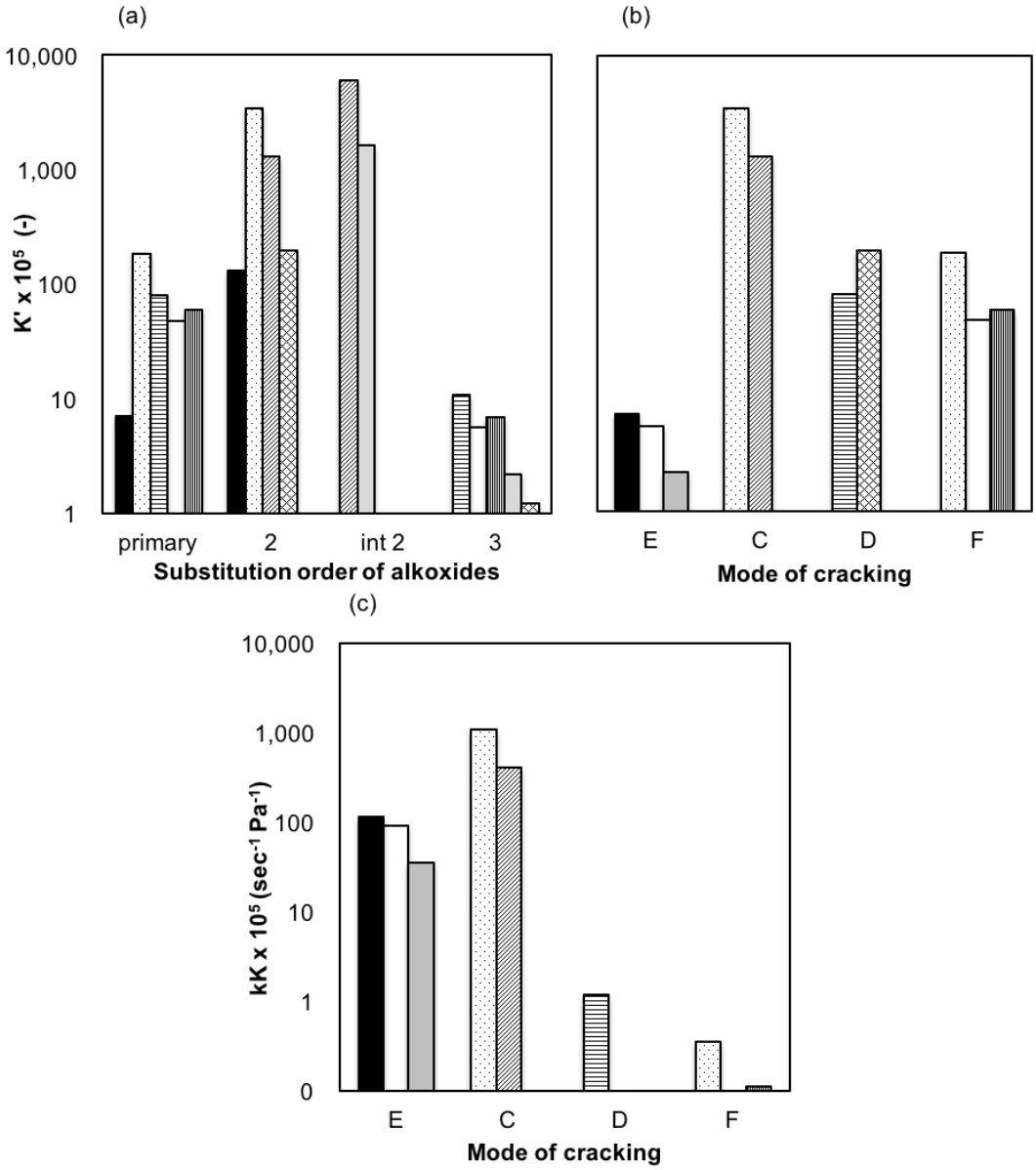

Figure 2.3 (a) Adsorption constants of all adsorption types from the 8 olefins identified; (b) Adsorption constants of the adsorption types that can crack from the 8 olefins; (c) Apparent rate constants of the 8 olefins. (K (Pa^{-1}) = K' (-) $\times 10^{-5}$ (Pa^{-1})) (black) 3,3-diC_1-1-C_4, (white)2-C_1-1-C_5, (gray)2-C_1-2-C_5, (dotted)4-C_1-1-C_5, (horizontal lines) 2,3-diC_1-1-C_4, (vertical lines) 2-C_2-1-C_4, (diagonal lines) *trans*-4-C_1-2-C_5, (crosshatched) *trans*-3-C_1-2-C_5. All adsorption constants reported herein are evaluated at 783 K.

The conversion of 2,3-dimethyl-2-butene (<3%, 48 Pa), which does not have any available modes of cracking, was much lower than 1-hexene (<10%, 38 Pa) and *trans*-4-methyl-2-pentene (<15%, 34 Pa) feeds and the unreacted feed accounted for ~50% of all the hexene isomers in the effluent. A further comparison of the fractional contributions to propene and ethene syntheses from the 4 modes of β scission in hexene cracking (Table 2.5) reveals that when using 2,3-dimethyl-2-butene as primary feed, the fractional contributions are significantly different from those using 1-hexene and *trans*-4-methyl-2-pentene. These differences coincide with the isomer distributions of each of the feeds (Figure 2.5 in Section 2.5) measured in the effluent in hexene cracking – 2,3-dimethyl-2-butene feed has extreme isomer distributions (~50% of 2,3-dimethyl-2-butene, and ~23% of 2,3-dimethyl-1-butene) compared to those observed when using 1-hexene and *trans*-4-methyl-2-pentene (both feeds have ~6% of 2,3-dimethyl-2-butene and ~3% of 2,3-dimethyl-1-butene in the effluent stream) as primary feeds which demonstrates that (i) different carbon backbones of hexene feeds may result in different extent of olefin isomerization; (ii) besides apparent rate constants of olefin cracking, the concentrations of the dominant precursors can also significantly influence cracking rates.

Table 2.5 Averaged fractional contributions from different modes of cracking to hexene cracking products between 783–813 K (%).

Cracking products	2 C_3			C_2 and C_4		
Cracking modes	C	D	F	E	D	F
2,3-dimethyl-2-butene	98.74	1.25	0.01	97.52	2.38	0.10
trans-4-methyl-2-butene	99.92	0.06	0.02	96.54	3.33	0.13
1-hexene	99.92	0.06	0.02	96.60	3.27	0.13

2.4. Conclusions

Linear relationships between alkoxide and alkane enthalpy and entropy of formation were proposed to estimate olefin adsorption constants on H-ZSM-5 based on group additivity and group correction methods, which, in general, can be applied to surface chemistries on zeolitic solid acids with specific numbers reported here applicable to H-ZSM-5. Intrinsic β-scission rate constants of mode C, D, E, and F were inferred from cracking of linear and branched isomers of butene, pentene, and hexene at low conversion (<15%) over a temperature range of 773–813 K by simultaneously solving for the observed concentration of cracking products analytically and concurrently accounting for the non-equilibrium distribution of olefin isomers in the effluent stream with the assumption that intrinsic rate constants are independent of carbon chain length. Intrinsic activation energies calculated from Arrhenius plots showed good agreement with computational calculations. The intrinsic rate parameters of β-scission modes were dominated by the substitution order of the reactant and product alkoxides, wherein $E_{inE} < E_{inC} < E_{inD} < E_{inF}$ and k_E: k_C: k_D: k_F = 1094: 21: 8: 1 at 783 K. Secondary alkoxides were found to have higher adsorption constants than primary and tertiary, which is the least favorable adsorption mode; olefins having cracking mode E were also found to have the smallest adsorption constants and mode C the largest. The apparent rate constants, $k_i K_j$ (s^{-1} Pa^{-1}), of mode C were found to be ~9 times larger than that of mode E, however, the intrinsic rate constant of mode E is ~52 times larger than mode C (k_E : k_C = 52 : 1 at 783 K). The varying extents of olefin isomerization observed in olefin cracking using different hexene feeds affects the fractional contribution of the four modes of β-scission to the cracking products, which demonstrates that the concentration of dominant olefin cracking precursors is also an important factor in determining olefin cracking rates.

2.5. Supporting information

2.5.1. Structural characterization of ZSM-5

2.5.1.1. Nitrogen adsorption experiments

Nitrogen adsorption/desorption measurements were carried out at 77 K on an Autosorb-1 analyzer (Quantachrome Instruments). Samples were evacuated overnight at 573 K and 1 mm Hg prior to measurement. The specific surface area was obtained using the Brunauer–Emmett–Teller (BET) method from the adsorption data at P/P_0 between 0.1 and 0.3. Conventional t-plot methods were used to extract micropore volume from the nitrogen adsorption data over t ranges from 3 to 5 Å. Derived values from Liu et al.[106] are reproduced in Table 2.6.

Table 2.6 Characterization information for ZSM-5 used in this study. a) ICP-OES elemental analysis as performed by Galbraith Laboratories. b) Adsorbed DME per Al atom on zeolites at 438 K.[102] c) BET parameters fit to nitrogen adsorption data as taken from a Quantachrome Autosorb. d) Micropore volume determined by t-plot method.

Zeolyst zeolite Sample (Si/Al)	Si/Al (ICP-OES)[a]	DME/Al[b]	BET surface area (m^2 g^{-1})[c]	BET micropore volume (cc g^{-1})[c, d]
H-ZSM-5 (40)	42.6	0.49	406	0.13

2.5.1.2. X-ray diffraction patterns

Powder X-ray diffraction (XRD) patterns were collected on a Bruker AXS D5005 diffractometer using Cu-Kα radiation with a step size of 0.04° and a step time of 3 s.

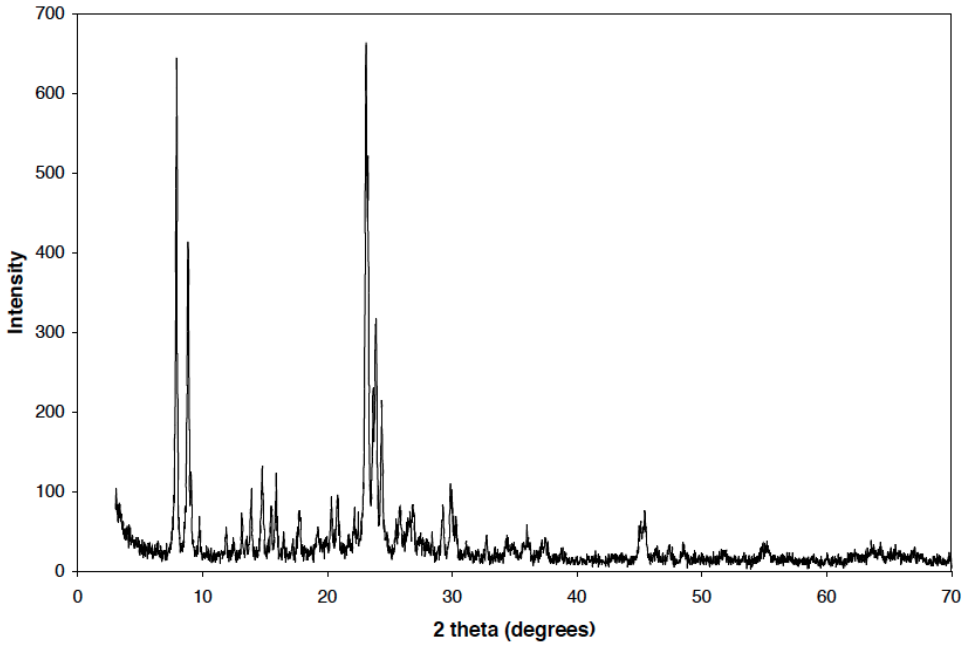

Figure 2.4 XRD pattern for H-ZSM-5 (Si/Al=40).

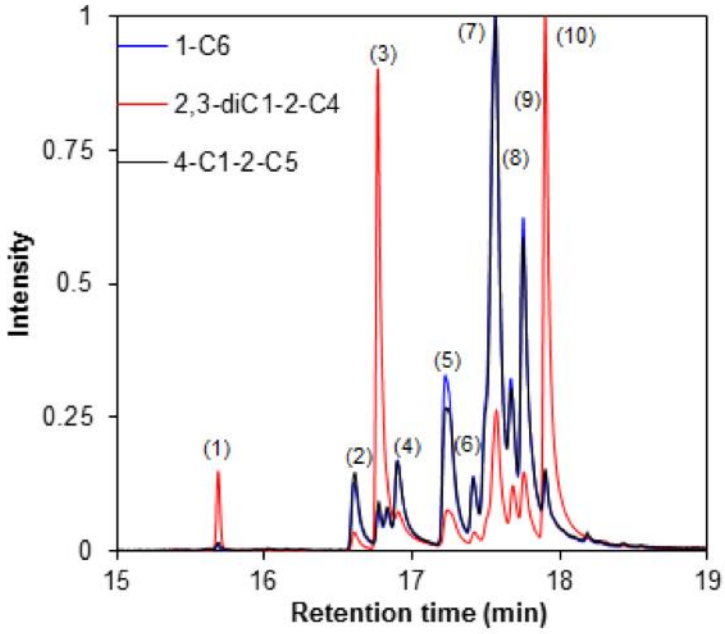

Figure 2.5 Hexene isomer distributions for (-)1-hexene, (-) 2,3-dimethyl-2-butene, and (-) *trans*-4-methyl-2-pentene feeds at 783 K. (1) 3,3-dimethyl-1-butene, (2) 4-methyl-1-pentene, (3) 2,3-dimethyl-1-butene, (4) *trans*-4-methyl-2-pentene, (5) 2-methyl-1-pentene, (6) 2-ethyl-1-butene, (7) 3-hexene, (8) 2-methyl-2-pentene, (9) *trans*-3-methyl-2-pentene, (10) 2,3-dimethyl-2-butene.

2.5.2. Internal and external mass transfer limitation

Internal mass transfer limitations were checked in both zeolite crystallite and pellet region by estimating Thiele Modulus defined as:[107] $\Phi = \frac{-r_{A(obs)} \times \rho_c \times R^2}{D_e \times C_{As}} = \eta\phi^2$, (2.11)

where $-r_{A(obs)}$ is the observed reaction rate in (kmol kgcat^{-1} s^{-1}); ρ_c is the pellet bulk density (1556 kg m^{-3}) or crystallite density (1840 kg m^{-3}); *R* is the catalyst pellet radius (1.50×10^{-4} m) or crystallite radius (1.08×10^{-9} m); *De* is the effective gas phase diffusivity (m^2 s^{-1}); C_{As} is the gas-phase concentration of species A at the catalyst surface in (kmol m^{-3}); η is the internal effectiveness factor and ϕ is the Thiele modulus, where if $\phi \ll 1$, η is close to unity and ϕ can then be calculated. This assumption of η close to unity was checked using Equation 2.12 for first order reaction.[107]

$$\eta = \frac{3}{\phi^2}(\phi\, coth\phi - 1) \quad (2.12)$$

Effective gas phase diffusivity, *De*, is estimated using Equation 2.13:[108]

$$D_e = \varepsilon^2 \frac{1}{\frac{1}{D_{AB}} + \frac{1}{D_{KA}}}, \quad (2.13)$$

where ε is the crystallite (0.007) or pellet (0.383) void fraction.

Knudsen diffisivity, D_{KA}, is defined as:[108]

$D_{KA} = 4850\, d_{pore}\sqrt{\frac{T}{M_A}}$ (2.14), where pore diameter, d_{pore}, is in (cm), molecular weight M_A in (g mol^{-1}), temperature T in (K).

Binary diffusivity, D_{AB}, was taken from Bird et al.:[109]

$$\frac{p\boldsymbol{D_{AB}}}{(p_{cA}p_{cB})^{1/3}(T_{cA}T_{cA})^{5/12}(\frac{1}{M_A}+\frac{1}{M_B})^{1/2}} = a(\frac{T}{\sqrt{T_{cA}T_{cB}}})^b, \quad (2.15)$$

where D_{AB} is in (cm^2 s^{-1}), pressure p is in (atm), temperature T is in (K), $a = 3.640 \times 10^{-4}$ and $b = 1.823$.[109] Molecular weight of A and B is M_A and M_B. Subscript c stands for the corresponding critical properties. A is gas phase olefin and B is helium.

External diffusion limitations, i.e. having concentration gradients between the bulk gas phase and the external surface of the pellet, were checked by Mears criterion:[107]

$$\frac{-r_{A(obs)} \times \rho_b \times R \times n}{k_C \times C_{As}} < 0.15, \qquad (2.16)$$

where ρ_b is bulk density of the catalyst bed in (kg m^{-3}); n is reaction order; k_C is mass transfer coefficient in (m s^{-1}), which can be estimated by the Sherwood number along with the Frossling correlation.[107] The parameters used for the estimation as well as the calculated results for butene, pentene, and hexene cracking at 500 ^{o}C are shown in Table 2.7, indicating that no mass transfer limitations are present.

Table 2.7 Parameters used and estimated for assessing internal and external diffusion limitation.

	1-butene		2-methyl-2-butene		1-hexene	
	Crystallite	Catalyst pellet	Crystallite	Catalyst pellet	Crystallite	Catalyst pellet
Effective diffusivity, D_e, $m^2\ s^{-1}$	7×10^{-12} [(a)]	1.9×10^{-4}	7×10^{-12} [(a)]	1.3×10^{-4}	7×10^{-12} [(a)]	1.6×10^{-4}
Estimated Thiele modulus	2×10^{-5}	0.049	6×10^{-4}	0.123	6×10^{-5}	0.17
Corresponding effectiveness factor	1.000	0.999	1.000	0.998	1.000	0.998
			External Mass transfer			
Mass transfer coefficient, m s^{-1}	8.7		6.0		7.2	
Mear's criterion	0.001		0.002		0.001	

[(a)] Effective diffusivity taken from Haag et al.[110]

2.5.3. The assessment of relaxing the assumption of intrinsic β-scission rate constants being independent of olefin carbon chain length

Hexene cracking pathways from cracking mode D and F have been found to be negligible compared to those from C and E modes (>99% and >96% for mode C and E, respectively) at temperatures between 783-813 K (Table 2.5 in the paper). This implies that carrying forward the kD value from pentene and kF value from butene cracking to calculate kE and kC does not lead to significant errors. The fractional contributions of cracking mode D and F to pentene cracking products shown in Table 2.8, however, indicates that cracking

mode F cannot be neglected. Assuming the activation entropy of F mode increases going from C_4 to C_5 olefin similar to the corresponding alkanes,[111] k_F for pentene is about 3 times higher than that for butene. This implies that contribution of D mode would be a factor of 2.7 times smaller than the original analysis, which corresponds to an error in activation barrier value of ~6 kJ mol^{-1} at 783 K. This error is within the intrinsic errors of DFT calculations and the activation barrier differences between modes D and F (64 kJ mol^{-1}).

The authors decided to maintain the original assumption of intrinsic rate constants being invariant with olefin carbon chain length to maintain the analytical solution presented in the analysis.

Table 2.8 Averaged fractional contributions from different modes of cracking to pentene cracking products between 783–803 K.

Cracking products	C_2 and C_4	
Cracking modes	D	F
2-pentene	0.76	0.24
2-methyl-2-butene	0.79	0.21

2.6. Acknowledgements

We acknowledge financial support from The Dow Chemical Co. and the National Science Foundation (NSF CBET 1055846). We also acknowledge Dr. Mark N. Mazar for helpful technical discussions.

3. Mo_2C catalyzed vapor phase hydrodeoxygenation of lignin-derived phenolic compound mixtures to aromatics under ambient pressure*

3.1. Introduction

Direct upgrade of pyrolysis vapors from depolymerized lignocellulosic biomass can be a sustainable process to produce aromatics[112–114] such as benzene, toluene, and xylenes (BTX), because phenolic monomeric compounds in vapor phase pyrolyzates can recombine and form oligomeric compounds after condensation, resulting in corrosive and viscous bio-oil.[115,116] Catalytic hydrodeoxygenation (HDO) can upgrade pyrolysis vapors by selectively removing oxygen heteroatoms in phenolic compounds as water. Selective cleavage of aryl-oxygen bonds in lignin-derived phenolic compounds, i.e. Ar–OH or Ar–OR, however, is challenging because the bond dissociation energies of aryl-oxygen bonds (422–468 kJ mol^{-1}) are 80–130 kJ mol^{-1} higher than that of aliphatic-oxygen (R–OR) bonds.[36] High H_2 pressure (~1–5 MPa) and/or high temperature (~473–723 K) reaction conditions, therefore, are commonly employed for HDO of phenolic compounds,[38,39] which can promote successive hydrogenation of aromatic rings, resulting in low yield of BTX.

Low yield of BTX (<30%) was obtained from vapor phase HDO of single phenolic model compounds, such as m-cresol or guaiacol, over alumina supported Pt catalysts,[117,118] carbon-supported bimetallic Pt-Sn catalyst,[119] gallium-modified H-BEA zeolite[120] and silica-supported transition metal[112]/ metal phosphide catalysts[121] at temperatures from 523–723 K under atmospheric H_2 pressure as a result of incomplete deoxygenation, significant concurrent hydrogenation, transalkylation, and/or demethylation reactions.

High yield of BTX (~80%) could be achieved from liquid phase anisole HDO over bimetallic FeMo phosphide catalysts at 673 K, however, high hydrogen pressures (2.1 MPa) were required to achieve this yield.[122] Zhao et al.[123] reported >50% BTX selectivity

*Reprinted from Appl. Catal. A Gen., 510 (2016) 42–48. Copyright 2016, with permission from Elsevier.

from vapor phase HDO of guaiacol over transition metal phosphides, specifically, Ni_2P/SiO_2 and Co_2P/SiO_2, at 573 K under atmospheric pressure. High benzene selectivity (99%) for vapor phase phenol HDO over 20.3 wt% Ni/SiO_2 at 573 K and ambient pressure has been demonstrated by Shin et al.[124] Prasomsri et al.[25] also reported high BTX selectivity in vapor phase HDO of anisole (~75%), m-cresol (~99%) over MoO_3, however, low BTX selectivity was found in guaiacol HDO (~45%) at ~1 bar of H_2 pressure and 593–623 K.[25]

Zhao and co-workers[37] showed that liquid phase upgrade of a phenolic monomer mixture containing 4-n-propylphenol, 2-methoxy-4-n-propylphenol, 4-hydroxy-3-methoxyphenylacetone, and 4-allyl-2,6-dimethoxyphenol could be achieved on carbon-supported palladium with H_3PO_4 acting as a dual-functional catalyst at 523 K and 5 MPa H_2. At nearly quantitative conversion, ~80% selectivity to alkanes, and ~8% methanol selectivity were observed.[37] Kinetic studies of single phenolic compounds, such as anisole, catechol, and guaiacol, suggest that multistep reactions including hydrogenation, hydrolysis, and dehydration are involved in HDO of the phenolic mixture.[125] Zhao et al.[125] further demonstrated that n-hexane-extracted bio-oil, which contains C_5–C_6 furans, ketones, aldehydes, and C_6–C_9 phenolic compounds, could be quantitatively converted to the corresponding C_5–C_9 hydrocarbons with ~85% selectivity to C_6–C_9 cycloalkanes with and/or without C_1–C_3 alkyl groups using a Ni/H-ZSM-5 catalyst at 523 K and 5 MPa H_2 in the aqueous phase.

HDO of model pyrolysis vapor, containing guaiacol, H_2, CO, CO_2, and H_2O, over silica supported iron catalysts under atmospheric pressure was investigated by Olcese et al.[126] at 673 K and atmospheric pressure, in which ~40% yield to benzene and toluene was observed, however, severe catalyst deactivation (100% to ~20% in 6 h) concurrently occurred. An integrated process which combines fast-hydropyrolysis of biomass with downstream vapor phase HDO to produce liquid fuels (H_2Bioil) has recently been proposed by Agrawal et al.[114] HDO of fast-hydropyrolysis vapor of poplar (~23 wt% of lignin) over 5 wt% Pt–2.5 wt% Mo supported on multiwalled carbon nanotubes at 25 bar H_2 pressure and 573 K resulted in ~54% total hydrocarbon yield, of which ~20% were C_6–C_8^+ hydrocarbons including cyclic alkanes.[114] Efforts to directly treat pyrolysis vapor from oak

and switch grass pyrolysis using a 5 wt% Ru/TiO_2 catalyst at 673 K and atmospheric pressure (H_2 ~0.58 atm) by Wan et al.[113] resulted in phenol as the dominant product from HDO of the pyrolyzates derived from oak or switch grass, suggesting that deoxygenation was incomplete and hydrogenation of the ring was negligible.[113] These reports demonstrate the challenges of direct HDO of phenolic mixtures to BTX even with the expense of noble metal catalysts.

Molybdenum carbide, nitride, phosphide and oxide supported on titania have been shown to selectively catalyze gas phase HDO of phenol with >85% selectivity to benzene at 723 and 773 K, however, high H_2 pressure (25 bar) was employed.[26] The site time yield for vapor phase phenol HDO products on 15 wt% Mo_2C/TiO_2 catalyst was found to be ~3 times higher than that on 15 wt% MoO_3/TiO_2 and 6.8 wt% Mo_2N/TiO_2,[26] demonstrating that molybdenum carbide catalysts are more active than molybdenum oxides and/or nitride catalysts for HDO of phenolic compounds. Our recent study showed that β-Mo_2C is stable for vapor phase anisole HDO and can preferentially cleave the Ar-O bond, resulting in >90% selectivity to benzene (C_6^+ basis) at ambient pressure and 423 K.[127] Metallic sites were suggested to be involved in vapor phase anisole HDO as benzene rates normalized by the number of exposed metallic sites measured by ex situ CO chemisorption were invariant ($3.4 \pm 1.0 \times 10^{-4}$ mol s^{-1} mol_{CO}^{-1}).[127] In situ CO titration studies for anisole HDO at 423 K ($1.1 \pm 0.3 \times 10^{-3}$ mol s^{-1} mol_{CO}^{-1}) demonstrated that only a fraction of CO chemisorption sites are active for HDO catalysis.[54]

Herein, mixtures of lignin-derived phenolic model compounds containing characteristic bonds, i.e., Ar–OH and $Ar–OCH_3$, such as m-cresol, anisole, 1,2-dimethoxybenzene (DMB), and guaiacol (GUA), were chosen to simulate pyrolysis vapor from lignin depolymerization. The lignin-derived phenolic compounds were selectively converted to the corresponding completely deoxygenated aromatics (BTX) with >90% yield at quantitative conversion, under mild reaction temperatures (533–553 K), and ambient pressure. Kinetic studies suggest that (i) direct hydrodeoxygenation of m-cresol was the dominant pathway for toluene synthesis, and (ii) the methoxyl group in guaiacol was removed prior to the cleavage of the hydroxyl bond. Low alkylbenzene selectivity

(<4%) in HDO of the phenolic mixtures suggests that transalkylation and/or demethylation reactions are insignificant. High H_2 efficiency with <10% selectivity for subsequent hydrogenation products was, presumably, due to in situ modification of the catalyst surface by oxygenate reactants, as inferred from in situ methanol and water chemical titration of benzene/toluene hydrogenation reactions on Mo_2C.

3.2. Materials and methods

3.2.1. Catalyst synthesis and characterization

Mo_2C catalysts were prepared based on a prior report.[127] A tubular quartz reactor (I.D. 10 mm) loaded with 1.2 g of ammonium molybdate tetrahydrate (sieved, 177–400 μm, $(NH_4)_6Mo_7O_{24}\cdot 4H_2O$, Sigma, 99.98%, trace metal basis) was housed in a tube furnace (Applied Test System, Series 3210) equipped with a Watlow Temperature Controller (96 series) where the reaction temperature was monitored by a thermocouple attached to an outer thermowell of the reactor and heated in a gas mixture (total flow rate of ~2.75 $cm^3\ s^{-1}$), comprising 15/85 vol% of CH_4 (Matheson, 99.97%) and H_2 (Minneapolis Oxygen, 99.999%) at ~623 K for 5 h with a ramping rate of ~0.06 K s^{-1} from room temperature (RT). The reactor was subsequently heated from ~623 K to ~863 K (~0.047 K s^{-1}) and held at ~863 K for 3 h. The resulting material was cooled to RT in the CH_4/H_2 gas mixture and subsequently treated in a flow (~1.67 $cm^3\ s^{-1}$) of 1% O_2/He (Matheson, Certified Standard Purity) for ~2 h to passivate the carbidic surface before being removed from the reactor.

The bulk structures of both fresh and spent samples were determined using X-ray diffraction (XRD, Bruker D8 Discover, 2D X-ray diffractometer with a two-dimensional VÅNTEC-500 detector). Cu Kα X-ray radiation with a graphite monochromator and a 0.8 mm point collimator measured in two or three measurement frames at $2\theta = 25^o$, 55^o, and/or 85^o with a 900 s frame/dwell were used to collect two-dimensional images which were then converted to one-dimensional intensity vs. 2θ for analysis.

CO (Matheson, 99.5%) chemisorption for Mo_2C formulations was measured at 323 K using a Micromeritics ASAP 2020 instrument following the protocols reported

previously.[127] Briefly, the catalyst (~0.14 g) was first evacuated at 383 K (~2 μmHg) for 0.5 h, and then treated in H_2 at 723 K for 1 h, followed by degassing (~2 μmHg) at 723 K for 2 h. Two adsorption isotherm measurements (between 100 and 450 mmHg) were taken at 323 K. The cell was degassed (~2 μmHg) to remove weakly adsorbed species before the second isotherm. The amount of irreversibly adsorbed species was obtained by the difference between the two isotherms extrapolated to zero pressure.

The BET surface area was measured using N_2 adsorption/desorption isotherms (Micromeritics ASAP 2020). The sample was degassed (<10 μmHg) at 523 K for at least 4 h before N_2 adsorption.

3.2.2. Vapor phase HDO of phenolic compound mixtures on Mo_2C

Molybdenum carbide catalysts (1.9–18.5 mg) diluted in ~0.3 g quartz sand in a tubular quartz reactor (I.D. 10 mm) were treated in pure H_2 (~1.67 $cm^3\ s^{-1}$) at 723 K (0.125 K s^{-1}) for 1 h and cooled down to the reaction temperature before introducing reactants (~3.67 $cm^3\ s^{-1}$) consisting of 0.03/91/balance (vol%) of oxygenates/H_2 /He, in which the oxygenates represent the sum of the phenolic compound mixtures. Phenolic compound mixtures of anisole (Sigma, ReagentPlus, 99%), m-cresol (Sigma, ≥98%), guaiacol (GUA, SAFC, natural, ≥98%), and 1,2-dimethoxybenzene (DMB, Sigma, ReagentPlus, 99%) were added using a syringe pump (KD Scientific, Model 100) and the reactor effluents were analyzed by an online gas chromatograph (GC, Agilent 7890) equipped with a methyl-siloxane capillary column (HP-1, 50 m × 320μm × 0.52 μm) connected to a flame ionization detector. All lines were heated to at least 398 K via resistive heating to prevent condensation of the compounds in the lines. The equations used to calculate conversion, selectivity, and toluene or benzene ratio are shown below.

$$Total\ conversion\ of\ phenolic\ mixture = \frac{(sum\ of\ C\ in\ phenolic\ reactants)_{in} - (sum\ of\ C\ in\ phenolic\ reactants)_{out}}{(sum\ of\ C\ in\ phenolic\ reactants)_{in}} \times 100\% \qquad (3.1)$$

$$Selectivity\ of\ C_6^+\ product\ i = \frac{moles\ of\ C_{6+}\ product\ i}{moles\ of\ C_{6+}\ products} \times 100\% \quad (3.2)$$

$$Toluene\ or\ benzene\ ratio = \frac{moles\ of\ toluene\ or\ benzene}{moles\ of\ (toluene+benzene)} \times 100\% \quad (3.3)$$

$$Individual\ conversion\ of\ reactant\ i = \frac{(moles\ of\ C\ in\ phenolic\ reactant\ i)_{in} - (moles\ of\ C\ in\ phenolic\ reactant\ i)_{out}}{(moles\ of\ C\ in\ phenolic\ reactant\ i)_{in}} \quad (3.4)$$

Small amounts of catalyst (1.9–18.5 mg) diluted in ~0.3 g of quartz sand were employed to achieve <100% conversion for HDO of phenolic compounds at 553 K. We confirmed that high conversions reported here (82 and 94%) are reproducible as the conversions measured using catalysts that were regenerated in H_2 flow (~1.67 $cm^3\ s^{-1}$ at 723 K for 1 h) were found to be consistent (<±2%) with those of the original runs.

3.2.3. In situ titration for hydrogenation reactions

Vapor phase hydrogenation reactions of a benzene/toluene (molar ratio = 1/1) mixture (1.2/4.9/balance (vol%) of (benzene and toluene)/He/H_2; total flow rate of ~3.4 $cm^3\ s^{-1}$) were carried out using ~0.34 g Mo_2C (~200 μmol g_{cat}^{-1} CO chemisorption sites) at ~353 K and ambient pressure, in which Mo_2C was pretreated in H_2 (~1.67 $cm^3\ s^{-1}$) at 723 K for 1 h before hydrogenation reactions. A lower temperature (~353 K) than that for HDO reactions (533–553 K) was chosen to allow for kinetic measurements of in situ titration experiments at differential conversion (<10%). After steady state rates of cyclohexane and methylcyclohexane were observed, a co-feed of methanol or water in argon (methanol or water/Ar of 11.5 or 24.5/balance (vol%) at a total flow rate of ~0.17 $cm^3\ s^{-1}$) was introduced, while simultaneously removing He to maintain the same total flow rate. The transient responses of the titrant, Ar, cyclohexane, and methylcyclohexane were tracked using an online mass spectrometer (MKS Cirrus 200 Quadrupole mass spectrometer system). The concentrations of reactants and products were quantified by GC before and after the titration.

3.3. Results and discussion

3.3.1. Materials characterization

β-Mo_2C was identified as the major carbidic phase for a passivated Mo_2C catalyst based on the observed diffraction peaks shown in Figure 3.1, consistent with previous reports.[56,127,128] We note that the passivated Mo_2C catalyst was aged in a vial under ambient conditions for ~1 month prior to the XRD analysis.

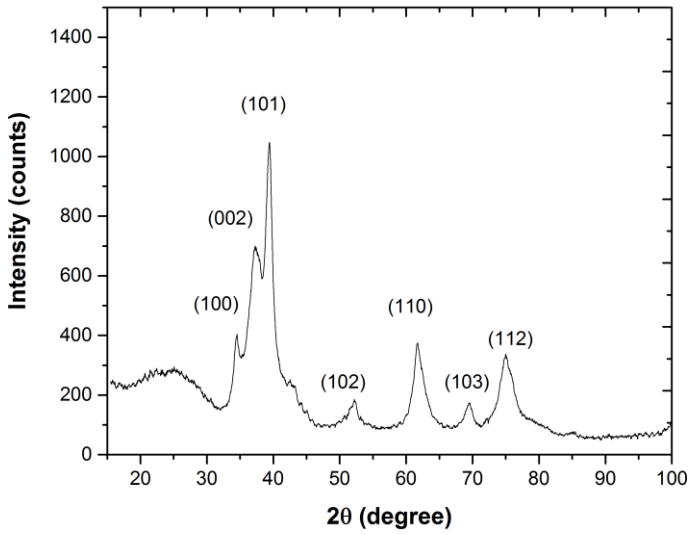

Figure 3.1 X-ray diffraction pattern of a Mo_2C catalyst. The sample was treated in a flow of 1% O_2/He mixture (~1.67 cm^3 s^{-1}) for ~2 h at RT and was aged for ~1 month in a vial under ambient conditions prior to XRD analysis.

The BET surface area for the same catalyst, aged for ~2.5 months, was ~116 m^2 g_{cat}^{-1}, in which the sample was treated in pure H_2 (~1.67 cm^3 s^{-1}) at 723 K for 1 h, passivated in 1% O_2 in He, and immediately loaded in a cell for BET measurement, however, the surface area for the same sample, directly loaded for BET measurement without H_2 pretreatment, was found to be ~23 m^2 g_{cat}^{-1}. The amount of irreversibly chemisorbed CO at ~323 K of the same Mo_2C sample, aged for ~2.5 months, was 108 μmol g_{cat}^{-1} (STP). Porous features of the fresh Mo_2C catalysts and TEM analysis were reported in our previous work.[56,127]

The crystallite size of the fresh but passivated Mo_2C was ~7.3 nm, which was estimated using the Scherrer equation for the 2θ peak at ~52º. This is comparable to both our previous report (~3.3nm)[127] and the Mo_2C catalysts reported by Boudart and coworkers (~5.8 and 11.5 nm).[41] The particle size of a typical fresh but passivated sample is ~70 nm, estimated using the equation $D_p = \sim 6 \times (\rho \times Sa)$, where ρ is taken as 770 kg m^{-3}.[129] These results suggest that the catalyst is polycrystalline.

Lee et al.[128] reported a significant loss in chemisorbed CO uptake (~250 to ~130 μmol g_{cat}^{-1}) and BET surface area (~125 to ~25 m^2 g_{cat}^{-1}) measured on samples that were not pretreated in H_2 over an initial ~10 day period; no significant change in surface area or CO adsorption capacity was noted over a subsequent aging time of ~4 months. The number of times that the sample was exposed to air, instead of the shelf life was attributed to be a more relevant descriptor for the loss in both CO uptake and BET surface area.[128] Chemisorbed CO uptake for the samples used in this study were, therefore, measured within 7 days before each reaction; the BET surface area (~106 m^2 g_{cat}^{-1}) used specifically for calculating the number of surface Mo atoms on molybdenum carbide catalysts in the titration experiments (Section 3.3.4) was an average value taken from two independent BET measurements of two batches of Mo_2C, each aged for ~2.5 months and ~1.5 months, with a H_2 pretreatment (~1.67 cm^3 s^{-1}) at 723 K as discussed above.

3.3.2. Vapor phase HDO of phenolic compound mixtures on Mo_2C

Figure 3.2 shows product selectivity and conversion for vapor phase HDO of a phenolic compound mixture comprised of m-cresol, anisole, DMB, and GUA (molar ratio = 1: 0.96: 0.95: 0.98) over ~0.02 g Mo_2C at 553 K under ambient pressure. Concurrent high conversion (95%), and high selectivity to BTX, at a level of ~95%, were achieved with low selectivity (<10% on a molar basis) to sequential hydrogenated products. No indication of catalyst deactivation over the course of 6 h was observed, which distinguishes Mo_2C catalysts from alumina supported Pt catalysts[118] and silica-supported nickel phosphide catalysts[121] that deactivated ~15% in 4 h at 523 K and ~40% in 10 h at 573 K, respectively for m-cresol and guaiacol HDO reactions.

A comparison of specific BTX yield from vapor phase HDO of guaiacol/phenolic compounds mixture on different catalysts is shown in Table 3.1. We note, however, that the tabulated values were reported from HDO reactions (i) using different phenolic compounds as reactants, and (ii) at varying reaction temperatures and conversions.

Table 3.1 Specific yield of benzene and toluene from vapor phase HDO of guaiacol/anisole/phenolic compound mixtures at 1 bar.

Catalyst	Reaction Temperature (K)	Space Velocity ($g_{phenolic\ compound}$ g_{cat}^{-1} h^{-1})	Conversion (%)	Phenolic Compound	Yield of benzene and toluene ($\times 10^{-7}$ mol g_{cat}^{-1} s^{-1})
15 wt% Fe/SiO_2[126]	673	0.13	100	Guaiacol	1.2
Ni_2P/SiO_2[123]	573	0.06	80	Guaiacol	0.6
Co_2P/SiO_2[123]	573	0.02	70	Guaiacol	0.1
MoO_3[25]	593	3.5	73	Guaiacol	16
Mo_2C[127]	553	2.6	-	Anisole	40[a]
Mo_2C	553	5.5	95	Phenolic mixture[b]	14

[a] The specific yield of benzene at 553 K is extrapolated from benzene turnover rate at 423 K using apparent activation energy (~70 kJ mol^{-1}) reported by Lee et al.[127]

[b] Molar ratio of m-cresol: anisole: DMB: GUA = 1: 0.96: 0.95: 0.98; Feed = phenolic mixture (0.03)/ H_2 (91)/ He balance (vol%); space velocity 198 cm^3 s^{-1} g_{cat}^{-1}.

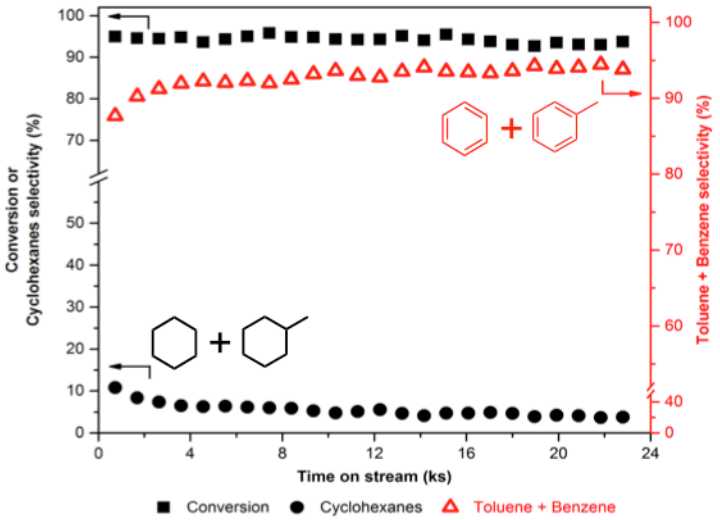

Figure 3.2 Conversion and product selectivity for HDO of a phenolic compound mixture over ~0.02 g_{cat} Mo_2C. Molar ratio of m-cresol: anisole: DMB: GUA = 1: 0.96: 0.95: 0.98; Feed = phenolic mixture (0.03)/ H_2 (91)/ He balance (vol%) at 114 kPa total pressure and at 553 K; space velocity 198 cm^3 s^{-1} g_{cat}^{-1}; ex situ CO uptake = 124 μmol g_{cat}^{-1}; Cyclohexanes contains methylcyclohexane and cyclohexane.

Figure 3.3 shows the molar ratios of toluene and benzene, defined as specified in Equation 3.3, for vapor phase HDO of phenolic compound mixtures with different compositions over Mo_2C at 533–553 K and quantitative conversion (~100%). Toluene molar ratio was found to increase with the m-cresol content in the mixture, suggesting that toluene synthesis was dominated by direct HDO of m-cresol. The predicted molar ratios of toluene to benzene (Figure 3.3), assuming that toluene and benzene were produced from complete HDO of m-cresol, and from complete HDO of anisole, DMB, and GUA, respectively, were found to be consistent (<±10%) with the ratios measured experimentally from the reactor effluents, which confirms that (i) molybdenum carbide catalysts can exclusively and quantitatively cleave the aryl-oxygen bonds in phenolic compounds, and (ii) the extent of transalkylation was insignificant under the given reaction conditions, as quantitative synthesis of the corresponding aromatics was observed. The low selectivity to transalkylation products (~3% selectivity to toluene from mixture M1 at quantitative conversion) during HDO of phenolic compound mixtures on Mo_2C contrasts vapor phase

HDO of phenolic model compounds such as m-cresol, guaiacol, and anisole on bimetallic Ni-Fe,[130] monolithic Pt-Sn,[119] MoO_3,[25] and carbon-supported Pd-Fe[131] catalysts, in which the selectivity to transalkylation products was found to be ~12%–50%.

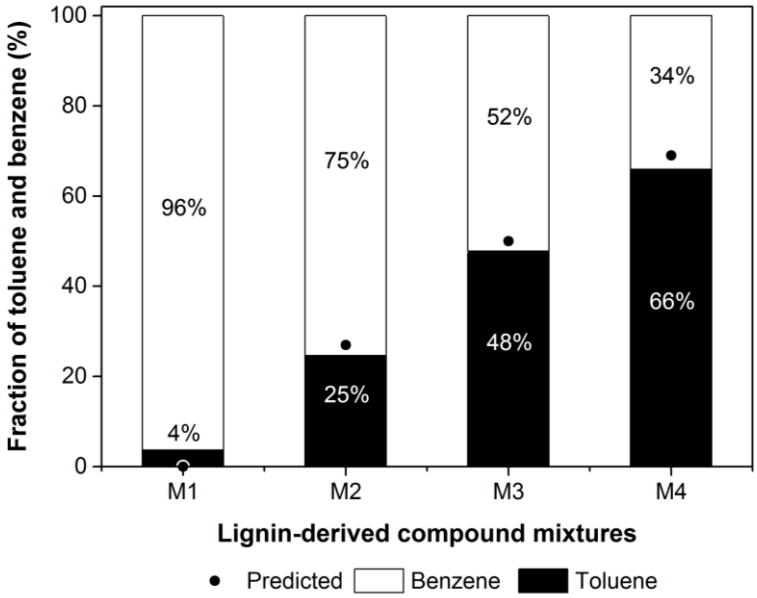

Figure 3.3 Fraction of toluene and benzene, defined as molar flow rate of (toluene or benzene)/ (toluene + benzene) × 100%, from reactor effluents of HDO reactions at different mixture compositions at quantitative (100%) conversion on 0.1 g Mo_2C under ambient pressure at 533 K for M2 and M3 (ex situ CO uptake = 224 μmol g_{cat}^{-1}), and 553 K for M1 and M4 (ex situ CO uptake = 135 μmol g_{cat}^{-1}); (•) predicted toluene fractions from the compositions of mixtures, assuming that m-cresol was completely deoxygenated to toluene, while anisole, DMB, and GUA were deoxygenated to benzene. Molar compositions of phenolic compound mixtures [m-cresol: anisole: DMB: GUA] = 0: 0.35: 0.35: 0.3 (M1); 1: 0.96: 0.95: 0.82 (M2); 1: 0: 0.95: 0 (M3); 1: 0.16: 0.16: 0.13 (M4). Feed (M1 and M4) = phenolic mixture (0.03)/ H_2 (91)/ He balance (vol%) at 114 kPa total pressure; space velocity ~36.6 $cm^3\ s^{-1}\ g_{cat}^{-1}$. Feed (M2 and M3) = phenolic mixture (0.07 and 0.15)/ H_2 (77)/ He balance (vol%) at 108 kPa total pressure; space velocity ~19.0 $cm^3\ s^{-1}\ g_{cat}^{-1}$.

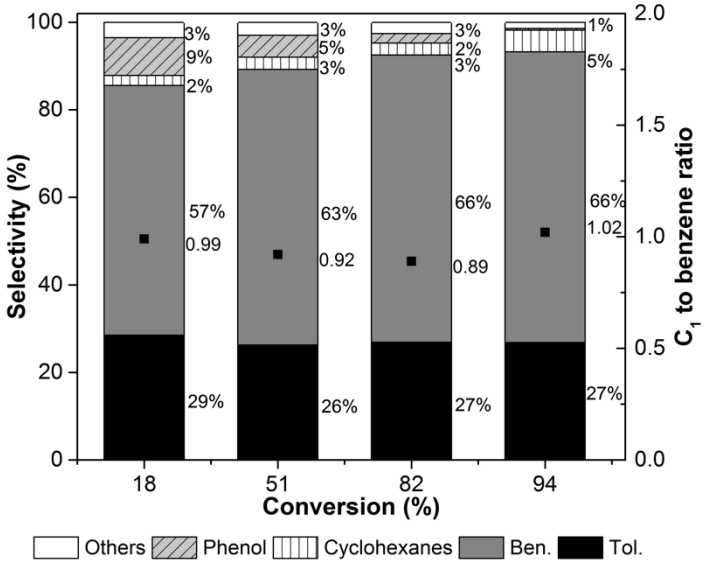

Figure 3.4 Selectivity for HDO of phenolic compound mixtures and molar ratio of C_1 products (methane and methanol) to benzene at different conversions (18–94%). Molar ratio of m-cresol: anisole: DMB: GUA = 1: 0.96: 0.95: 0.98; Feed = phenolic mixture (0.03)/ H_2 (91)/ He balance (vol%) at 114 kPa total pressure and at 553 K; Selectivity reported is an average value taken between ~3.6–21 ks time-on-stream; Different conversions were achieved by using different mass of catalyst (1.9–18.5 mg, ex situ CO uptake ~124 μmol g_{cat}^{-1}); space velocities 198–1.9 × 10^3 cm^3 s^{-1} g_{cat}^{-1}; Cyclohexanes contains methylcyclohexane and cyclohexane; Others contains unidentified C_6^+ hydrocarbons, which were quantified using benzene, anisole, or m-cresol, depending on the retention time of the species in the GC chromatogram.

3.3.3. Reaction pathways for lignin-derived phenolic compounds on Mo_2C

The selectivity to phenol (Figure 3.4) decreased from 9% to 0.3% as the total conversion of the phenolic mixture (molar ratio of m-cresol, anisole, DMB, and GUA = 1: 0.96: 0.95: 0.98) increased from 18% to 94%, suggesting that the Ar–OCH_3 bond in GUA was preferentially cleaved before the Ar–OH bond. Negative conversion of anisole, calculated using Equation 3.4, was observed at 18% total conversion (Figure 3.6 in Section 3.5), indicating that the Ar–OCH_3 bond in DMB was first cleaved to form anisole, before it was further deoxygenated to form benzene (Scheme 3.1). These experimental observations are in line with recent computational chemistry calculations of bond

dissociation energies (BDE) of GUA,[25] showing that the Ar-OH bond (~456 kJ mol^{-1}) is stronger than the Ar–OCH_3 bond (~376 kJ mol^{-1}). The product selectivity and conversion were stable over 6 h time-on-stream (TOS) at all conversions (18–94%) investigated (Figure 3.2, and Figure 3.7 in Section 3.5). We note that unidentified C_6^+ compounds were observed (collectively denoted as "Others" in Figure 3.4) and were quantified using benzene, anisole, or m-cresol, depending on the retention time of the species in the GC chromatogram.

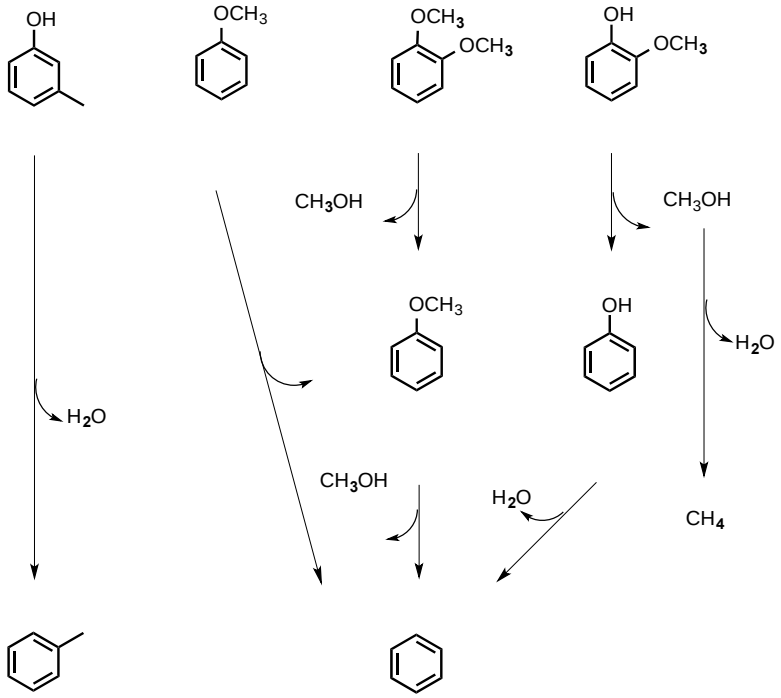

Scheme 3.1 Reaction pathways for hydrodeoxygenation of lignin-derived phenolic compound mixtures comprising m-cresol, anisole, 1,2-dimethoxybenzene, and guaiacol on molybdenum carbide catalysts.

3.3.4. Oxygen modified surface for selective HDO on Mo_2C

The catalytic activity of freshly prepared bulk or supported molybdenum carbide catalysts in benzene hydrogenation reactions has been reported to be comparable to noble metal catalysts such as Ru/Al_2O_3 or Pt/Al_2O_3.[7,132] Choi et al.[7] reported that site time yield (STY, normalized by ex-situ CO chemisorption sites) of benzene hydrogenation at room temperature was 0.09 s^{-1} on Mo_2C catalysts, and 0.35 s^{-1} on a commercial Ru/Al_2O_3 sample.

Similarly, bulk molybdenum carbide catalysts have also been shown to be active for toluene hydrogenation at 423–598 K and ~3 MPa H_2 pressure, in which 100% toluene conversion was achieved at 473 K.[133,134]

Low selectivity to cyclohexane and methylcyclohexane (<10% at <100% conversion) observed in HDO of phenolic mixtures, as shown in Figure 3.2, suggests that successive hydrogenation reactions of the corresponding HDO products, toluene and benzene, on Mo_2C were significantly suppressed even at temperatures (533–553 K) much higher than RT, and high hydrogen to oxygenate molar ratio (~3,300). Hydrogenation reactions of an equimolar mixture of benzene and toluene on the molybdenum carbide catalyst were, therefore, investigated. In situ titration via oxygen-containing compounds, specifically, methanol and water, was implemented to probe the hydrogenation functionality, and to assess hydrogenation turnover frequency of benzene and toluene on Mo_2C at 353 K. Methanol or water was co-fed to the system after steady state rates of cyclohexane and methylcyclohexane synthesis were obtained (<10% conversion). Figure 3.5 shows the mass spectrometric signals of cyclohexane, methylcyclohexane, methanol or water, and Ar normalized to their corresponding values at steady state, as a function of time during the titration experiments. The signals of cyclohexane and methylcyclohexane dropped to <1% of their steady state values in presence of the titrants, showing that hydrogenation rates of benzene and toluene were almost completely inhibited by methanol or water, and not recovered upon the removal of titrants at 353 K. These experimental results suggest that the introduction of oxygen-containing compounds, such as lignin-derived phenolic compounds, CO and water, which are typically observed in pyrolysis vapor,[135,136] to Mo_2C under HDO reaction conditions (533–553 K) can irreversibly and significantly inhibit hydrogenation of aromatic rings, resulting in high product selectivity to aromatics in HDO reactions of phenolic compound mixtures.

The activity of benzene/toluene hydrogenation reactions on molybdenum carbide catalysts was evaluated in terms of turnover frequency (TOF). The TOF of benzene and toluene hydrogenation was obtained by normalizing the synthesis rates of cyclohexane and methylcyclohexane at steady state to the number of the adsorption sites occupied by the

titrant. The latter can be assessed by calculating the area between normalized mass spectrometric signals of Ar and the titrant, as shown in Figure 3.5, and multiplying it by a known titrant flow rate (2.2×10^{-4} mol of H_2O; 2.8×10^{-4} mol of CH_3OH).[137] Alternatively, the number of active sites could be evaluated using the time that is required to bring the signals of cyclohexane and methylcyclohexane to zero (Figure 3.5), and multiplying it by a known titrant flow rate (2.2×10^{-4} mol of H_2O; 2.8×10^{-4} mol of CH_3OH). Both methods gave similar number of adsorption sites (±5%, Table 3.2 in Section 3.5). The resulting TOF for benzene and toluene hydrogenation at 353 K is ~2.5×10^{-4}–6×10^{-4} s^{-1}. The effective site density for benzene and toluene hydrogenation reactions prior to the in situ titration was, therefore, ~7×10^{2} μmol g_{cat}^{-1}, which corresponds to ~40% of surface Mo atoms, using a surface area of ~106 m^2 g_{cat}^{-1} for a typical aged sample after pretreatment in H_2 (~1.67 cm^3 s^{-1}) at 723 K and Mo atom density of 1×10^{15} cm^{-2}.[7]

The reported TOF for benzene/toluene hydrogenation at ~353 K is about two orders of magnitude lower than that reported by Choi et al.[7] at room temperature. One possible reason for the lower TOF is that the molybdenum carbide sample used in the current study had been previously passivated using 1% O_2/He before being reactivated in H_2 at 723 K, whereas Choi et al.[7] used freshly prepared catalysts (without exposure to air) for benzene hydrogenation. In an independent study, Choi et al.[40] noted that a passivated Mo_2C sample treated in H_2 at 773 K showed only 1% conversion in benzene hydrogenation, as compared to ~100% conversion measured from a freshly prepared formulation, consistent with our experimental observation that Mo_2C was completely inactive for hydrogenation reactions of toluene and benzene after being exposed to methanol or water.

High selectivity to the direct HDO product, 2-methylfuran (~60%), but low selectivity to the furfural hydrogenation product, furfural alcohol (~7%), has been reported by Xiong et al.[18,138] in furfural HDO on molybdenum carbide catalysts. The high deoxygenation selectivity of furfural HDO on Mo_2C was attributed to the strong interaction between the C=O group in furfural, the favored binding configuration, and the Mo_2C surface, as adduced by density functional theory (DFT) calculations where the binding energy (BE) of furfural on a close-packed $Mo_2C(0001)$ (3.54 eV) surface was found to be higher than that

on a Pt(111) (0.66 eV) surface.[138] High-resolution electron energy loss spectroscopy (HREELS) measurements of furfural, furfural alcohol, and 2-methylfuran on Mo_2C suggested that the selective C=O scission is likely to proceed through an η^2(C,O) bonding configuration,[138] and the conjugation between the five-membered aromatic ring and the C=O bond could be disrupted, increasing the propensity for the molecule to undergo deoxygenation rather than hydrogenation/dehydrogenation.[18] By analogy, we suggest that high selectivity to BTX (>90%) in HDO of phenolic compound mixtures on Mo_2C may be a consequence of the phenolic reactants binding/adsorbing in a configuration that is favorable for preferential cleavage of the stronger Ar–OCH_3 bond relative to the weaker ArO–CH_3 bond, i.e., the Ar–O bond of the phenolic compounds interacts strongly with the Mo_2C surface, and the aromatic ring helps weaken the Ar–O bond.[139]

The slow increase in BTX selectivity with time-on-stream (90% to 95%) is noted to be at the expense of cyclohexanes selectivity with TOS (10% to 5%), as shown in Figure 3.2, which arises presumably due to a gradual and continuous modification of the catalyst surface by the oxygen-containing phenolic reactants during HDO. The total conversion of the phenolic compound mixture, however, was nearly invariant within the course of the reaction as cyclohexane selectivity decreased from 10% to 5%, suggesting that modification of the Mo_2C surface from the phenolic compounds has little or no effect on the catalytic sites for aryl-oxygen bond cleavage.

The observed inhibition of aromatic hydrogenation functionality on Mo_2C during HDO reactions was found to be correlated with in situ oxygen-modification as discussed above, however, the X-ray diffraction (XRD) pattern of the spent catalyst used for in situ methanol titration shows no peaks assigned to MoO_2, and/or MoO_3, suggesting that bulk oxidation of the molybdenum carbide did not occur. β-Mo_2C phase was identified in the spent catalyst (Joint Committee on Powder Diffraction Standards, no. 35-0787, 2θ peaks at ~34.355° (100), 37.979° (002), 39.393° (101), 52.124° (102), 61.529° (110), 69.567° (103)), which evidenced that the bulk phase of the catalyst remained as Mo_2C (Figure 3.8 in Section 3.5) and that the oxygen modification occurred only in the surface and/or subsurface region.

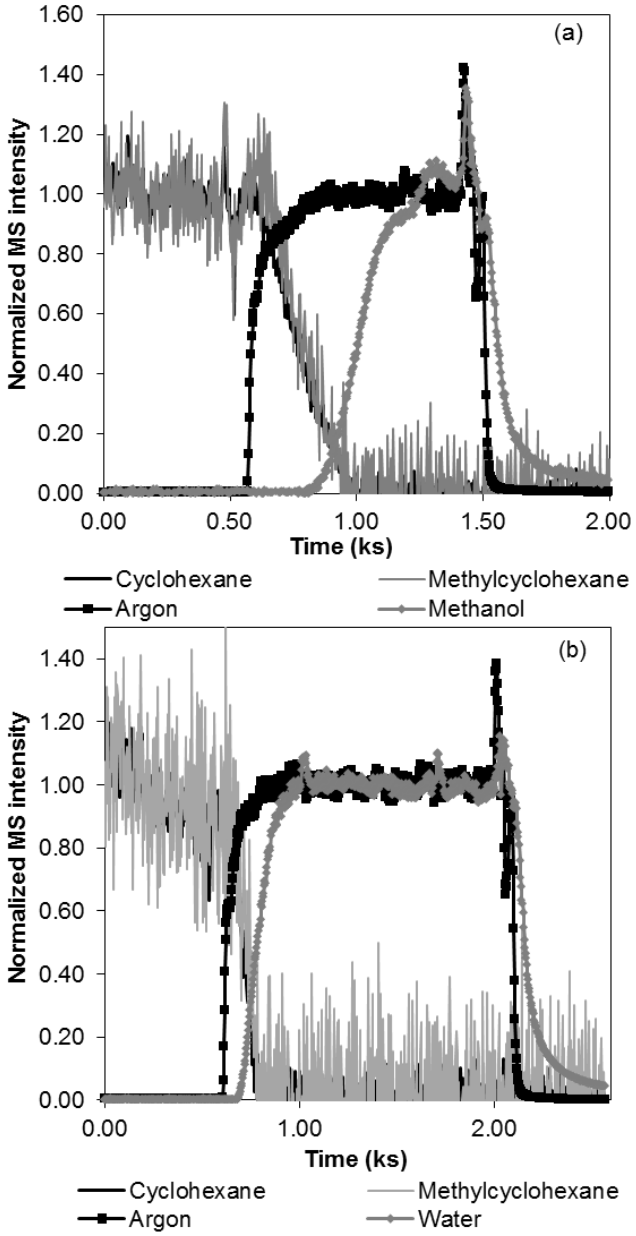

Figure 3.5 Mass spectrometric signals of methylcyclohexane and cyclohexane normalized to the signals at steady state as a function of time with a titrant co-feed consisting of (a) methanol/ argon (11.5/balance, vol%) and (b) water/ argon (24.5/balance, vol%) gas mixture (total flow rate ~0.17 $cm^3\ s^{-1}$), in which Ar was used as an internal standard. Hydrogenation reaction conditions: equimolar mixture of (benzene and toluene)/He/H_2 (vol%) = 1.2/4.9/balance, with ~0.34 g_{cat} (ex situ CO uptake ~200 μmol g_{cat}^{-1}) and space velocity of ~10 $cm^3\ s^{-1}\ g_{cat}^{-1}$ at ~353 K under ambient pressure.

3.4. Conclusions

Lignin-derived phenolic compound mixtures (anisole, m-cresol, guaiacol, and 1,2-dimethoxybenzene) can be selectively converted to the corresponding completely deoxygenated aromatics (benzene and toluene) with high yield (>90%) and high hydrogen efficiency (<10% selectivity for unwanted sequential hydrogenation products) via vapor phase HDO over molybdenum carbide catalysts at mild reaction temperatures (~533–553 K) and ambient pressure. The methoxyl group in guaiacol was preferentially cleaved prior to the removal of the hydroxyl group, which is in line with the higher bond dissociation energy of Ar–OH (~456 kJ mol^{-1}) relative to $Ar–OCH_3$ (~376 kJ mol^{-1}) in lignin-derived phenolic compounds.[25] In situ methanol and/or water titration of benzene/toluene hydrogenation reactions suggest that the inhibition of aromatic hydrogenation functionality on Mo_2C during HDO reactions is a result of in situ modification of the catalyst surface by oxygenates. These experimental results demonstrate a feasible approach to directly upgrade pyrolysis vapor without the expense of noble metal catalysts and the use of severe reaction conditions (high H_2 pressure and/or high temperatures).

3.5. Supporting information

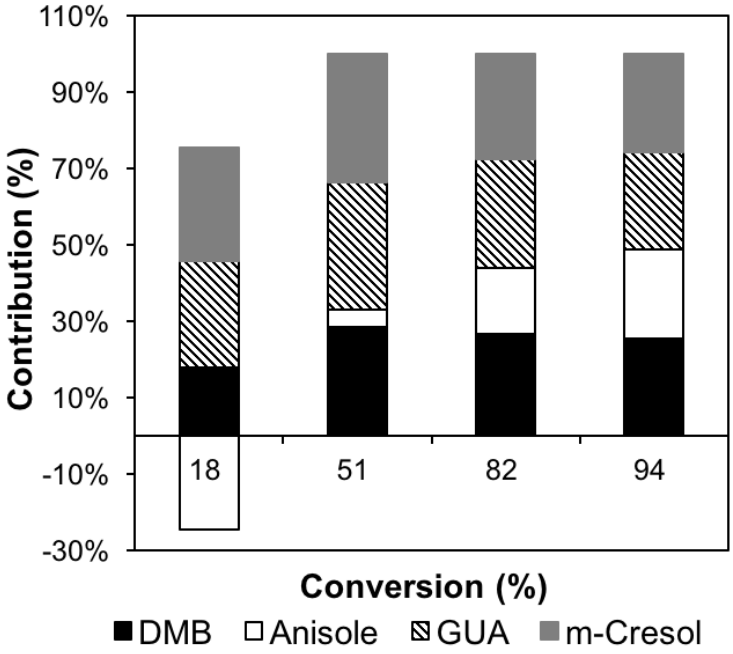

Figure 3.6 Contributions of individual conversion of each phenolic compound to the overall conversion of the phenolic mixture over Mo_2C at 553 K and 114 kPa total pressure. Molar ratio of m-cresol: anisole: DMB: GUA = 1: 0.96: 0.95: 0.98; Feed = phenolic mixture (0.03)/ H_2 (91)/ He balance (vol%); Different conversions were achieved by using different mass of catalyst (1.9–18.5 mg); space velocities: 198–1.9×10^3 cm^3 s^{-1} g_{cat}^{-1}; ex situ CO uptake 124 μmol g_{cat}^{-1}. Individual conversion is defined as [(moles of C in phenolic reactant i)$_{in}$– (moles of C in phenolic reactant i)$_{out}$]/(moles of C in phenolic reactant i)$_{in}$.

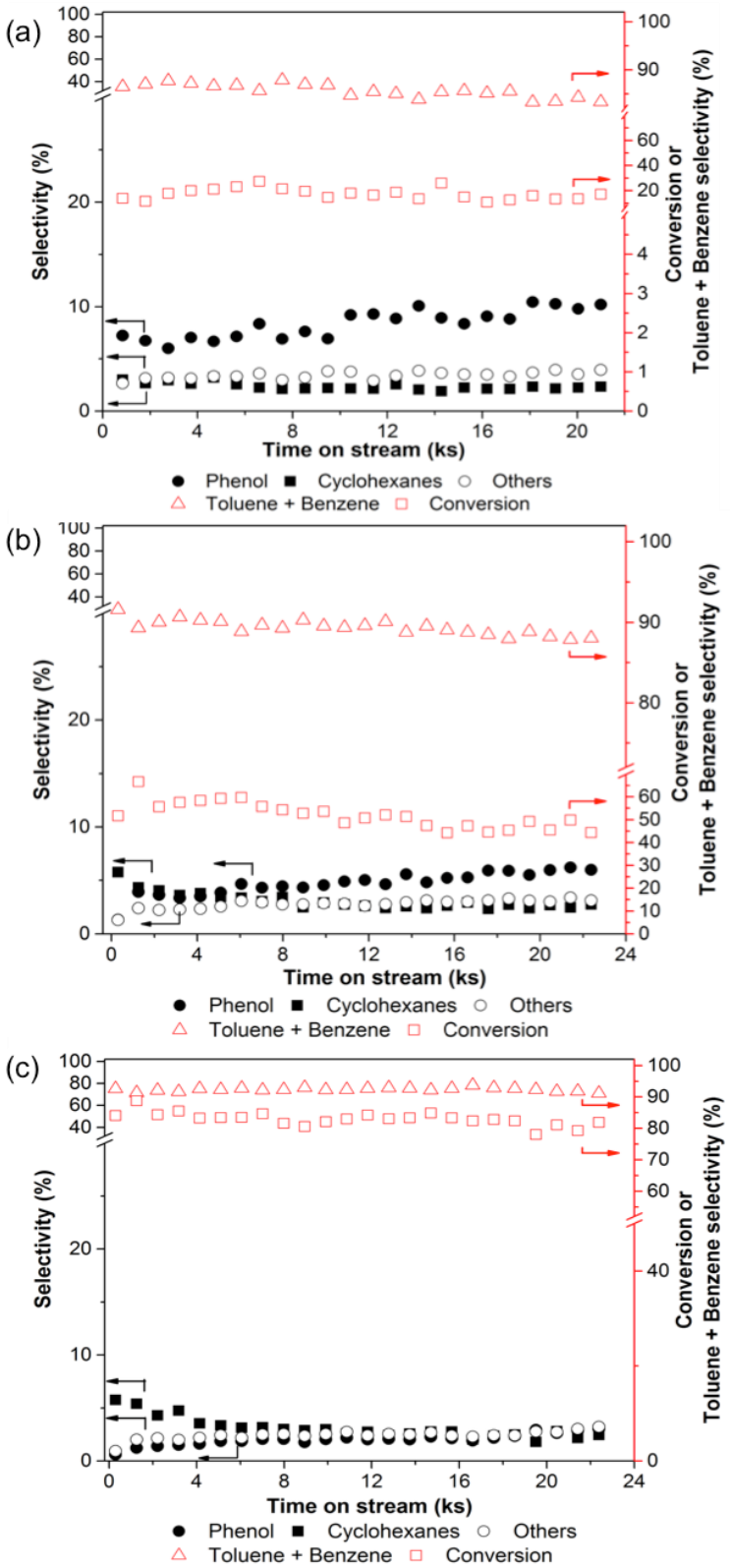
(a)
Selectivity (%)
Conversion or
Toluene + Benzene selectivity (%)
Time on stream (ks)
Phenol
Cyclohexanes
Others
Toluene + Benzene
Conversion
(b)
Selectivity (%)
Conversion or
Toluene + Benzene selectivity (%)
Time on stream (ks)
Phenol
Cyclohexanes
Others
Toluene + Benzene
Conversion
(c)
Selectivity (%)
Conversion or
Toluene + Benzene selectivity (%)
Time on stream (ks)
Phenol
Cyclohexanes
Others
Toluene + Benzene
Conversion

Figure 3.7 Conversion and product selectivity for HDO of phenolic compound mixtures at (a) 18%, (b) 51%, and (c) 82% conversion. Molar ratio of m-cresol: anisole: DMB: GUA = 1: 0.96: 0.95: 0.98; Feed = phenolic mixture (0.03%)/ H_2 (91%)/ He balance (vol%) at 114 kPa total pressure and at 553 K; Conversions are averaged values taken after 3.6 ks time-on-stream, after steady state was established; Different conversions were achieved by using different mass of catalyst (1.9–11.3 mg); space velocities: 198–1.9×10^3 cm^3 s^{-1} g_{cat}^{-1}; ex situ CO uptake 124 μmol g_{cat}^{-1}; Cyclohexanes contains methylcyclohexane and cyclohexane; Others contains unidentified C_6^+ hydrocarbons, which were quantified using benzene, anisole, or m-cresol, depending on the retention time of the species in the GC chromatogram.

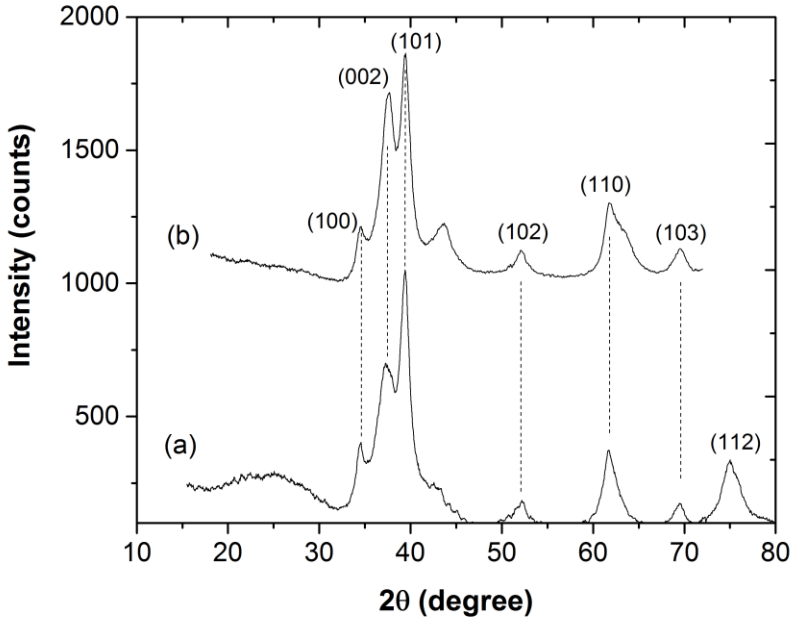

Figure 3.8 X-ray diffraction patterns of (a) fresh Mo_2C which was treated in a flow of 1% O_2/He mixture (~1.67 cm^3 s^{-1}) for ~2 h at RT and was aged for ~1 month in a vial under ambient conditions prior to XRD analysis, and (b) spent Mo_2C from in situ methanol titration experiment during steady state benzene/ toluene hydrogenation reactions. Hydrogenation reaction conditions: equimolar mixture of (benzene and toluene)/He/H_2 (vol%) = 1.2/4.9/balance, with ~0.34 g_{cat} (ex situ CO uptake ~200 μmol g_{cat}^{-1}) and space velocity of ~10 cm^3 s^{-1} g_{cat}^{-1} at ~353 K under ambient pressure. The titrant co-feed consists of methanol/ argon (11.5/balance, vol%) at a total flow rate of ~0.17 cm^3 s^{-1}.

Table 3.2 Number of adsorption sites measured from in situ CH_3OH and H_2O titration of benzene/ toluene hydrogenation reactions on Mo_2C.[†]

Titrant	Method 1[a] ($\times 10^{-4}$ mol)	Method 2[b] ($\times 10^{-4}$ mol)	Difference[c] (%)
CH_3OH	2.8	2.8	0
H_2O	2.2	2.1	4.5

[†]Hydrogenation reaction conditions: equimolar mixture of (benzene and toluene)/He/H_2 (vol%) = 1.2/4.9/balance, with ~0.34 g_{cat} (ex situ CO uptake ~200 μmol g_{cat}^{-1}) and space velocity of ~10 $cm^3\ s^{-1}\ g_{cat}^{-1}$ at ~353 K under ambient pressure. Titrant co-feed consists of methanol/ argon (11.5/balance, vol%) or water/ argon (24.5/balance, vol%) gas mixture (total flow rate ~0.17 $cm^3\ s^{-1}$).

[a] The number of adsorption sites was assessed by calculating the area between normalized mass spectrometric signals of Ar and the titrant (methanol or water, see Figure 3.5), and multiplying it by a known titrant flow rate.

[b] The number of adsorption sites was evaluated using the time required to bring the signals of cyclohexane and methylcyclohexane to zero (Figure 3.5), and multiplying it by a known titrant flow rate.

[c] The difference of the reported adsorption sites between the two methods as described above.

3.6. Acknowledgements

This research was supported by Office of Basic Energy Sciences, the U.S. Department of Energy under award number DE-SC0008418 (DOE Early Career Program). We thank Ms. Seema Thakral for assistance with the X-ray diffraction studies

4. Ordered mesoporous metal carbides with enhanced anisole hydrodeoxygenation selectivity*

4.1. Introduction

Biomass has received considerable attention as a green carbon feedstock for chemical and fuel production.[38,39,140] Distinct from petroleum-derived chemicals, biomass contains highly oxidized carbon compounds, which are not desired for the existing chemical industry.[39,140] Many efforts have been devoted into identifying suitable catalysts that can selectively break C–O bonds in biomass molecules during hydrodeoxygenation (HDO) processes.[141–143] A variety of catalysts, such as metals, bimetallics, metal sulfides, and metal carbides, have been investigated as potential candidates for selective HDO.[39,140] Among them, metal carbides have shown promising properties in selective HDO of biomass-derived oxygenates to unsaturated hydrocarbons.[19,144] For example, Lee et al.[54,127] recently discovered that molybdenum carbide can selectively remove oxygen without attacking the aromatic ring in the vapor phase anisole HDO reaction, leading to a ~90% benzene selectivity and a ~9% cyclohexane selectivity simultaneously. More importantly, the high benzene selectivity was achieved at atmospheric pressures of hydrogen and at reaction temperatures (420–520 K) significantly lower than the typical HDO reaction temperatures (500–700 K). It clearly demonstrated the great promise of metal carbides as selective HDO catalysts for biomass-derived oxygenate upgrading.

Ordered mesoporous metal-containing materials are potential candidates as model heterogeneous catalysts, because they have large surface areas, nano-sized walls, and well defined three-dimensionally porous structures.[145–148] The self-supported structure eliminates the requirement of an inert support that is commonly used in traditional nanoparticle catalysts. By doing so, it not only suppresses sintering and segregation in harsh catalytic environments, but also enables fundamental studies of intrinsic catalytic rates and selectivities without the interference of support effects. A general synthetic

*Reprinted with permission from ACS Catal., 2016, 6 (6), pp 3506–3514. Copyright 2016 American Chemical Society.

"nanocasting" method (also called "hard templating") has been established to fabricate a wide range of metal oxides.[149,150] An "oxide-to-sulfide" approach to convert metal oxides further to metal sulfides with preservation of the ordered mesostructure was recently developed.[151] Three ordered mesoporous metal sulfides, i.e., FeS_2, NiS_2, and CoS_2, have been synthesized by this method as potential catalyst candidates for desulfurization and photocatalytic reactions.

While the "oxide-to-sulfide" phase transformation method worked very well for mesoporous metal sulfides, this method has had limited success in the preparation of metal carbide formulations with ordered mesoporosity. To date, only a few examples of mesoporous metal carbides have been reported.[152–154] Attempts to carburize metal oxides inside a porous silica template failed to produce pure metal carbides with ordered porous structures, which is likely due to the difficulty of carbon diffusion across partially carburized particles, leading to carbon accumulation on the surface of metal carbide particles. Herein, the synthesis of molybdenum and tungsten carbides (i.e., Mo_2C and W_2C) with three-dimensionally ordered mesoporous structures through a one-step carburizing process using methane as the sole carbon source as well as the reductant is reported. The concurrence of metal precursor decomposition and methane-assisted carburization inside the silica template nanopores enables the formation of phase pure metal carbides with ordered mesoporous structures at relatively low annealing temperatures. Catalytic HDO studies confirmed the superior properties of ordered mesoporous Mo_2C and W_2C. Mesoporous W_2C catalyst exhibited greater than 96% selectivity to benzene from anisole HDO at 423 K, representing the highest benzene selectivity reported to date.

4.2. Experimental section

4.2.1. Synthesis of mesoporous metal carbides

The synthesis of the mesoporous silica template, KIT-6, was described previously in the literature.[155] In a typical synthesis of mesoporous Mo_2C, a highly concentrated molybdenum precursor solution was first prepared by dissolving 10 g of phosphomolybdic

acid hydrate (ACS reagent, Sigma-Aldrich) in 2.5 cm^3 of de-ionized water. In a separate beaker, 2 g of KIT-6 was dispersed in 20 cm^3 of dry n-hexane. Under vigorous stirring, 4 g of concentrated molybdenum precursor solution was added slowly into the KIT-6/hexane suspension. The mixture was stirred in an open beaker inside a hood until a fully dried powder was obtained. The powder was then transferred to an alumina crucible and treated at 923 K for 5 hours under a continuous methane flow (flow rate: ~0.5 cm^3 s^{-1}). After cooling down to room temperature, the sample was treated in 10 wt% HF solution three times to remove the silica template, followed by washing with de-ionized water repeatedly and drying in an oven at 313 K. In the case of mesoporous W_2C, phosphotungstic acid hydrate (reagent grade, Sigma-Aldrich) was used as the tungsten precursor and the rest of the procedure remained the same. The samples are stable in the ambient environment after the carburization process, hence, passivation is not required, similar to observations reported in the literature using solution-derived synthesis approaches to prepare transition metal carbides.[156,157] Alternatively, during the removal of the silica template the exposed metal carbide surface is likely oxidized by water or the dissolved oxygen in solution, which results in the formation of a passivation layer on the carbide.

4.2.2. Structural characterizations

Scanning electron microscopy (SEM) measurements were carried out using JEOL JSM-7400F. A JEOL JEM-2010F with an accelerating voltage of 200 kV was used for transmission electron microscopy (TEM) analysis. Powder X-ray diffraction (PXRD) measurements were performed on a Rigaku Ultima IV X-ray diffractometer with Cu Kα radiation. A Thermo Scientific K-Alpha X-ray Photoelectron Spectrometer (XPS) System was used for analyzing the surface stoichiometry of the resulting carbidic formulations. The XPS data were calibrated using the binding energy of adventitious carbon at 285 eV and analyzed using CasaXPS software and peaks were fitted using a Gaussian/Lorentzian product line shape and a Shirley background. For the N_2 adsorption-desorption experiments, the samples were first degassed under vacuum at 393 K overnight, and then tested on a Micromeritics 3Flex Surface Characterization Analyzer. Surface areas were

estimated by the Brunauer–Emmett–Teller (BET) method using the adsorption data at 0.05-0.35 P/P_0. Pore size distributions were calculated from desorption isotherms using the classical Barrett–Joyner–Halenda (BJH) model.

X-ray absorption spectroscopic (XAS) data were collected at beamline 5-BM-D of the Advanced Photon Source at the Argonne National Laboratory. The samples were mixed with a small amount of amorphous SiO_2 powder and sealed using Kapton tape for the XAS measurements. The XAS spectra were collected using a scanning profile with various step sizes and dwell times (Section 4.5). The free Demeter software package was used for all data processing, including raw data alignment, reduction, and post-processing (Athena).[158] The standard procedures of data processing can be found in the instruction manual of the Demeter software package. Energy measurements were calibrated to the known edge position of a pure metal foil (Mo K-edge at 20,000 eV and W L_3-edge at 10,207 eV). The E^0 points were selected by taking the second derivative of binding energies and choosing the energy at the zero crossing point.

4.2.3. Catalytic studies of vapor phase anisole hydrodeoxygenation

Steady state vapor phase catalytic anisole HDO reactions were carried out in a tubular quartz reactor (I.D. 10 mm) with a thermocouple inserted in the thermowell in the middle of reactor bed to monitor the reaction temperature, which was controlled by a Watlow Temperature Controller (96 series). Mesoporous molybdenum carbide (or tungsten carbide, pelletized and sieved with a size of 177-420 μm) sample (0.02-1.6 g) was first treated in pure H_2 (~1.67 $cm^3\ s^{-1}$) at 723 K (~0.1 K s^{-1}) for 1 h (or 6 h for W_2C), and then cooled to the reaction temperature. Subsequently, reactants (~1.67 $cm^3\ s^{-1}$, or ~3.33 $cm^3\ s^{-1}$ for W_2C) consisting of ~0.15 (or ~0.06 for W_2C)/balance (mol%) of anisole/H_2 were introduced. Anisole (Sigma, ReagentPlus, 99%) was added to the flow line using a syringe pump (KD Scientific, Model 100). All flow lines were heated to at least 398 K via resistive heating to prevent condensation of the compounds. Reactor effluents were analyzed by an online gas chromatograph (GC, Agilent 7890) equipped with a methyl-siloxane capillary

column (HP-1, 50 m × 320 μm × 0.52 μm) connected to a flame ionization detector. The temperature program employed for the GC oven is shown in Table 4.2 (Section 4.5). Detailed methods for carbon balance, anisole conversion, C_6^+ product selectivity, and C_1/C_6 ratio calculations can be found in the Section 4.5. The absence of external and internal mass transfer limitations was confirmed by the Mears' Criterion and the estimated Thiele modulus (Section 4.5).

Benzene synthesis rates, kinetic measurements and in situ titration studies for anisole HDO reported herein were obtained from the spent mesoporous Mo_2C and W_2C samples after H_2 treatment (~1.67 $cm^3\ s^{-1}$) at 723 K for 1 h and 6 h, respectively, and after ~6 h on stream in anisole/H_2 flow at which time the conversion was noted to be largely invariant with time.

4.2.4. In situ CO titration for vapor phase hydrodeoxygenation of anisole

In situ CO titration was carried out after steady state benzene synthesis rates from anisole HDO were reached. A co-feed of 1% CO in helium (total flow rate of ~0.08–0.14 $cm^3\ s^{-1}$) was introduced, in which He was used as an internal tracer to quantify the amount of CO adsorbed or reacted during the course of titration. The transient responses of CO and He were tracked using an online mass spectrometer (MKS Cirrus 200 Quadrupole mass spectrometer system). The concentrations of reactants and products were quantified by GC before and after CO co-feed. Repeated experiments of CO titrations were conducted using the same or different CO flow rates. Typical mass spectrometric signals for chemical titration studies are shown in Figure 4.6 (Section 4.5). Turnover frequencies (TOFs) of benzene production were calculated by dividing the difference in benzene synthesis rates without and with CO co-feed (ΔR_{diff}) by the amount of CO adsorbed (CO_{ads}), which was obtained by integrating the area circumscribed by the He and CO signals in the mass spectrometer and multiplying it by the corresponding CO flow rate. The amount of CO that is required to inhibit all active sites for benzene synthesis was estimated by scaling the calculated CO_{ads} linearly with the ratio of the drop in benzene rate, i.e., benzene synthesis

rates without CO co-feed, and ΔR_{diff}. Two assumptions are made: (i) CO adsorption is irreversible and far from equilibrium at low CO coverages, and (ii) all active sites behave the same as those in the CO breakthrough regime.

4.3. Results and discussion

4.3.1. Synthesis of mesoporous metal carbides

Synthesis of metal carbides, such as Mo_2C and W_2C, usually requires a thermal treatment at an elevated temperature, which makes it difficult to prepare mesoporous metal carbides through traditional soft-templating methods.[158] A nanocasting approach uses a mesoporous silica as a hard template, which makes it possible to synthesize porous materials at a relatively high temperature (1000–1100 K). Here, the "nanocasting" method with a simultaneous methane carburization process was combined to prepare two ordered mesoporous metal carbides, Mo_2C and W_2C, at an annealing temperature of 923 K. The synthesis used a three-dimensionally ordered mesoporous silica (KIT-6) as a hard template, which was loaded with a heteropoly acid precursor, followed by a thermal annealing process in the presence of a continuous methane flow to form the desired metal carbides. The silica template was removed by a 10% HF solution after carburization.

Notably, full conversion of the metal precursor to the desired metal carbide phase was achieved at a moderate temperature. It is likely because the silica template confined thermal decomposition of the heteropoly acid precursor inside the silica nanopores with pore diameters of 7–8 nm, greatly suppressed the formation of large clusters, and reduced the carbon diffusion length to result in complete carburization of Mo and W. The interconnected pores may also assist methane transport and diffusion during carburization, resulting in phase pure metal carbides at the synthetic conditions.

For both Mo_2C and W_2C, a heteropoly acid precursor solution to silica template ratio of 2 (by weight) was loaded for synthesis. This ratio is higher than the ratio typically used in the synthesis of mesoporous metal oxides (typically 1:1). By keeping the loading level

high, three-dimensionally ordered mesoporous particles rather than isolated nanoclusters are reproducibly synthesized. While it is possible to increase the precursor loading further, it could cause the formation of undesired large particles outside the pore channels of the silica template.

4.3.2. Morphology of mesoporous metal carbides

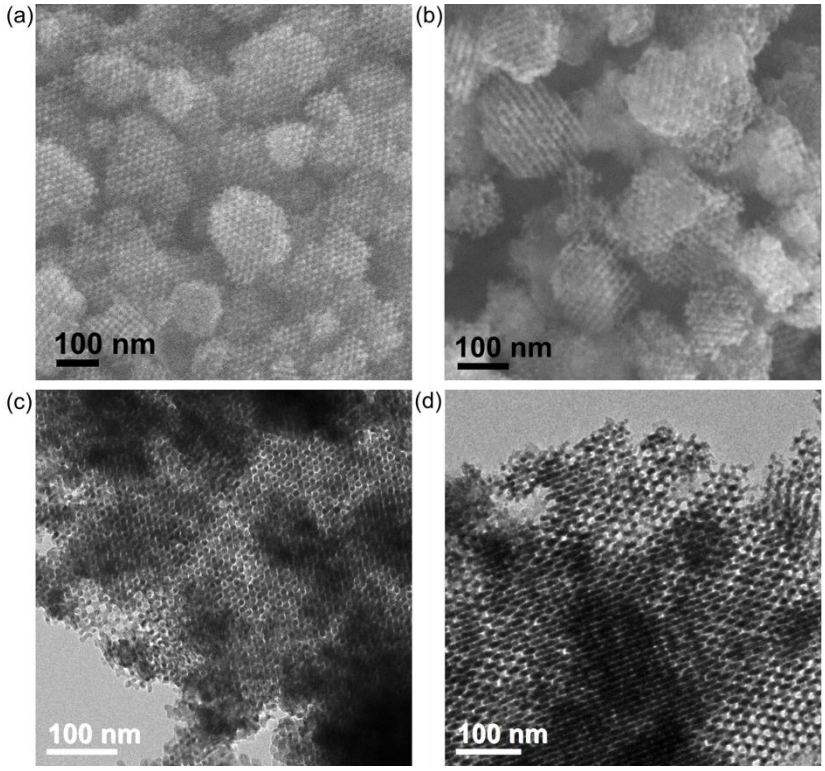

Figure 4.1 Typical SEM images for ordered mesoporous (a) Mo_2C and (b) W_2C. Typical TEM images for ordered mesoporous (c) Mo_2C and (d) W_2C.

The morphology of as-synthesized mesoporous Mo_2C and W_2C was examined using SEM (Figure 4.1a-b). Both samples contain fine particles with a similar size of 100-200 nm and the majority of particles have an ordered porous structure, confirming the high quality of as-made mesoporous metal carbides. Highly ordered mesoporous structures of as-synthesized Mo_2C and W_2C are also evident in TEM images (Figure 4.1c-d). An examination of more than 30 particles in both samples confirmed that the ordered porous

structures are present throughout the samples. The mesoporosity of as-synthesized samples was further examined using N_2 adsorption-desorption measurements. The shapes of adsorption-desorption isotherms (Figure 4.7 in Section 4.5) are similar to those of mesoporous metal oxides. The BET surface areas of Mo_2C and W_2C are 93 and 73 $m^2\ g^{-1}$, respectively. Considering the high bulk density of metal carbides (typically 9–16 g cm^{-3}), the obtained surface areas of mesoporous metal carbides are well aligned with the surface areas (~100 $m^2\ g^{-1}$) in previous reports for mesoporous metal oxides and sulfides synthesized using a similar nanocasting approach.[151,159–161] Pore size distributions calculated using the BJH method on the desorption portion of the isotherms are shown in the insets of Figure 4.7 (Section 4.5). Interestingly, the pore size of mesoporous Mo_2C exhibited a bimodal distribution, 3.8 nm and 13 nm. The bimodal distribution is likely due to the partial occupation of two independent sets of pore networks in the KIT-6 template as previously observed in the synthesis of mesoporous NiO.[162] The complete occupation of both sets of pores leads to 3.8 nm pores in the replica, while a partial filling results in 13 nm pores. A similar bimodal pore size distribution was observed for the mesoporous W_2C sample with one at 3.7 nm and the other at 13 nm, although the 13 nm peak is more pronounced compared to the 3.7 nm peak. We surmise that the difference may be due to: (i) the higher density of W_2C (~16 g cm^{-3}) compared to that of Mo_2C (~9 g cm^{-3}); (ii) the poor mobility of W compared to Mo during the crystal growth, which causes the local growth of W_2C inside one pore network rather than across both pore networks.

4.3.3. Atomic and surface structures of mesoporous metal carbides

The atomic structures of as-synthesized mesoporous Mo_2C and W_2C were characterized using wide-angle PXRD analysis. PXRD patterns for both mesoporous samples (Figure 4.2a) show clear diffraction peaks, which can be indexed to pure orthorhombic β-Mo_2C (space group: Pbcn) or W_2C (space group: Pbcn) phase, consistent with the patterns for bulk metal carbide standards. No impurity peaks were observed in the PXRD analysis. The diffraction peaks are also significantly broad, suggesting the nanocrystalline nature of walls of the mesopores. Using the Scherrer formula, the crystal

domain sizes of mesoporous Mo_2C and W_2C are roughly estimated to be 3 nm and 4 nm, respectively. A more accurate estimation of the grain size is quite difficult, since the three peaks between 20–40 degrees are convoluted. The atomic structures of nanocrystalline walls were also studied using high-resolution TEM (HRTEM) technique. The images (Figure 4.2b-c) show clear lattice fringes of the mesopore walls, confirming the high crystalline nature of the walls. The distances between two neighboring fringes are 0.23 and 0.26 nm for Mo_2C and W_2C samples, respectively.

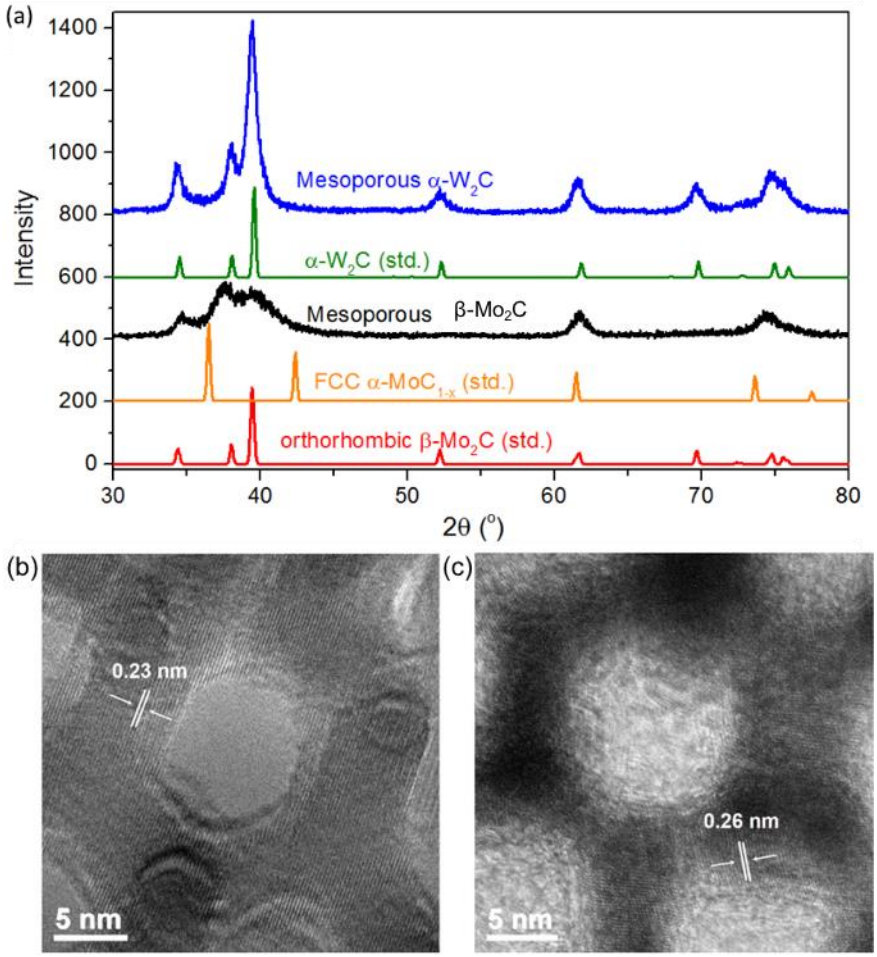

Figure 4.2 (a) PXRD patterns of mesoporous Mo_2C and W_2C including corresponding standards. Typical HRTEM images of (b) mesoporous Mo_2C and (c) mesoporous W_2C.

Both as-synthesized mesoporous metal carbides were further examined by XAS techniques. For the Mo_2C sample, the X-ray Absorption Near-edge Structure (XANES) results (Figure 4.3a) show that the Mo K-edge of mesoporous Mo_2C overlaps with the edges of bulk Mo_2C (Sigma Aldrich) and metallic Mo foil, indicating that the binding energy for the majority of Mo atoms in Mo_2C samples is similar to the binding energy for metallic Mo. This phenomenon can be explained by the ionic contribution being relatively weak in the Mo-C bond and has also been reported in the literature.[163–165] It should be noted that there are a number of literature reports of an energy shift in the Mo K-edge between Mo_2C and Mo foil.[166,167] This discrepancy may be due to different synthetic methods, particle sizes, and surface characteristics of the materials. In contrast, the W L_3-edge of mesoporous W_2C was shifted slightly towards high energies (~0.5 eV) compared to that of metallic W foil (Figure 4.3b), suggesting some of the W atoms in W_2C are slightly oxidized, although the majority of W atoms still have a binding energy close to metallic W. It is likely that a small amount of tungsten oxide is present on the surface of as-synthesized mesoporous W_2C sample.

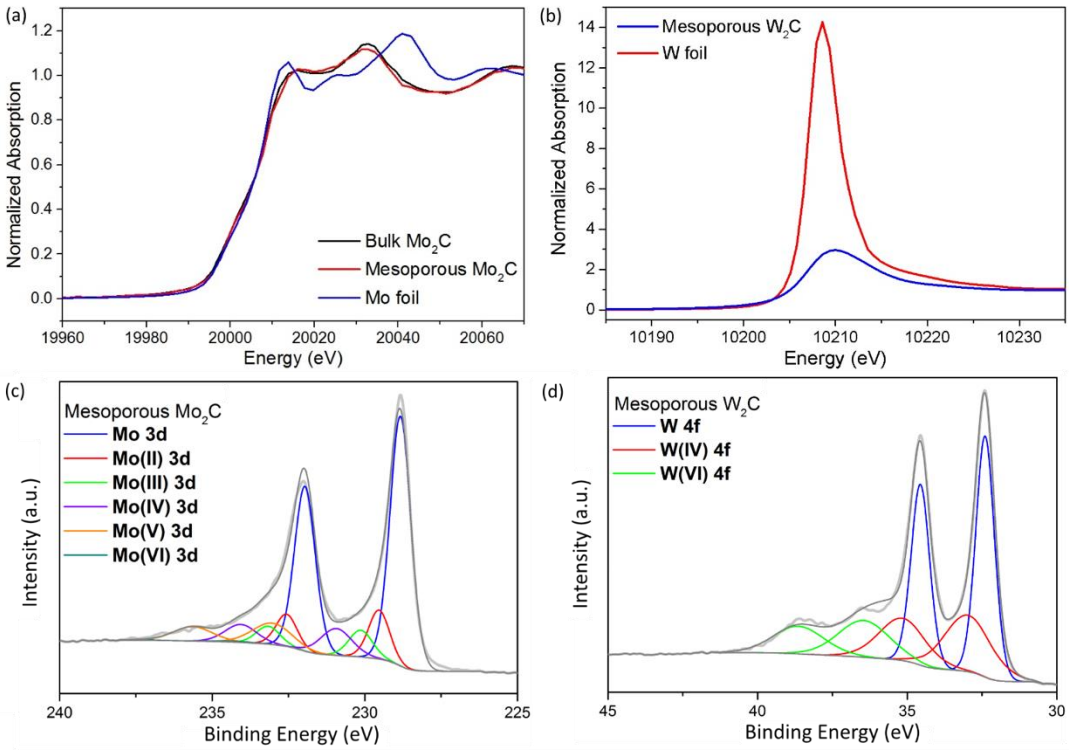

Figure 4.3 XANES results for ordered mesoporous (a) Mo_2C and (b) W_2C. Data for metallic foils and bulk Mo_2C are shown for comparison. XPS spectra of (c) Mo 3d region for Mo_2C and (d) W 4f region of W_2C with their fitting peaks.

Surface electronic structures of as-synthesized mesoporous Mo_2C and W_2C were analyzed by XPS. Mo 3d and W 4f core level spectra are shown in Figure 4.3c-d. Both spectra are split into two sets of peaks because of spin–orbital coupling. The peak fitting suggests that there are six oxidation states for Mo (Mo^0, Mo^{2+}, Mo^{3+}, Mo^{4+}, Mo^{5+} and Mo^{6+}) on the surface of Mo_2C and three oxidation states for W (W^0, W^{4+} and W^{6+}) on the surface of the W_2C. It is worth noting here that Mo in Mo_2C and W in W_2C are not distinguishable from metallic Mo^0 and W^0, respectively, due to their similarity in binding energyies. However, the majority of their surfaces is unlikely in the metallic form based on HRTEM characterizations. Therefore, the existence of dominant "zero valence peak" along with small peaks of higher oxidation states can be explained as the majority of the surface metal

atoms are in the form of metal-carbon bonds in these carbides. The small fraction of oxide contamination on the carbide surface is likely due to the surface passivation during dissolution and oxidation by air during sample handling, which may cause a deviation of C:Mo stoichiometric from 0.5.

4.3.4. Catalytic performance of mesoporous Mo_2C in anisole HDO

Vapor phase anisole HDO on mesoporous Mo_2C was conducted at 423 K. Benzene selectivity increased from ~53% to ~82% and cyclohexane selectivity decreased from ~47% to ~17% in the first ~1 ks on stream, and remained stable at ~80% and ~20%, respectively (Figure 4.4a). A similar trend of an increase in benzene rate at the expense of cyclohexane rate before steady state anisole HDO rates were obtained has been reported previously using transient kinetic studies and was ascribed to oxygen (~0.29 monolayer) accumulation on the Mo_2C catalyst.[54]

A comparison of anisole HDO catalytic performance on nanocrystalline Mo_2C and mesoporous Mo_2C is shown in Table 4.1 (structural information can be found in Table 4.4 in Section 4.5). The selectivity to the direct and completely deoxygenated products, benzene and cyclohexane, on mesoporous Mo_2C (>99%) is higher than that on the nanocrystalline Mo_2C (~97%) at 423 K and ~0.15 kPa anisole. The selectivity to cyclohexane on mesoporous Mo_2C (~20%), however, is almost three times more than that on the nanocrystalline Mo_2C (~7%). The difference in benzene and cyclohexane selectivity between the mesoporous Mo_2C and nanocrystalline Mo_2C may result from two possible reasons: (i) the presence of fcc α-Mo_2C(200) and fcc α-Mo_2C(220) phases in the nanocrystalline Mo_2C (dominant phase: orthorhombic β-Mo_2C), whereas the mesoporous Mo_2C is purely orthorhombic β-Mo_2C (Figure 4.2a), or (ii) the presence of different amounts of residual oxygen in mesoporous and nanocrystalline Mo_2C.

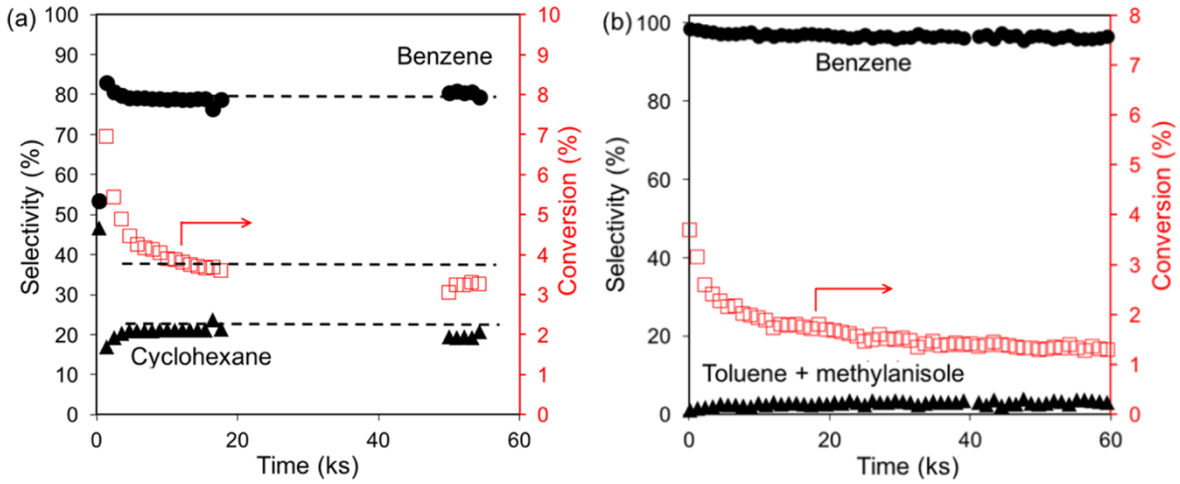

Figure 4.4 (a) Conversion and product selectivity for anisole HDO over mesoporous Mo_2C catalyst. Feed = anisole (0.16%)/ H_2 (balance) (mol%) at ~110 kPa total pressure and at 423 K; Total flow rate ~1.67 cm^3 s^{-1}. (b) Conversion and product selectivity for anisole HDO over mesoporous W_2C catalyst. Feed = anisole (0.06%)/ H_2 (balance) (mol%) at ~131 kPa total pressure and at 444 K; Total flow rate ~3.33 cm^3 s^{-1}.

Anisole conversion on mesoporous Mo_2C at 423 K decreased from ~7% to ~4% in the first ~18 ks on stream and remained at ~3.3% conversion for an additional ~36 ks (Figure 4.4a). Similar deactivation profiles with time-on-stream for HDO of phenolic compounds on Mo_2C catalysts have been reported previously in the literature.[53,128,168] The catalyst deactivation is likely due to the oxidation of surface/bulk Mo_2C by water (a byproduct of HDO) to form oxide phases with lower activity, and/or coke deposition blocking the active sites for HDO reactions.[53,127,128] To elucidate the origin of the catalyst deactivation, we examined the spent mesoporous Mo_2C catalyst. The results clearly show that the crystal structure of orthorhombic β-Mo_2C is preserved (Figure 4.8a in Section 4.5), while carbon deposition is evident in the SEM image (Figure 4.9a, Section 4.5), indicating that coking may cause the decrease in conversion over time. Additionally, the ratio of C_1/C_6 for anisole HDO on mesoporous Mo_2C was ~0.1 at the beginning of reaction (<1 ks on-stream) and remained at ~0.7 after 1 ks, suggesting that mesoporous Mo_2C surface is carbon-deficient as C_1 carbon deposition occurred during the initial transient (~0.01 monolayer) and

continued after steady state anisole HDO rates were observed (~0.1 monolayer of cumulative C_1 deposition during the 54 ks on stream). Carbon-deficient surfaces of Mo_2C have been reported in the literature via temperature-programmed reaction measurements or elemental analysis.[1,7,8,35,54,169] Balbuena and coworkers have also demonstrated surface depletion of carbon in the synthesis of carbon nanotubes on cobalt surfaces, suggesting that heterogeneity in carbon content in bulk and surface structure composition may be common for transition metal catalysts.[170,171] The formation of carbon-deficient surfaces on orthorhombic β-Mo_2C may result from (i) a relatively lower carburization temperature in catalyst synthesis (e.g. <1023 K using 10%CH_4/H_2 for molybdic acid powder),[7,169] and/or (ii) the reductive treatment in H_2 for Mo_2C at elevated temperatures prior to reaction studies.[1,8]

Table 4.1 Comparison of benzene synthesis rates, benzene TOFs, product selectivities, H_2 orders, apparent activation energies, and site densities for anisole HDO on nanocrystalline Mo_2C, mesoporous Mo_2C, and mesoporous W_2C.

	Benzene rate[a]	H_2 order	E_{app}[b]	Benzene TOF[c]	Site per surface metal	Product selectivity
Nanocrystalline Mo_2C	~40-80 (423 K)	~0.5	~70	~10 (423 K)	~2.5%	Benzene ~90% ; Cyclohexane 7%; Others[d] <2.5%
Mesoporous Mo_2C	~6-10 (423 K)	~0.5	~75	~9 (423 K)	~0.6%	Benzene ~80% ; Cyclohexane ~20%; Others[e] <1%
Mesoporous W_2C	~1.6-2.6 (443 K)	~0.5	~73	~5 (443 K) ~2 (extrapolated to 423 K)	~0.6%	Benzene >96%; Others[e] <4%; Heavier compounds <1%

[a] $\times 10^{-9}$ mol g_{cat}^{-1} s^{-1}; [b] kJ mol^{-1}; [c] $\times 10^{-4}$ mol mol_{CO}^{-1} s^{-1}; [d] others contain toluene, phenol, and styrene; [e] others contain toluene and methylanisole.

It should be noted that the catalytic activity of mesoporous Mo_2C could be regenerated by treating the spent catalyst in pure H_2 at 723 K for 1 h (Figure 4.10a in Section 3.5). Notably, a ~30% increase in benzene synthesis rates over the regenerated mesoporous Mo_2C catalyst was observed compared to the rate of the fresh catalyst. It is likely that the H_2 treatment at 723 K allows the carbon-deficient catalyst surface to be re-carburized by the carbonaceous species deposited during anisole HDO at 423 K, consistent with the observed increase (~50%) in 2-methylfuran synthesis rates from furfural HDO on the regenerated nanocrystalline Mo_2C at 423 K.[128] Carburization of carbon-deficient Mo or Mo_2C surfaces by carbon-containing reactants, such as n-butane, CO, and ethane, in H_2 under reaction conditions (atmospheric pressure and >510 K) has also been reported in the literature.[1,172,173]

4.3.5. Catalytic performance of mesoporous W_2C in anisole HDO

Catalytic anisole HDO studies were also performed on mesoporous W_2C after an H_2 pretreatment at 723 K. Benzene selectivity in excess of 96% with negligible cyclohexane selectivity for anisole HDO was observed over mesoporous W_2C at 443 K and atmospheric hydrogen pressure (Figure 4.4b), clearly distinguishing mesoporous W_2C from other HDO catalysts such as MoO_3 (~56% benzene selectivity, 100kPa of H_2, 593 K),[25] bimetallic FeMo phosphide catalysts (~90% benzene selectivity, 2.1 MPa of H_2, 673 K),[122] and Mo_2C catalysts (~90% benzene selectivity, 100 kPa of H_2, 423 K).[127] It represents the most selective anisole HDO catalyst for benzene synthesis under ambient hydrogen pressures and low reaction temperatures reported to date. It has been reported that tungsten carbide catalysts are able to catalyze double bond hydrogenation reactions such as ethylene and benzene hydrogenation.[174,175] The observed near zero cyclohexane selectivity from anisole HDO on mesoporous W_2C (Figure 4.4b) compared to ~20% cyclohexane selectivity on mesoporous Mo_2C (~80% benzene selectivity, Figure 4.4a) suggests that W_2C demonstrates preferential selectivity to unsaturated HDO products over saturated ones, which is consistent with previous studies on Mo_2C and W_2C based catalysts.[22,24,176,177] The negligible cyclohexane selectivity on mesoporous W_2C is presumably ascribed to the

stronger oxygen affinity of tungsten, as also suggested by the stronger W–O bond (644 ± 42 kJ mol^{-1}) compared to Mo–O bond (485 ± 63 kJ mol^{-1}) reported at 0 K by DeMaria et al.[178] Anisole conversion decreased initially (~25 ks) and remained stable for at least 60 ks on stream. The near invariance in the product selectivity with the decrease in anisole conversion (Figure 4.4b) or benzene synthesis rate (Figure 4.10b in Section 4.5) after ~5 ks on stream indicates that no preferential loss/generation of sites occurred during catalyst deactivation, similar to that observed from anisole HDO on mesoporous Mo_2C (Figure 4.4a and Figure 4.10a in Section 4.5). The post-reaction structural analysis showed preservation of the crystalline structure and potential coke formation on the catalyst particles (Figures 4.8 and 4.9 in Section 4.5). The spent mesoporous W_2C catalyst can be reactivated by treatment in flowing H_2 at 723 K for 6 h as shown in Figure 4.10b (Section 4.5).

4.3.6. Kinetics and in situ CO titration studies

To explore reaction kinetics for anisole HDO, we studied both anisole, varied from 0.08–1.2 kPa (balance H_2), and hydrogen, varied from 6–107 kPa (balance He), pressure dependences on mesoporous metal carbides. Benzene synthesis rates on both mesoporous Mo_2C and W_2C are zero order dependent on anisole pressure and near half order dependent on H_2 pressure (Figure 4.11 in Section 4.5), suggesting that two distinct sites are required for benzene synthesis on both mesoporous Mo_2C and W_2C catalysts, which is consistent with the previously reported reaction mechanism for anisole HDO on the nanocrystalline Mo_2C.[127] The measured apparent activation energies (Figure 4.12 in Section 4.5), ~75 kJ mol^{-1} for the mesoporous Mo_2C (411–441 K) and 73 ± 7 kJ mol^{-1} for the mesoporous W_2C (432–462 K), are also consistent with that measured from anisole HDO on the nanocrystalline Mo_2C (76 ± 1.3 kJ mol^{-1}).[127] Therefore, benzene synthesis from anisole HDO on both Mo_2C and W_2C catalysts likely involves the same chemistry.

To assess benzene turnover frequencies (TOFs) on mesoporous metal carbides, we measured the numbers of active sites during vapor phase anisole HDO using in situ CO titration techniques. A co-feed of 1% CO/He was introduced when steady state benzene

synthesis rates were reached (the shaded areas in Figures 4.5 representing CO co-feeds). The results clearly suggest that CO is a reversible titrant for benzene synthesis from anisole HDO on both mesoporous Mo_2C and W_2C catalysts as benzene rates can be completely recovered after CO co-feed (0.06–0.08 kPa and 0.03–0.05 kPa for the mesoporous Mo_2C and W_2C, respectively) was removed, similar to anisole HDO on nanocrystalline Mo_2C.[54] Based on in situ CO titration results, the estimated benzene TOF for anisole HDO on mesoporous Mo_2C is ~ $(9.3 \pm 0.8) \times 10^{-4}$ mol mol_{CO}^{-1} s^{-1} at 423 K, which is similar to that for nanocrystalline Mo_2C (~10×10^{-4} mol mol_{CO}^{-1} s^{-1} at 423 K).[54] The same benzene TOF on both Mo_2C formulations suggests that the nature of the metal-like sites for anisole HDO is the same for the two Mo_2C samples. The differences in benzene and cyclohexane selectivity between the nanocrystalline and mesoporous Mo_2C catalysts discussed above, therefore, are not resulted from the site requirements for benzene formation on the materials.

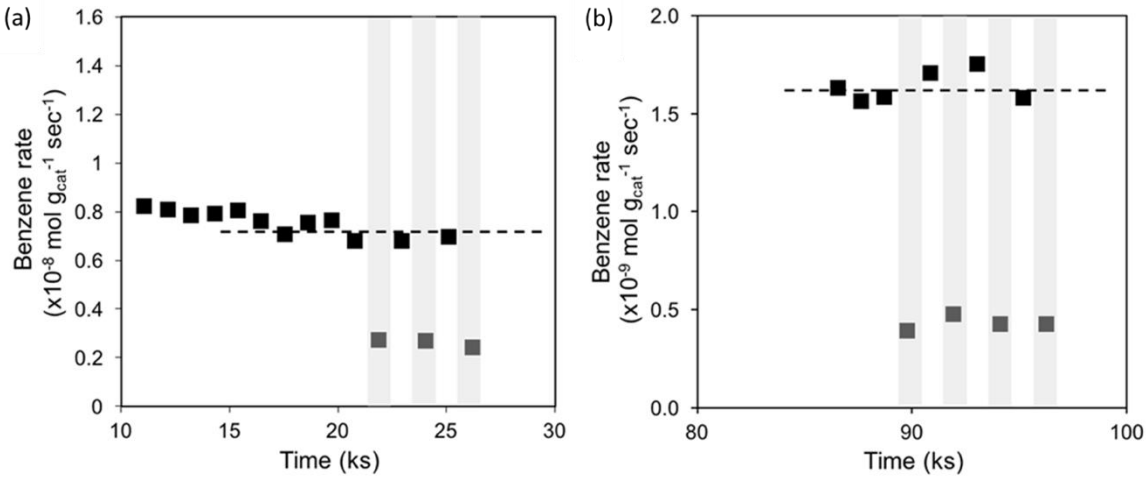

Figure 4.5 Benzene synthesis rates vs. time-on-stream for anisole HDO over (a) mesoporous Mo_2C at 0.16 kPa anisole, total flow rate ~1.67 cm^3 s^{-1}, and at 423 K; CO partial pressure 0.06–0.08 kPa, and (b) mesoporous W_2C at 0.09 kPa anisole, total flow rate ~3.33 cm^3 s^{-1}, and at 443 K; CO partial pressure 0.03–0.05 kPa.

Benzene TOF for anisole HDO measured on mesoporous W_2C is ~ $(5.4 \pm 0.5) \times 10^{-4}$ mol mol_{CO}^{-1} s^{-1} at 443 K, and, if extrapolated using the measured apparent activation energy (73 kJ mol^{-1}), benzene TOF is ~2×10^{-4} mol mol_{CO}^{-1} s^{-1} at 423 K, demonstrating that TOF

for benzene synthesis on mesoporous W_2C is only ~20% of that on Mo_2C catalysts at 423 K. These results highlight that the difference in the metal-like sites involved in anisole HDO for benzene formation on group VI metal carbides is not the identity but the nature of the site. The observed invariance of benzene TOF with a concurrent decrease in benzene synthesis rate (Figure 4.11b and Figure 4.13 in Section 4.5) as a function of anisole pressure (0.2–1.2 kPa) suggests that the number of active sites for benzene synthesis from anisole HDO on the W_2C decreased with increasing oxygenate pressure while the identity and the nature of the active sites remained the same.

The site densities for benzene formation on mesoporous Mo_2C and W_2C, and nanocrystalline Mo_2C, obtained by dividing the amount of all operating sites for benzene synthesis by the number of metal sites on the catalyst surface, are summarized in Table 4.1. The number of active sites per surface metal atom for benzene synthesis at 443 K on mesoporous W_2C (~0.6%, based on ~73 $m^2\ g^{-1}$ and the estimated W atom density of ~4 x 10^{14} cm^{-2} (Table 4.5 in Section 4.5)) is similar to that on mesoporous Mo_2C at 423 K (~0.6%, based on ~93 $m^2\ g^{-1}$ and Mo atom density of ~7 x 10^{14} cm^{-2} (Table 4.5 in Section 4.5)). However, the site density on the nanocrystalline Mo_2C at 423 K (~2.5%, based on ~100 $m^2\ g^{-1}$ and Mo atom density of ~7 × 10^{14} cm^{-2}) is about three times larger than that on mesoporous carbides.

4.4. Conclusions

We report the synthesis of high-surface area (> 70 $m^2\ g^{-1}$) ordered mesoporous Mo_2C and W_2C using a novel approach involving the use of a hard silica template and concurrent carburization of the metal-precursor heteropoly acid using flowing CH_4 at 923 K. Electron microscopy measurements evidence the existence of an ordered mesoporous structure and X-ray based spectroscopies evidence the predominant existence of the carbide phase in these materials. These materials exhibit unprecedented selectivity for hydrodeoxygenation of anisole to benzene (~96% for W_2C) at low temperatures (423-443 K) and ambient pressures of hydrogen. The existence of sites with metal-like characteristics and ~5 μmol

active catalytic centers per gram on Mo_2C and W_2C was demonstrated using in situ chemical titration methods.

4.5. Supporting information

4.5.1. XAS data collecting profile

Background start energy: 200 eV before the edge

Pre-edge start energy: 30 eV before the edge

Data collect range: starting at K = 3 Inverse Angstroms and ending at K = 13 Inverse Angstroms

Background scan energy increment: 10 eV

Pre-edge scan energy increment: 0.7 eV

EXAFS scan K increment: 0.05 Inverse Angstroms

Base count time: 1 second

Final K count time: 5 seconds

K weight for time base: 1.5

Background count time: 5 seconds

Table 4.2 Temperature program for GC oven.

Temperature set point (°C)	Heating rate (°C min^{-1})	Hold time (min)	Total run time (min)
40		1	1
80	20	0	3
125	10	1	8.5
135	10	1	10
250	30	1	15

4.5.2. Methods for calculations of carbon balance, anisole conversion, C_6^+ product selectivity, and C_1/C_6 ratio

Carbon balance, anisole conversion, C_6^+ product selectivity, and C_1/C_6 ratio were calculated as follows:

$$Carbon\ balance = \frac{sum\ of\ moles\ of\ C\ in\ all\ compounds\ in\ the\ effluent}{(moles\ of\ C\ in\ anisole)_{in}} \times 100\% \quad (4.1)$$

$$Anisole\ conversion = \frac{(sum\ of\ moles\ of\ C\ in\ products)_{out}}{(moles\ of\ C\ in\ anisole)_{in}} \times 100\% \quad (4.2)$$

$$C_6^+\ product\ selectivity = \frac{moles\ of\ C_{6+}\ product\ i}{moles\ of\ C_{6+}\ products} \times 100\% \quad (4.3)$$

$$\frac{C_1}{C_6} ratio = \frac{(sum\ of\ moles\ of\ methane\ and\ methanol)}{(sum\ of\ moles\ of\ benzene\ and\ cyclohexane)} \quad (4.4)$$

Carbon balance, defined in Equation 4.1, was typically ±10%, however, the typical feed fluctuation was also ~±10%. All kinetic measurements were conducted at differential conversion (<7%). The absence of external mass transfer was confirmed by Mears' Criteria; internal mass transfer can be neglected as the estimated Thiele modulus was <<1.

4.5.3. Internal and external mass transfer limitations

The Thiele modulus (ϕ) was used to check internal mass transfer limitations in anisole HDO kinetic studies, which was estimated using Equation 4.5[107]:

$$\Phi = \frac{-r_{A(obs)} \times \rho_c \times R^2}{D_e \times C_{As}} = \eta \phi^2, \quad (4.5)$$

where $-r_{A(obs)}$ is the observed reaction rate in kmol kg_{cat}^{-1} s^{-1}; ρ_c is the pellet bulk density of the catalyst in kg m^{-3}; R is the catalyst pellet radius in m (taking the crystallite size as effective diffusion length for the mesoporous carbides, ~4×10^{-9} m); D_e is the effective diffusivity at reaction temperature in m^2 s^{-1}; C_{As} is the gas concentration of reactant A at the catalyst surface in kmol m^{-3} (taking anisole as reactant A to give an upper bound of the Thiele modulus); η is the internal effectiveness factor and ϕ is the Thiele modulus. If $\phi \ll 1$, η is close to unity and ϕ can be calculated.

Effective gas phase diffusivity, D_e, is estimated using Equation 4.6[179]:

$$D_e = \frac{D_{AB} \times \varepsilon \times \delta}{\tau}, \quad (4.6)$$

where ε is the pellet void fraction (0.3), D_{AB} is binary diffusivity in cm^2 s^{-1}, τ is tortuosity (6), and δ is constriction factor (0.8).

Binary diffusivity, D_{AB}, was taken from Bird et al.[109]:

$$\frac{pD_{AB}}{(p_{cA}p_{cB})^{1/3}(T_{cA}T_{cB})^{5/12}(\frac{1}{M_A}+\frac{1}{M_B})^{1/2}} = a(\frac{T}{\sqrt{T_{cA}T_{cB}}})^b, \quad (4.7)$$

where D_{AB} is in cm^2 s^{-1}, pressure p is in atm, temperature T is in K, a = 3.64×10^{-4} and b = 2.334. Molecular weight of A and B is M_A and M_B. Subscript c represents the corresponding critical properties. A is gas phase anisole and B is hydrogen.

External mass transfer limitations during kinetic studies can be neglected if the Mears' criterion (Equation 4.8) is satisfied[107]:

$$\frac{-r_{A(obs)} \times \rho_b \times R \times n}{k_c \times C_{Ab}} < 0.15, \quad (4.8)$$

where $-r_{A(obs)}$ is the observed reaction rate in kmol kg_{cat}^{-1} s^{-1}; ρ_b is catalyst bed density in kg m^{-3}; R is the catalyst pellet radius in m (the median value of the size of the catalyst pellets, ~3×10^{-4}); n is the reaction order of reactant A (0.5 for H_2 and zero for anisole as the primary reactant); C_{Ab} is the concentration of reactant A in the bulk gas phase at reaction temperature in kmol m^{-3}; k_c is the mass transfer coefficient for reactant A in m s^{-1}, which can be estimated by the Sherwood number with the Frossling correlation.[107]

The parameters used for the estimation of the Thiele modulus and Mears' criterion as well as the estimated values are listed in Table 4.3. The absence of mass transfer limitations was confirmed.

Table 4.3 Parameters used and estimated for assessing internal and external mass transfer limitations for anisole HDO on mesoporous Mo_2C and W_2C at 423 and 443 K, respectively

	Mesoporous Mo_2C	Mesoporous W_2C
ρ_c (kg m^{-3})	361[a]	1975[b]
D_e (m^2 s^{-1})	6.5×10^{-6}	7.2×10^{-6}
ϕ Thiele modulus	~4×10^{-7}	~1×10^{-6}
	External Mass transfer	
ρ_b (kg m^{-3})	253[b]	1382[c]
k_c (m s^{-1})	0.5	0.6
Mears' criterion	2.3×10^{-8}	1.2×10^{-7}

[a] Measured from the as-synthesized mesoporous Mo_2C

[b] Obtained from $\rho_b = (1-\varepsilon)\rho_c$

[c] Measured from the pelletized and sieved mesoporous W_2C

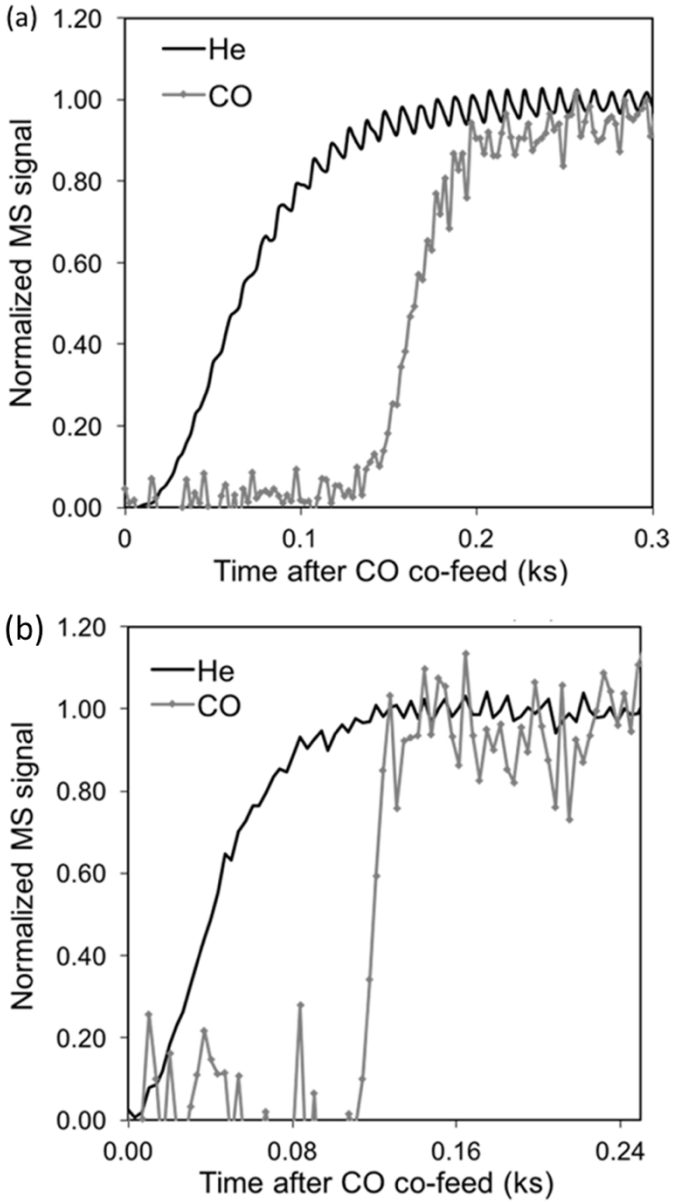

Figure 4.6 Typical transient mass spectrometric signals of helium and CO normalized to the signals at steady state as a function of time after co-feed for CO titrations for anisole HDO on (a) mesoporous Mo_2C and (b) mesoporous W_2C.

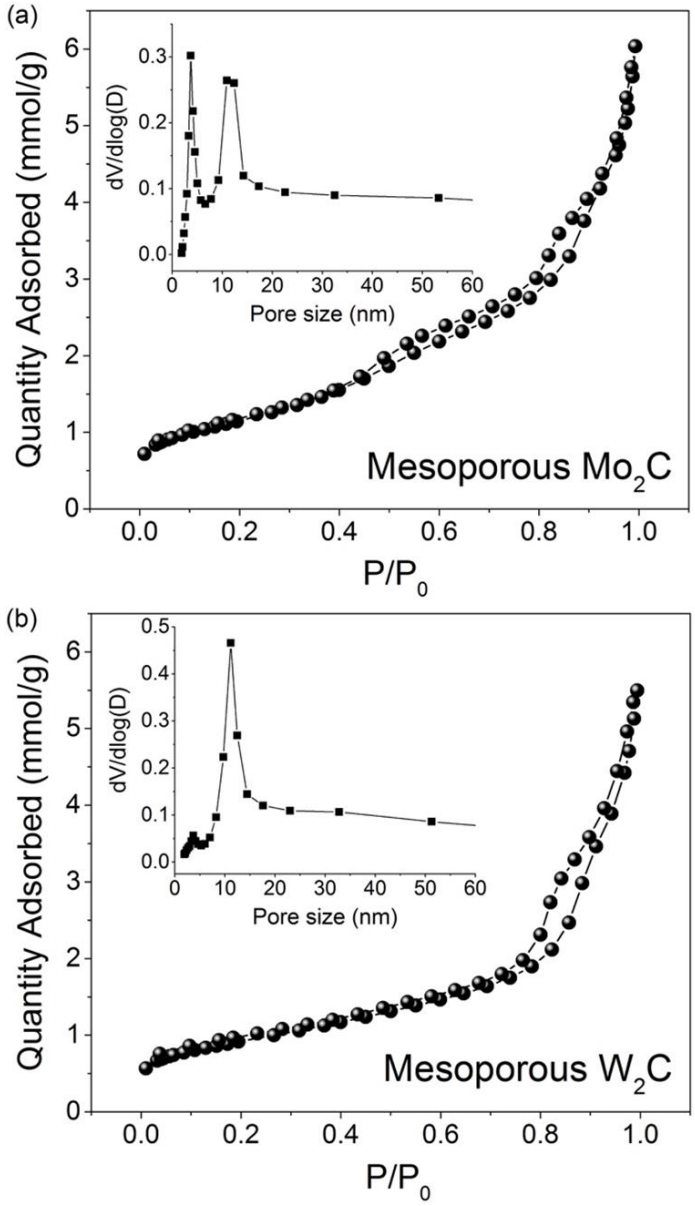

Figure 4.7 The N_2 adsorption/desorption isotherms for (a) mesoporous Mo_2C and (b) mesoporous W_2C. Insets: Their corresponding pore size distributions derived from the desorption isotherms using BJH method.

Table 4.4 Structural comparison of nanocrystalline Mo_2C[a] and mesoporous Mo_2C.

Catalyst	Surface area (Passivated) (m^2 g_{cat}^{-1})	Major carbidic phase	Morphology
Nanocrystalline Mo_2C	~100	orthorhombic β-Mo_2C	Nanoparticle morphology is evidenced in TEM image
Mesoporous Mo_2C	~93	orthorhombic β-Mo_2C	Ordered mesoporous structure evidenced by SEM and TEM images

[a] The characterization results for the nanocrystalline Mo_2C are reproduced from a prior report by Lee et al.[127]

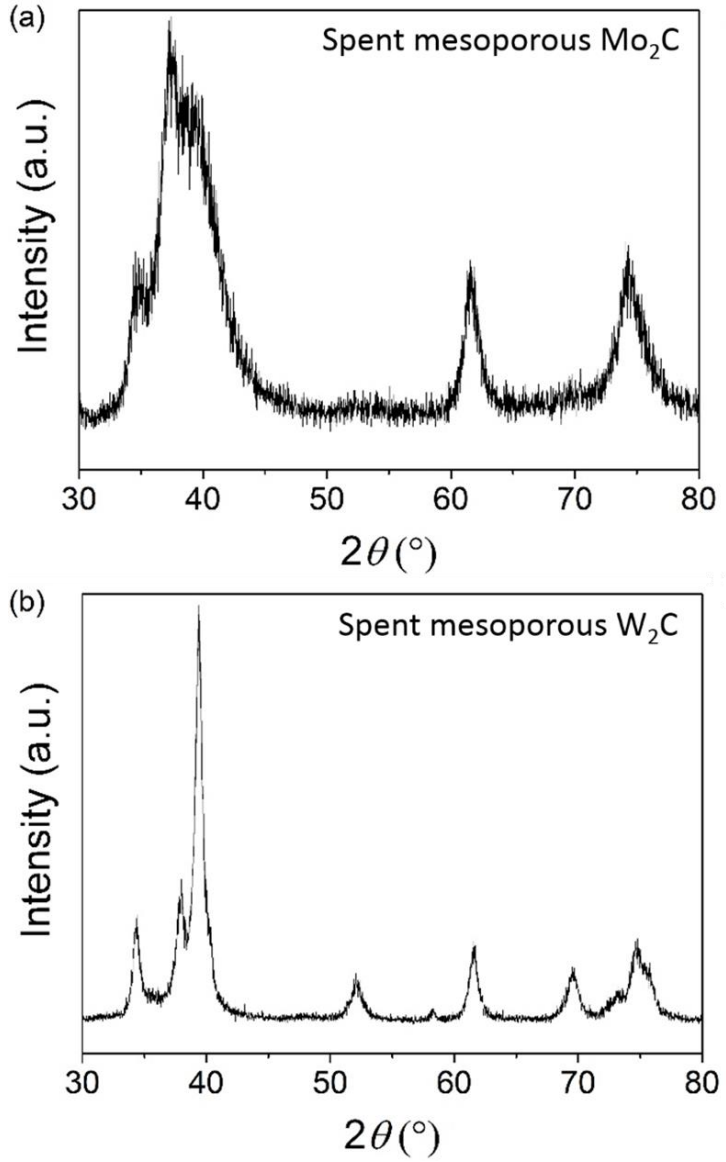

Figure 4.8 Powder XRD patterns of spent mesoporous (a) Mo_2C and (b) W_2C.

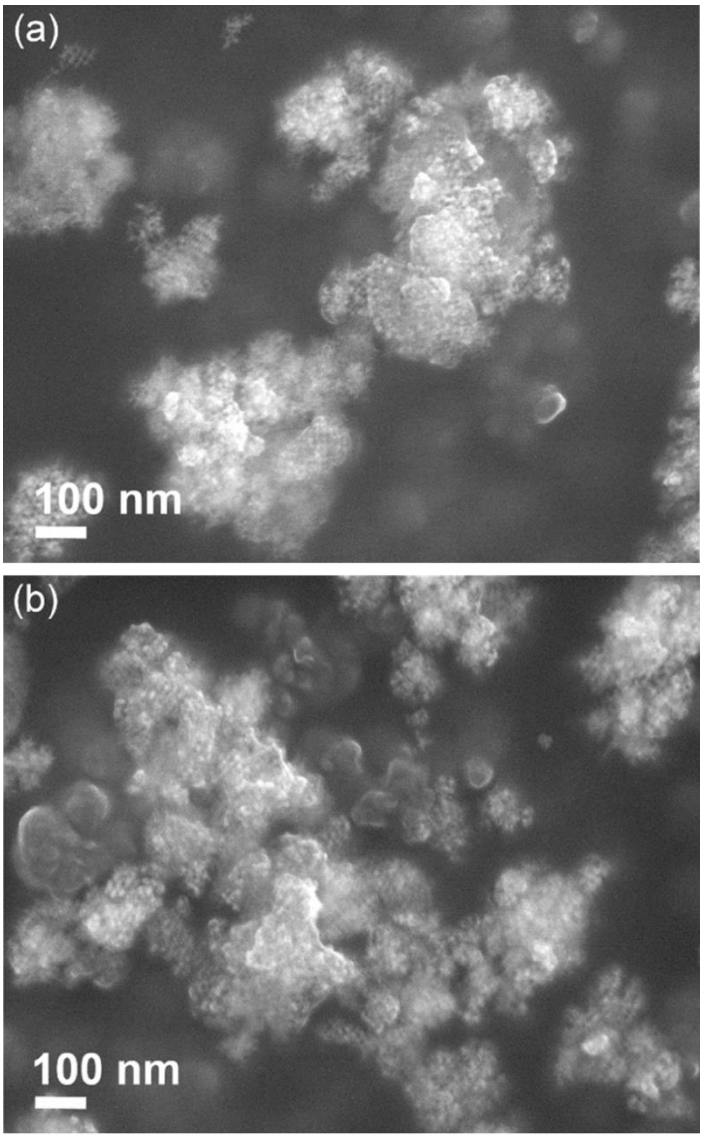

Figure 4.9 SEM image of (a) spent mesoporous Mo_2C and (b) spent mesoporous W_2C.

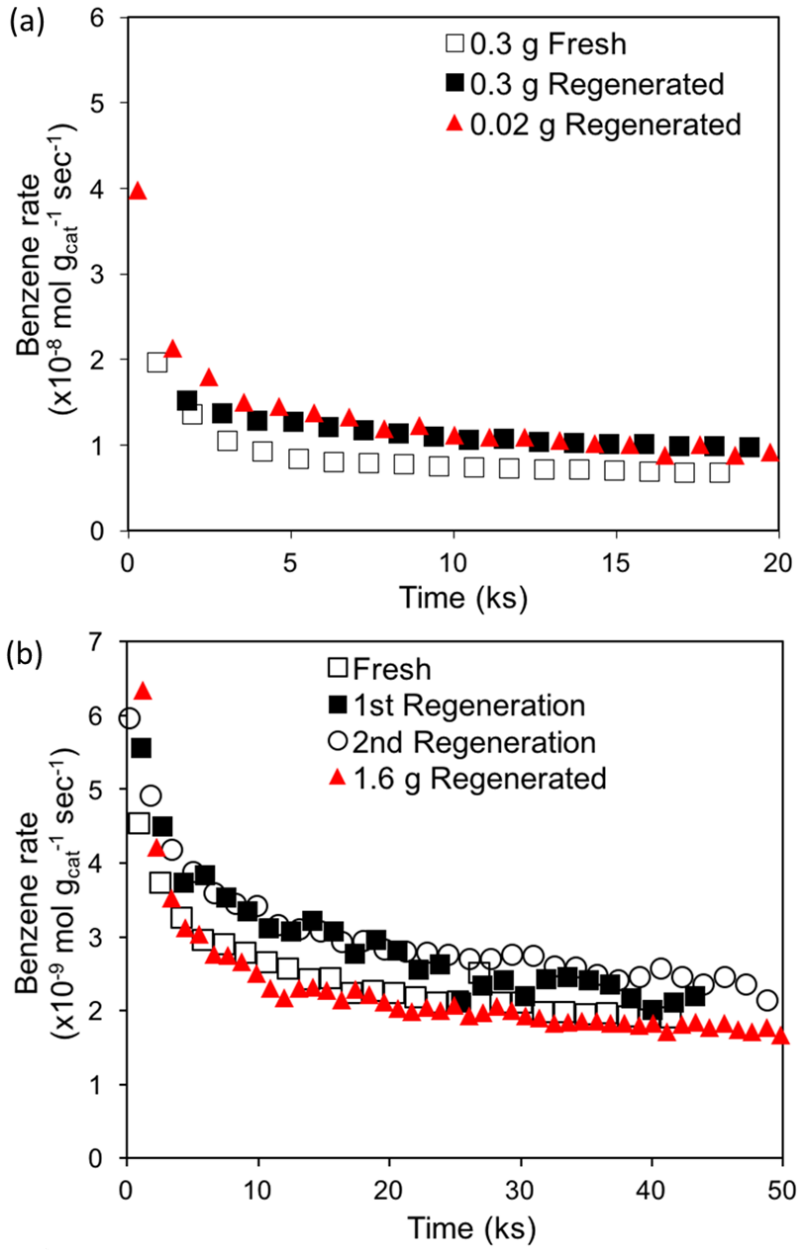

Figure 4.10 (a) Benzene synthesis rates for anisole HDO over as-synthesized mesoporous Mo_2C catalyst. Feed = anisole (0.16%)/ H_2 (balance) (mol%) at ~110 kPa total pressure and at 423 K; Total flow rate ~1.67 cm^3 s^{-1}. (b) Benzene synthesis rates for anisole HDO over as-synthesized mesoporous W_2C catalyst. Feed = anisole (0.06%)/ H_2 (balance) (mol%) at ~131 kPa total pressure and at 444 K; Total flow rate ~3.33 cm^3 s^{-1}.

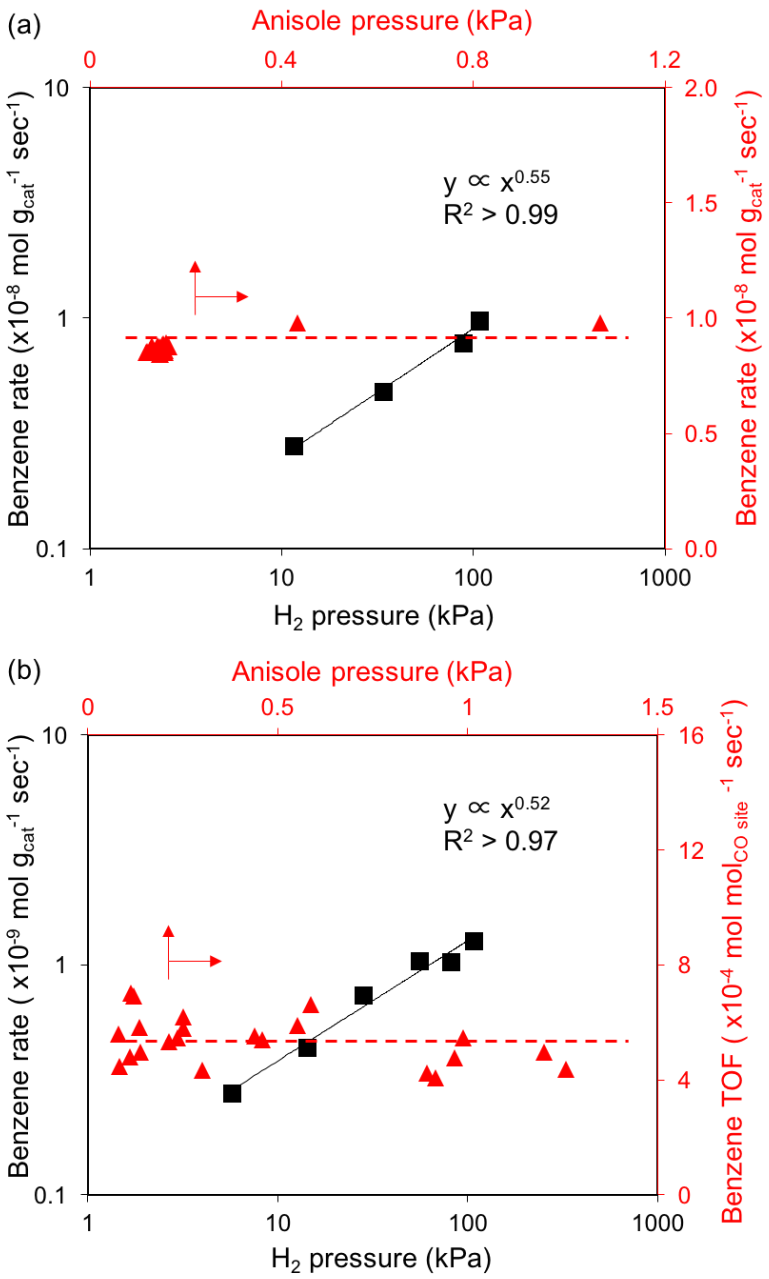

Figure 4.11 Effect of H_2 pressure (■) and anisole pressure (▲) for benzene synthesis rates on (a) mesoporous Mo_2C catalyst at 423 K, and (b) mesoporous W_2C catalyst at 443 K. H_2 pressure varied from 6–107 kPa (balance He) at 0.16 kPa and 0.08 kPa anisole pressures for anisole HDO on the mesoporous Mo_2C and W_2C catalysts, respectively. Anisole pressure varied from 0.08–1.2 kPa (balance H_2).

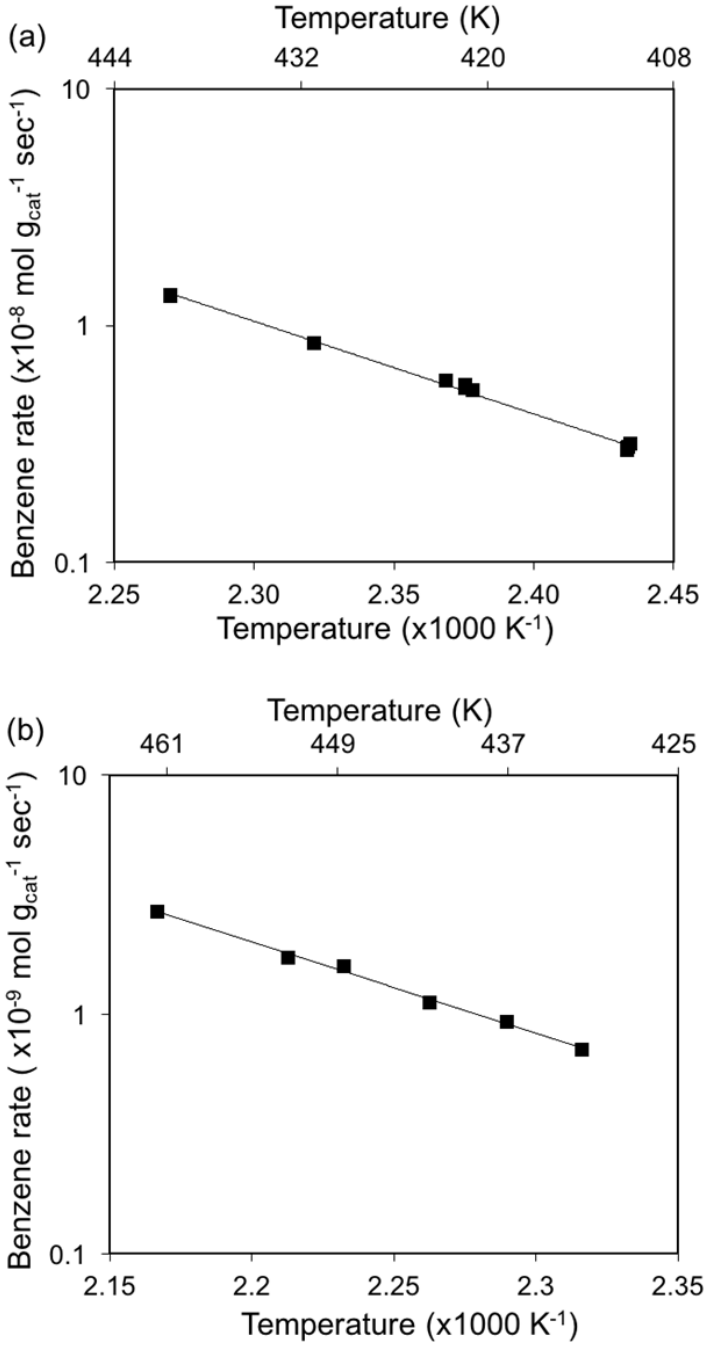

Figure 4.12 Temperature dependencies for benzene synthesis rates on (a) mesoporous Mo_2C catalyst at 411–441 K at ~0.16 kPa anisole pressure (balance H_2), total pressure ~110 kPa, and total flow rate ~1.67 $cm^3\ s^{-1}$, and (b) mesoporous W_2C catalyst at 432–462 K at ~0.08 kPa anisole pressure (balance H_2), total pressure ~107 kPa, and total flow rate ~3.33 $cm^3\ s^{-1}$.

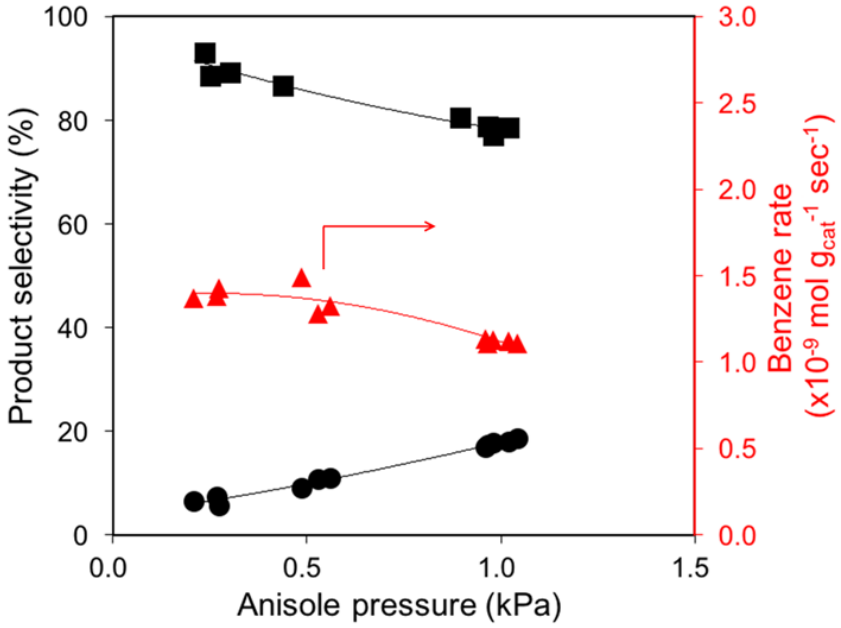

Figure 4.13 Product selectivity and benzene synthesis rate on mesoporous W_2C catalyst at 443 K. Anisole pressure varied from 0.2–1.2 kPa (balance H_2); Total flow rate ~3.33 cm^3 sec^{-1}. Benzene selectivity (■), benzene rate (▲), and selectivity to acid-catalyzed products toluene, phenol, and methylanisole (●).

4.5.4. Estimation of Mo and W atom surface densities

Molybdenum and tungsten atom surface densities in Mo_2C and W_2C were estimated using the averaged value of planar density of (100), (101), and (110) planes in the hexagonal close packed structure. The lattice constants are: hexagonal-Mo_2C ($a = b = 3.01$ Å$; c = 4.73$ Å , JCPDS No. 00-035-0787) and hexagonal-W_2C ($a = b = 5.18$ Å$; c = 4.72$ Å, JCPDS No. 03-065-3896). The sample calculations are shown in Table 4.5.

Table 4.5 Sample calculations of Mo and W atom surface densities in Mo_2C and W_2C.

Plane		Number of atom per plane	Planar density ($\times 10^{14}$ cm^{-2})	
			Mo_2C	W_2C
(100)	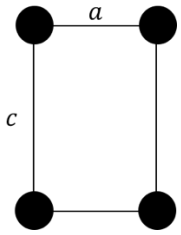	1	7.0	4.1
(101)	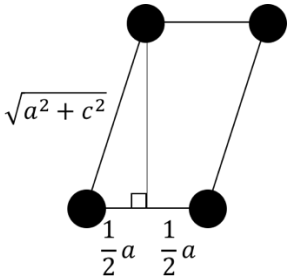	1	6.2	3.0
(110)	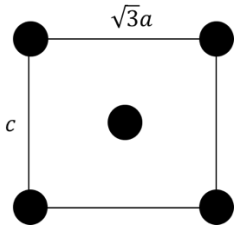	2	8.1	4.7

4.6. Acknowledgements

The authors at the University of Delaware acknowledge financial support from the University of Delaware Energy Institute Innovative Energy Research Grants Program (IERGP). The authors at the University of Minnesota acknowledge financial support from Office of Basic Energy Sciences of the U.S. Department of Energy under award number DE-SC0008418 (DOE Early Career Program).

5. Mo_2C modification by CO_2, H_2O, and O_2 for vapor phase hydrodeoxygenation

5.1. Introduction

Transition metal carbides have been shown to catalyze hydrodeoxygenation (HDO) reactions to convert biomass-derived compounds to fuels and chemicals.[16,17,20,23,25,26,180,181] These catalysts are selective in cleaving C–O and C=O bonds at ambient H_2 pressure and low temperatures (423–623 K),[16,19,25,55,180] and the aromaticity of furan and benzene rings can be retained during HDO.[55,128] Molybdenum carbides exhibit various stable surfaces that vary with reaction environments, such as surface coverage of O and C, and temperature,[34] and display heterogeneous surface structures, including distinct binding sites[28,29,32,33] and non-stoichiometric surface compositions.[8,35] The presence of oxygenates during HDO of bio-oil or pyrolysis vapor on the oxophilic transition metal carbides[2,27,41,45] can result in oxygen deposition on the catalyst, which can poison the metal-like sites for HDO[54] and/or possibly generate Brønsted acid sites.[56]

Oxygen (~ 4.7×10^{-4} mol g_{cat}^{-1}) and carbon (equivalent of ~ 1.4×10^{-3} mol g_{cat}^{-1} C_6 species) deposition was observed during the initial transient of anisole HDO on bulk β-Mo_2C that had been passivated in 1% O_2/He and pretreated in H_2 for 1 h at 723 K prior to the reaction at 423 K.[54] Cyclohexane signal was observed from mass spectrometry initially but as oxygen deposition occurred, cyclohexane dropped to almost zero and benzene signal was observed, suggesting that hydrogenation of benzene to cyclohexane was inhibited during the course of oxygen deposition.[54] This observation mirrors our previous studies that showed hydrogenation rates of benzene and toluene on Mo_2C being irreversibly inhibited when water or methanol was co-fed to the reactant line.[55] These results demonstrate that oxygen deposition under reaction environments alters catalyst composition and function, however, the effect of the source of oxygen on HDO catalysis is unclear.

Metal-like sites were found to be involved in selective benzene synthesis (>90% C_6^+ selectivity) from vapor phase hydrodeoxygenation of anisole on Mo_2C and W_2C catalysts as co-feeds of carbon monoxide were noted to inhibit HDO rates under reaction conditions and turnover frequencies of benzene synthesis at 423 K (~ 10^{-3} mol mol_{CO}^{-1} s^{-1} for Mo_2C and ~ 10^{-4} mol mol_{CO}^{-1} s^{-1} for W_2C) were noted to be invariant with different CO co-feed pressures.[54,182] Turnover frequency of benzene synthesis on a fresh Mo_2C from anisole HDO (~ 1.7×10^{-3} mol mol_{CO}^{-1} s^{-1}) was found to be almost the same as that on an O_2-modified Mo_2C catalysts (~ 1.5×10^{-3} mol mol_{CO}^{-1} s^{-1}; 0.075 O/Mo_{bulk} (molar ratio)), while benzene synthesis rate normalized per gram catalyst was three times higher on the fresh Mo_2C, indicating that the number of sites responsible for anisole HDO on Mo_2C decreases with O_2 treatment.[54]

Oxygen modified tungsten carbide materials prepared by exposing freshly synthesized tungsten carbides to O_2 at various temperatures have been reported to exhibit bifunctionality.[10,11,42] Alkane (n-hexane and n-heptane) hydrogenolysis rates decrease concurrently with the increase of alkane isomerization rates as the extent of oxygen-modification on tungsten carbides increases, which was quantified by temperature-programmed reduction and ex situ CO chemisorption, demonstrating the metallic and acidic properties of oxygen-modified tungsten carbides.[10,11] Sullivan et al.[56] reported that a ~ 30-fold increase in propylene rate per gram Mo_2C catalyst from isopropyl alcohol dehydration at 415 K was observed when O_2 co-feed was varied from 0 to 13.5 kPa. Brønsted acid sites were found to be responsible for isopropyl alcohol dehydration to propylene on Mo_2C formulations with oxygen co-feed (0–13.5 kPa) as evidenced by the invariance of propylene rates normalized to acid sites titrated in situ by 2,6-di-tert-butylpyridine.[56] The O 1s peak at 532.5 eV assigned to surface hydroxyl species observed from X-ray photoelectron spectroscopy (XPS) on Mo_2C catalyst after H_2 pretreatment was correlated with the surface acidity of Mo_2C measured from temperature-programmed desorption of ammonia (NH_3-TPD).[180] These surface hydroxyl sites (O 1s peak at 532.5 eV) were also observed on spent Mo_2C catalysts from hydrodeoxygenation of acetic acid

at 623 K without exposure to air.[180] These results show that the catalyst function of molybdenum and tungsten carbide formulations can be tuned by varying O_2 co-feed pressure during the reaction or by changing O_2 pretreatment conditions at different temperatures.

The propensity for O_2, CO_2, and H_2O as oxidants to oxidize β-Mo_2C surface was evaluated using density-functional theory (DFT) calculations on β-Mo_2C(011) and (101) surfaces with mixed Mo/C terminations.[30] The calculated reaction energies for surface oxidation vary with oxygen coverage and the source of oxygen. The oxidizing strength of O_2 was found to be much stronger (-13 to -2 eV) than those of H_2O and CO_2 (~ -2 to 0 eV or > 0 eV) at 0 K.[183] It is, however, still unclear (i) how the differences in the oxidizing strength of O_2, CO_2, and H_2O translate to the amount of oxygen adsorbed on Mo_2C and (ii) how oxygenate-modification affects the metal-like function on Mo_2C.

In this work, we investigate the effects of oxygenate-modification on Mo_2C for m-cresol HDO and prepared oxygenate-modified Mo_2C catalysts using 1 kPa of O_2, CO_2, or H_2O, at 333 K. The independent kinetic and in situ chemical titration studies showed that two distinct sites and metal-like sites are involved in m-cresol HDO. Temperature-programmed surface reaction with H_2 was used to quantify the amount of oxygen incorporated in the catalyst from oxygenate-treatment (O/Mo_{bulk} before HDO) and/or from m-cresol HDO (O/Mo_{bulk} after HDO). We infer that molecular oxygen has a higher propensity to deposit oxygen on Mo_2C (O/Mo_{bulk} before HDO = 0.23 ± 0.02) compared to CO_2 and H_2O (O/Mo_{bulk} before HDO ~ 0.036). We also showed from in situ chemical titration and m-cresol HDO on fresh and oxygenate-modified Mo_2C catalysts that adsorbed oxygen poisons the metal-like sites responsible for m-cresol HDO, and the effect of adsorbed oxygen is agnostic to the source of oxygen.

5.2. Materials and methods

5.2.1. Kinetics and in situ chemical titration studies for m-cresol HDO

5.2.1.1. Catalyst synthesis and characterization

Molybdenum carbide catalysts were synthesized based on a prior report.[55] Ammonium molybdate tetrahydrate (~ 1.2 g, Sigma, 99.98%, trace metal basis; sieved, 177 – 400 μm, $(NH_4)_6Mo_7O_{24}\cdot 4H_2O$) was loaded to a tubular quartz reactor (I.D. 10 mm) placed in a tube furnace (Applied Test System, Series 3210) controlled by a Watlow Temperature Controller (96 series) and was treated in a gas mixture (total flow rate of ~ 2.75 $cm^3\ s^{-1}$) of 15/85 vol% of CH_4 (Matheson, 99.97%) and H_2 (Minneapolis Oxygen, 99.999%) at ~ 623 K for 5 h at a ramping rate of ~ 0.06 K s^{-1} from room temperature (RT), then treated at ~ 863 K for 3 h at a ramping rate of ~ 0.047 K s^{-1}. Passivation of the resulting material was done at RT using 1% O_2/He (Matheson, Certified Standard Purity) (~ 1.67 $cm^3\ s^{-1}$) for ~ 2 h.

N_2 adsorption/desorption (Micromeritics ASAP 2020) measurements at ~ 77 K were used to determine Brunauer−Emmett−Teller (BET) surface area of Mo_2C catalysts; the sample was degassed (< 10 μmHg) at 523 K for at least 4 h before N_2 adsorption. X-ray diffraction (XRD, Bruker D8 Discover, 2D X-ray diffractometer with a two-dimensional VÅNTEC-500 detector) was used to determine the bulk structures of molybdenum carbide samples. Two-dimensional images were collected using Cu Kα X-ray radiation with a graphite monochromator and a 0.8 mm point collimator measured in three measurement frames at $2\theta = 25^o$, 55^o, and 85^o with a 900 s frame/dwell, which were then converted to one-dimensional intensity vs. 2θ for analysis. Ex situ CO chemisorption (Matheson, 99.5%) uptake at 323 K for Mo_2C samples was measured using a Micromeritics ASAP 2020 instrument, in which ~ 0.14 g_{cat} passivated Mo_2C was treated in H_2 at 723 K for 1 h, followed by degassing (~ 2 μmHg) at 723 K for 2 h, after being evacuated at 383 K (~ 2 μmHg) for 0.5 h. The uptake of irreversibly adsorbed CO was then obtained from the difference between two adsorption isotherms (from 100 to 450 mmHg at 323 K)

extrapolated to zero pressure; the second isotherm was taken after the cell was degassed at ~ 2 μmHg to remove weakly adsorbed species. Ex situ CO chemisorption measurements were conducted within a 7-day period prior to the kinetic studies for vapour phase m-cresol HDO.

X-ray photoelectron spectroscopy measurements were performed using an SSX-100 spectrometer (Surface Science Laboratories, Inc.) with Al K_α X-ray source operating at 200 W on an area of 1 × 1 mm^2 on the samples. The high resolution spectra were collected using 50 eV pass energy and 0.1 eV $step^{-1}$. The atomic percentages were calculated from the survey spectrum (150 eV pass energy and 1 eV $step^{-1}$) using the ESCA Hawk software. The lowest energy Mo $3d_{5/2}$ peak was used as the reference peak (228.0 eV for Mo_2C).[184,185] A combination of Gaussian/Lorenzian functions with the Gaussian percentages being at 80% or higher was used for curve fitting.

5.2.1.2. Kinetic studies for vapor phase hydrodeoxygenation of m-cresol

Steady state vapor phase hydrodeoxygenation reactions of m-cresol on Mo_2C catalyst were carried out in a tubular quartz reactor (I.D. 10 mm) placed in a tube furnace (Applied Test System, Series 3210), controlled by a Watlow Temperature Controller (96 series). The reaction temperature was monitored by a thermocouple inserted in the outer thermowell of the reactor. The reactant gas mixture was comprised of m-cresol (0.03%)/ H_2 (84%)/ He (balance) (mol%) at ~ 3.33 $cm^3\ s^{-1}$ total flow rate and at ~ 112 kPa total pressure. m-Cresol (Sigma, FG, ≥98%) was added to the flow line using a syringe pump (KD Scientific, Model 100). Reactor effluents were analyzed by a flame ionization detector using an online gas chromatograph (GC, Agilent 7890) with a methyl-siloxane capillary column (HP-1, 50 m × 320 μm × 0.52 μm). All passivated molybdenum carbide samples were treated in pure H_2 (~ 1.67 $cm^3\ s^{-1}$) at 773 K (~ 0.1 K s^{-1}) for 1 h prior to reaction. All flow lines were heated to at least 398 K via resistive heating to prevent condensation of the compounds. m-Cresol conversion and C_6^+ product selectivity were calculated as follows:

$$m-Cresol\ conversion = \frac{(sum\ of\ moles\ of\ C\ in\ products)_{out}}{(moles\ of\ C\ in\ m-cresol)_{in}} \times 100\% \qquad (5.1)$$

$$C_6^+ \ product \ selectivity = \frac{moles \ of \ C_{6+} \ product \ i}{moles \ of \ C_{6+} \ products} \times 100\% \quad (5.2)$$

5.2.1.3. In situ CO titration for vapor phase hydrodeoxygenation of m-cresol

In situ CO titration studies were conducted to probe the identity and the density of the operational sites for m-cresol HDO on Mo_2C catalysts. A co-feed of CO with Ar or He as an internal tracer (0.0125, 0.025, or 0.0375 $cm^3 \ s^{-1}$ CO in 0.033 $cm^3 \ s^{-1}$ Ar) was introduced to the reactant mixture after steady state m-cresol synthesis rates were observed. The transient responses of CO and Ar/He were monitored by an online mass spectrometer (MKS Cirrus 200 Quadrupole mass spectrometer system). Toluene synthesis rates before and after CO co-feed were quantified by an online GC.

5.2.2. Oxygenate treatment studies

5.2.2.1. Oxygenate treatment on fresh Mo_2C

Fresh Mo_2C (~ 1 g_{cat}) was synthesized following the procedures described in Section 2.1.1, and was subsequently cooled to the oxygenate treatment temperature at 333 K, 363 K, or 423 K in the same CH_4/H_2 flow. The oxygenate treatment flow was then introduced to the freshly synthesized Mo_2C catalyst for 2 h in a total flow rate of 1.67 $cm^3 \ s^{-1}$ at ambient pressure. The oxygenates studied include CO_2, H_2O, and O_2 and the corresponding oxygenate treatment pressures are summarized in Scheme 5.1. Water was added to the flow lines by a syringe pump (KD Scientific, Model 100). The catalyst was then heated to 423 K in 0.5 h and held at 423 K for 1.5 h in a flow of He (10%)/ H_2 (balance) (mol%) at ambient pressure and at a total flow rate of ~ 1.83 $cm^3 \ s^{-1}$ to remove any loosely bound species from the catalyst. The nomenclature for the oxygenate-modified Mo_2C catalysts reported in this work is of the form, oxygenate–treatment pressure (temperature)–Mo_2C. A freshly synthesized molybdenum carbide catalyst that was treated with 1 kPa O_2 at 333 K, for example, is noted as O_2–1 kPa (333 K)–Mo_2C. All oxygenate-modified Mo_2C catalysts studied in this work are listed in Scheme 5.1.

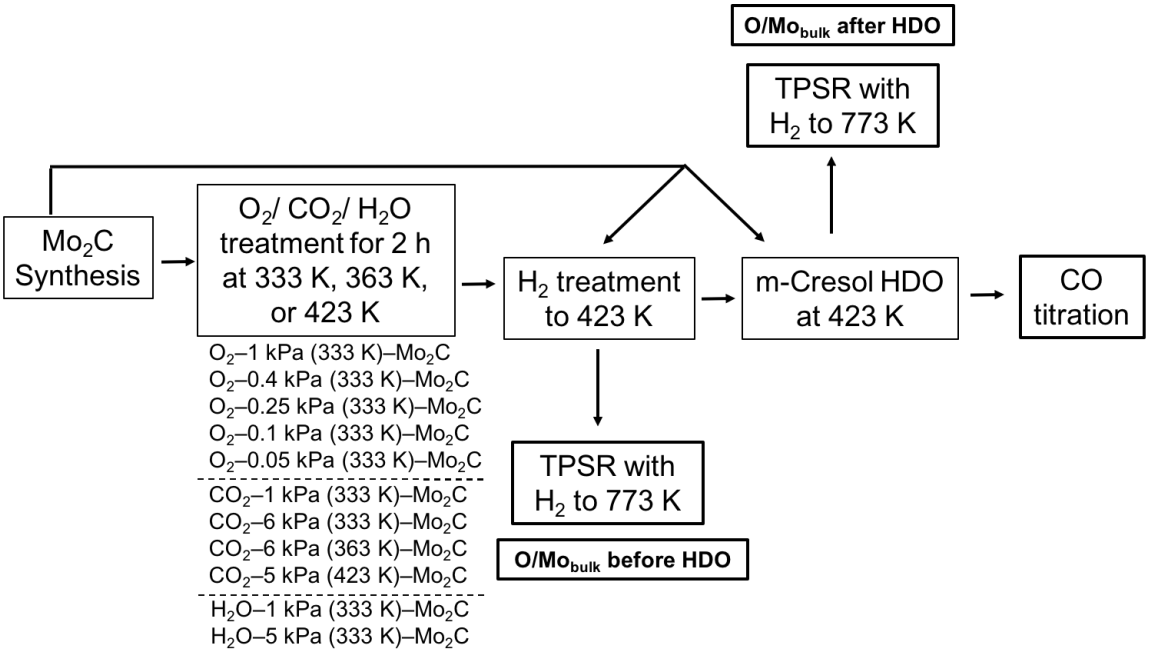

Scheme 5.1 Experimental procedures used in this study to investigate the effect of oxygenate pretreatment on Mo_2C for hydrodeoxygenation.

5.2.2.2. m-Cresol HDO on fresh/ oxygenate treated Mo_2C

Vapor phase hydrodeoxygenation was used as a probe reaction to study the effect of oxygenate-modification on Mo_2C catalysts. The reactor setup is the same as that described in section 5.2.1.2. The reactant flow for all results reported in the oxygenate treatment studies was comprised of m-cresol (1%)/ He (10%)/ H_2 (balance) (mol%), and the total flow rate was 1.83 $cm^3\ s^{-1}$ at ~ 107 kPa total pressure and at 423 K.

5.2.2.3. Temperature-programmed surface reaction with H_2 (TPSR)

Temperature-programmed surface reactions with H_2 were performed to quantify the amount of oxygen deposited on the fresh Mo_2C catalysts from oxygenate-modification and on a fresh and on an oxygenate-modified Mo_2C catalyst from m-cresol HDO at 423 K. The catalyst was heated from 423 K to 773 K in 1 h and held at 773 K for 0.5 h in a flow of He (10%)/ H_2 (balance) (mol%) at a total flow rate of ~ 1.83 $cm^3\ s^{-1}$ at ambient pressure. The oxygen uptake on the catalyst (i) after oxygenate treatment, denoted as O/Mo_{bulk} before

HDO, and (ii) after m-cresol HDO, denoted as O/Mo_{bulk} after HDO, was estimated by the H_2O signal monitored by an on-line mass spectrometer (MKS Cirrus 200 Quadrupole mass spectrometer system) during the TPSR process as H_2O was the major oxygen-containing compound that eluted from the catalyst. The observed H_2O signal during TPSR process is similar to that noted by Lee et al.[54] and Choi et al.[7] for TPSR with H_2 on Mo_2C after anisole HDO at 423 K and TPSR with H_2 for the as-prepared Mo_2C catalysts, respectively. Scheme 5.1 illustrates the experimental procedures for the oxygenate treatment studies. The values of O/Mo_{bulk} were obtained from Equation 5.3.

$$O/Mo_{bulk} = \frac{moles\ of\ oxygen\ uptake\ measured\ from\ TPSR}{moles\ of\ Mo\ in\ Mo_2C} \quad (5.3)$$

Independent TPSR with H_2 experiments were conducted on the fresh Mo_2C, O_2–1 kPa (333 K)–Mo_2C, H_2O–1 kPa (333 K)–Mo_2C, and CO_2–1 kPa (333 K)–Mo_2C catalysts in which, after the oxygenate treatment, the catalyst was heated to 773 K in 1 h and held at 773 K for 0.5 h, then subsequently heated to 973 K in 0.5 h and held at 973 K for 2 h in a flow of He (10%)/ H_2 (balance) (mol%) at a total flow rate of ~ 1.83 $cm^3\ s^{-1}$ and at ambient pressure (Figure 5.9 in Section 5.5). We confirmed that the majority of the oxygen added to the fresh Mo_2C catalyst from the oxygenate treatment is accounted for from TPSR with H_2 at 773 K as we show that (i) an amount of residual oxygen (O/Mo_{bulk} ~ 0.07, Figure 5.9a in Section 5.5) was observed on a freshly synthesized Mo_2C catalyst and it can only be removed at a temperature higher than 823 K (Figure 5.9a in Section 5.5), and (ii) the values of O/Mo_{bulk} before HDO quantified from TPSR with H_2 at 773 K are comparable to those quantified via TPSR with H_2 at 973 K (± 10%) after subtracting the amount of residual oxygen (O/Mo_{bulk} ~ 0.07) in a freshly synthesized Mo_2C catalyst (Table 5.3 in Section 5.5).

5.3. Results and discussion

5.3.1. Kinetics and in situ chemical titration studies for m-cresol HDO

5.3.1.1. Kinetic studies for vapor phase hydrodeoxygenation of m-cresol

Molybdenum carbide catalysts have been shown to selectively catalyze vapor phase anisole HDO at 423 K and ambient H_2 pressure (>90% C_6^+ selectivity for benzene and cyclohexane).[127,182] Similar to anisole HDO on Mo_2C, high selectivity for toluene (>90% C_6^+ selectivity) was observed from m-cresol HDO on Mo_2C at ambient pressure and at temperatures between 423 K and 483 K for ~ 240 ks on-stream (Figure 5.1a). A less than 5% decrease in m-cresol conversion at 423 K was observed after two temperature cycles (423–483 K) were employed during the ~ 240 ks on-stream (Figure 5.1b), demonstrating that the catalyst was stable for m-cresol HDO. High selectivity (>75%) to toluene from vapor phase m-cresol HDO has also been reported under ambient pressure on Pd/Fe_2O_3 catalysts at 573 K,[186] Pt/H-BEA at 623 K and 673 K,[187,188] Pt/SiO_2 at 553 K,[189] and 10 wt% MoO_3/ZrO_2 (>99% toluene selectivity)[190] at 593 K, and at ~ 5 atm on Pt/TiO_2 at 623 K.[191] m-Cresol conversion on these catalysts, however, decreases with time-on-stream (TOS).[188–190]

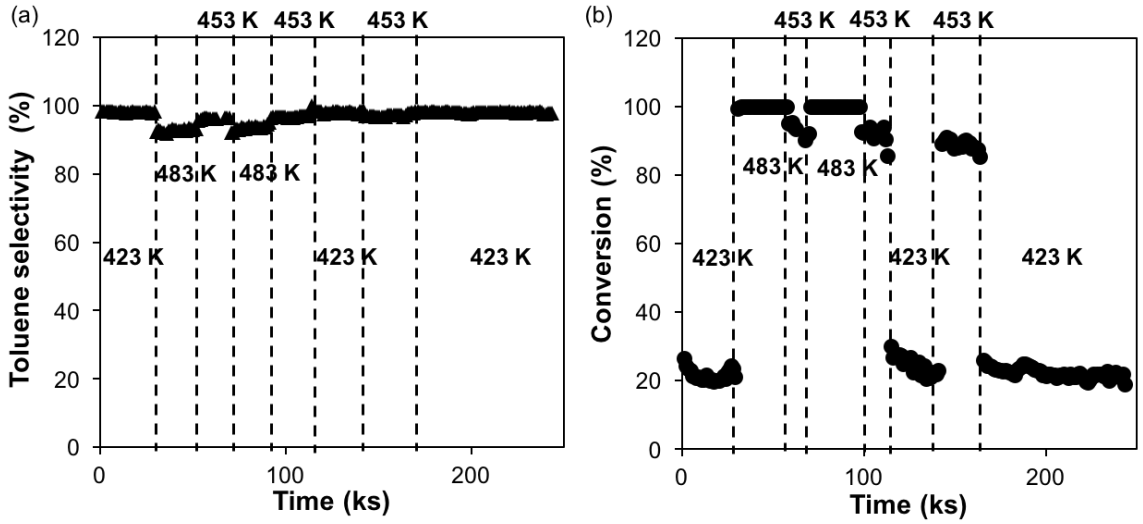

Figure 5.1 (a) Toluene selectivity and (b) m-cresol conversion for m-cresol HDO on Mo_2C. Feed = m-cresol (0.04%)/ H_2 (balance) (mol%) at ~ 108 kPa total pressure and at 423 K; total flow rate ~ 2.17 $cm^3\ s^{-1}$; 0.14 g_{cat} Mo_2C catalyst; ~ 94 μmol g_{cat}^{-1} ex situ CO uptake.

The turnover frequencies (TOF) of toluene synthesis determined by ex situ CO chemisorption on Mo_2C are zero order dependent on m-cresol pressure (0.03–1.5 kPa) and

near half order dependent on H_2 pressure (10–110 kPa) (Figure 5.2a), suggesting that two distinct sites are required for toluene synthesis on molybdenum carbide catalyst, consistent with the previously reported reaction mechanism for anisole HDO on bulk Mo_2C and W_2C catalysts.[127,182] The apparent activation energy for toluene synthesis estimated from the Arrhenius plot (Figure 5.2b) between 400–450 K is ~ 94 ± 2 kJ mol^{-1} for m-cresol HDO on Mo_2C.

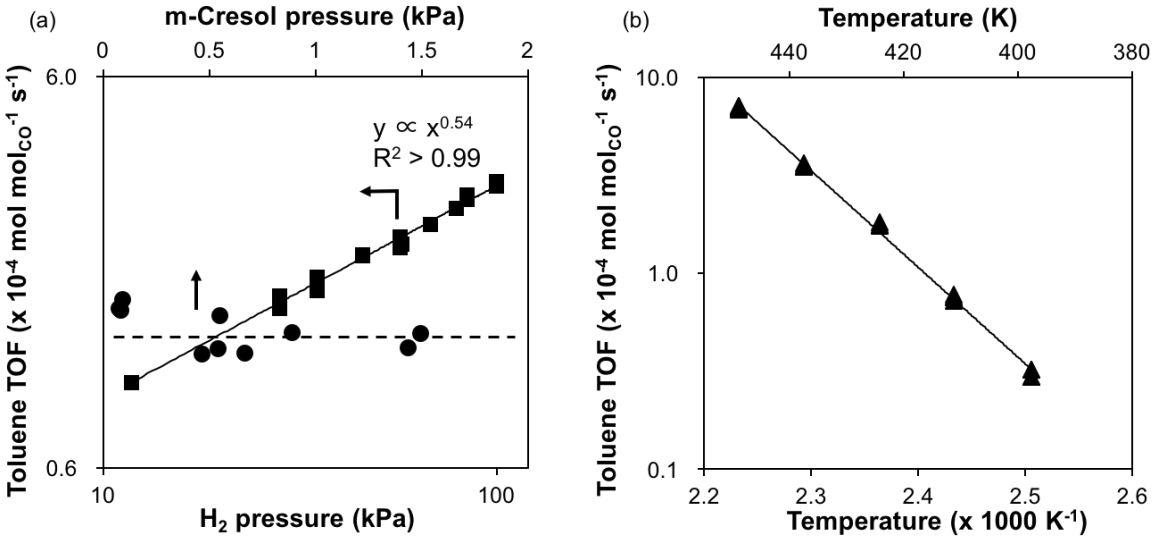

Figure 5.2 (a) Effect of H_2 pressure (■) and m-cresol pressure (●) on turnover frequencies (TOF) of toluene synthesis determined by ex situ CO chemisorption (184–240 μmol g_{cat}^{-1}) on Mo_2C catalysts at ~ 110 kPa total pressure and at 423 K. H_2 pressure was varied from 10–110 kPa (balance He) at 0.03 kPa m-cresol pressure; m-cresol pressure was varied from 0.03–1.5 kPa at 50 kPa H_2 pressure (balance He); total flow rate ~ 3.33 cm^3 s^{-1}; ~ 0.02–0.06 g_{cat} Mo_2C. (b) Temperature dependencies for TOF of toluene synthesis (▲) determined by ex situ CO chemisorption (236 μmol g_{cat}^{-1}) from m-cresol HDO at ~ 112 kPa total pressure and at 400–450 K. m-Cresol pressure ~ 0.028 kPa; total flow rate ~ 3.33 cm^3 s^{-1}; ~ 0.016 g_{cat}.

5.3.1.2. In situ CO titration for vapor phase hydrodeoxygenation of m-cresol

The number of operational sites during vapor phase m-cresol HDO were determined by in situ CO titration and were subsequently used to assess TOF of toluene synthesis. A

co-feed of pure CO (0.4–1.1 kPa) with Ar as an internal tracer was introduced (the shaded areas in Figure 5.3a) when steady state toluene synthesis rates were reached. Toluene synthesis rates from m-cresol HDO on Mo_2C catalyst were inhibited in presence of CO co-feed and were recovered when the co-feed was removed, suggesting that CO is a reversible titrant for m-cresol HDO, similar to anisole HDO on Mo_2C and W_2C catalysts.[54,182] These

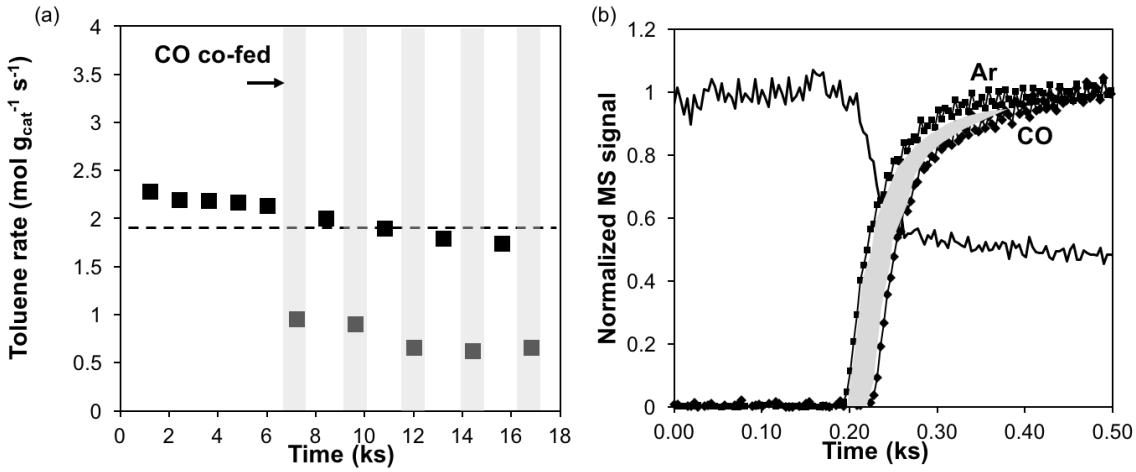

Figure 5.3 (a) Toluene synthesis rates vs. time-on-stream and (b) normalized transient mass spectrometer signals of toluene (m/z = 91), Ar (m/z = 40), and CO (m/z = 28) as a function of time during the course of in situ CO titration for m-cresol HDO over ~ 4 g_{cat} Mo_2C catalyst (75 μmol g_{cat}^{-1} ex situ CO uptake) at ~ 120 kPa total pressure and at 423 K. m-Cresol (0.3%)/ H_2 (balance) (mol%), total flow rate ~ 3.33 cm^3 s^{-1}, 28% conversion. Co-feed flow rates: 0.0125, 0.025, or 0.0375 cm^3 s^{-1} CO in 0.033 cm^3 s^{-1} Ar.

results suggest that metal-like sites[192,193] are involved in Ar-OH bond cleavage.

The total number of CO adsorbed during the course of in situ titration for m-cresol HDO was obtained by integrating the area circumscribed by the Ar and CO signals in the mass spectrometer (Figure 5.3b) and multiplying it by the corresponding CO flow rate. Turnover frequency of toluene synthesis was then estimated by dividing the difference in toluene synthesis rates without and with CO co-feed by the amount of CO adsorbed. Turnover frequency of toluene synthesis from m-cresol HDO on Mo_2C catalyst is ~ (3.6 ± 0.7) × 10^{-3} mol mol_{CO}^{-1} s^{-1} at 423 K, which is of the same order of magnitude as TOF of benzene synthesis from anisole HDO on Mo_2C formulations at 423 K (~ 1 × 10^{-3} mol

mol_{CO}^{-1} s^{-1}),[54,182] suggesting that the identity of the sites for Ar–OH and Ar–OCH_3 cleavage are similar. Carbon monoxide is shown to be a selective titrant for at least one of the two distinct sites responsible for m-cresol HDO as turnover frequencies of toluene synthesis from m-cresol HDO measured at different CO co-feed pressures (0.4–1.1 kPa) are consistent (~ $(3.6 \pm 0.7) \times 10^{-3}$ mol mol_{CO}^{-1} s^{-1}), similar to that reported by Lee et al.[54] in which turnover frequencies of benzene synthesis from anisole HDO measured at 0.4–3 kPa CO co-feed pressures are nearly invariant (~ $(1.1 \pm 0.3) \times 10^{-3}$ mol mol_{CO}^{-1} s^{-1}).

5.3.2. Oxygenate treatment studies

5.3.2.1. Mo_2C modification by CO_2, H_2O, and O_2

Edamoto et al.[194] showed from surface science studies that O_2 can adsorb dissociatively on a C or Mo-terminated $Mo_2C(0001)$ surface at room temperature as evidenced by XPS analysis in which the peaks on the C 1s and Mo 3d spectra of an O_2-treated $Mo_2C(0001)$ surface broadened and shifted to the higher binding energy side compared to those measured on a clean surface. DFT calculations from Shi et al.[195] also showed that O_2 adsorbs dissociatively and exothermically on low-index surfaces including clean or oxygen-covered β-$Mo_2C(100)$ and β-$Mo_2C(011)$ surfaces with negative adsorption energies (approximately -3 eV at 0 K). Lee et al.[54] previously prepared an O_2-modified bulk β-Mo_2C using an approach similar to that reported by Ribeiro et al.[12,196] TPSR with H_2 experiment on the O_2-modified bulk β-Mo_2C catalyst monitored by an on-line mass spectrometer showed that oxygen were left behind on the surface and were removed as H_2O by H_2.

DFT calculations in studying the mechanism for water-gas-shift reaction on Mo or C-terminated β-$Mo_2C(001)$ surfaces[48] and on a β-$Mo_2C(001)$ slab[50] suggest that H_2O and CO_2 can dissociate on the surfaces. The bonding energies for O* formation from $H_2O_{(g)}$ ($H_2O_{(g)} \rightarrow O^* + H_{2(g)}$) on Mo and C-terminated β-$Mo_2C(001)$ surfaces with 0.2 – 1.2 monolayers of oxygen coverage were found to be approximately -1.5 eV to -5.5 eV and -0.5 eV to -1.5 eV, respectively.[48] Porosoff and coworkers[197] have probed and established CO_2

dissociation on a model Mo_2C surface prepared by carburizing an Mo(110) substrate using ambient-pressure X-ray photoelectron spectroscopy (AP-XPS) and TPSR experiments monitored by mass spectrometry. A C 1s peak at 283.6 eV assigned to oxycarbide (O-Mo-C) and an O 1s peak at 531.7 eV assigned to oxygen bonded to carbon were observed on the model Mo_2C surface both when exposed to 150 mTorr CO_2 and under CO_2 hydrogenation reaction conditions (150 mTorr CO_2 and 553 mTorr H_2 at 523 K),[197] suggesting that CO_2 is dissociated to O and CO on a Mo_2C/Mo(110) surface.

The amount of oxygen deposited from the oxygenate treatments (O/Mo_{bulk} before HDO) on O_2–1 kPa (333 K)–Mo_2C, H_2O–1 kPa (333 K)–Mo_2C, and CO_2–1 kPa (333 K)–Mo_2C catalysts quantified using TPSR with H_2 at 773 K are summarized in Table 5.1. The value of O/Mo_{bulk} before HDO on O_2–1 kPa (333 K)–Mo_2C (O/Mo_{bulk} = 0.23 ± 0.02) is approximately 6 times of that on H_2O–1 kPa (333 K)–Mo_2C (O/Mo_{bulk} = 0.038 ± 0.010) and CO_2–1 kPa (333 K)–Mo_2C (O/Mo_{bulk} = 0.035 ± 0.010), demonstrating that O_2 has a stronger propensity to leave behind adsorbed oxygen on a fresh Mo_2C. A temperature exotherm ($\Delta T \sim 20$ K) was observed when 1 kPa of O_2 was introduced to the fresh Mo_2C at 333 K, however, the temperature exotherm observed when introducing 1 kPa of H_2O or CO_2 to the fresh Mo_2C at 333 K was only about 2 K. These experimental observations are consistent with the DFT calculations reported by Liu and Rodriguez[48] in which O_2 adsorption energies on Mo-terminated and C-terminated Mo_2C(001) surfaces (-8.15 eV and -5.4 eV) were found to be stronger than those for H_2O adsorption (-1.52 eV and -1.33 eV) and CO_2 adsorption (-0.88 eV and -0.27 eV) on the same surfaces. Thermodynamic calculations also show that the oxidizing strength of $O_{2(g)}$ is stronger than that of $H_2O_{(g)}$ for the formation of $MoO_{2(s)}$ ($\Delta G_{rxn,\ 600\ K}$ = -1301 kJ mol^{-1} vs. $\Delta G_{rxn,\ 600\ K}$ = -17 kJ mol^{-1}) or $MoO_{3(s)}$ ($\Delta G_{rxn,\ 600\ K}$ = -1530 kJ mol^{-1} vs. $\Delta G_{rxn,\ 600\ K}$ = 183 kJ mol^{-1}) from $Mo_2C_{(s)}$.[198,199]

5.3.2.2. m-Cresol HDO on CO_2, H_2O, or O_2 modified Mo_2C

Vapor phase m-cresol HDO at 423 K was performed on fresh Mo_2C, O_2–1 kPa (333 K)–Mo_2C, H_2O–1 kPa (333 K)–Mo_2C, and CO_2–1 kPa (333 K)–Mo_2C catalysts to

investigate the effects of oxygenate modification on the metal-like properties of Mo_2C. Toluene synthesis rates reported in this work are average values taken between 7.2–14.4 ks on-stream as the decrease in toluene synthesis rates observed in this regime is less than 5% on all the samples (Figure 5.4). Toluene synthesis rates from m-cresol HDO are similar on fresh Mo_2C, H_2O–1 kPa (333 K)–Mo_2C, and CO_2–1 kPa (333 K)–Mo_2C catalysts (8.3 – 9.6 × 10^{-8} mol g_{cat}^{-1} s^{-1}, Table 5.1), suggesting that the surface environment of these catalysts is similar. The different values of O/Mo_{bulk} before HDO measured on these samples showed that the value of O/Mo_{bulk} before HDO is not the relevant amount of oxygen adsorbed on the catalyst for toluene synthesis in this regime. Toluene rate on O_2–1 kPa (333 K)–Mo_2C, however, is an order of magnitude smaller (6.1 × 10^{-9} mol g_{cat}^{-1} s^{-1}) than those measured on fresh Mo_2C, H_2O–1 kPa (333 K)–Mo_2C, and CO_2–1 kPa (333 K)–Mo_2C catalysts.

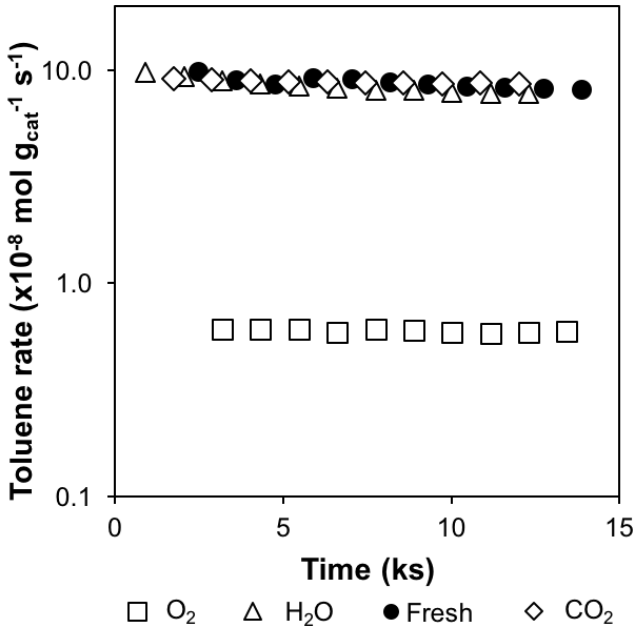

Figure 5.4 Toluene synthesis rates from m-cresol HDO over (●) fresh Mo_2C, (△) H_2O–1 kPa (333 K)–Mo_2C, (◇) CO_2–1 kPa (333 K)–Mo_2C, and (□) O_2–1 kPa (333 K)–Mo_2C catalysts. Feed = m-cresol (1%)/ He (10%)/ H_2 (balance) (mol%) at ~ 107 kPa total pressure and at 423 K; total flow rate 1.83 cm^3 s^{-1}; 1 g_{cat}.

BET surface area measurements were performed on the spent fresh Mo_2C, O_2–1 kPa (333 K)–Mo_2C, and CO_2–1 kPa (333 K)–Mo_2C catalysts after m-cresol HDO, which were subsequently treated in 1% O_2/He at ~ 5.8 cm^3 s^{-1} for ~ 1 ks at RT to passivate the pyrophoric Mo_2C prior to the measurements. The BET surface area (Table 5.1) for the spent O_2–1 kPa (333 K)–Mo_2C catalyst (76 m^2 g_{cat}^{-1}) is only ~ 20% lower than that for the spent fresh Mo_2C catalyst (96 m^2 g_{cat}^{-1}), which cannot account for the observed 10-fold decrease in toluene synthesis rate on O_2–1 kPa (333 K)–Mo_2C compared to that on the fresh Mo_2C catalyst. The change in surface area is therefore, not the major cause for the decrease in toluene synthesis rates on the O_2–1 kPa (333 K)–Mo_2C catalyst.

Oxygen uptake on the catalyst under m-cresol HDO environment was quantified from TPSR with H_2 performed subsequently after m-cresol HDO on fresh Mo_2C, O_2–1 kPa (333 K)–Mo_2C, H_2O–1 kPa (333 K)–Mo_2C, and CO_2–1 kPa (333 K)–Mo_2C catalysts and the values of O/Mo_{bulk} after HDO are reported in Table 5.1. Oxygen accumulation was observed on the fresh Mo_2C (O/Mo_{bulk} ~ 0.05 ± 0.01) from m-cresol HDO at 423 K, similar to that reported by Lee et al.[54] in which oxygen accumulation equivalent of O/Mo_{bulk} ~ 0.045 was observed on a passivated Mo_2C that was treated in H_2 at 723 K for 1 h prior to the reaction study of anisole HDO at ambient pressure and 423 K. The values of O/Mo_{bulk} after HDO on H_2O–1 kPa (333 K)–Mo_2C and CO_2–1 kPa (333 K)–Mo_2C catalysts are similar (Table 5.1, O/Mo_{bulk} ~ 0.06 ± 0.01) but higher than the values of O/Mo_{bulk} before HDO on the same catalysts, indicating that additional oxygen was deposited to these catalysts from m-cresol HDO. The values of O/Mo_{bulk} after HDO and before HDO on O_2–1 kPa (333 K)–Mo_2C were found to be similar (O/Mo_{bulk} ~ 0.23 ± 0.02), suggesting that the oxygen uptake on Mo_2C catalysts is determined by the oxygen source that has a higher propensity for oxygen deposition. These results also show that the value of O/Mo_{bulk} after HDO correlates with m-cresol HDO rates on oxygenate-modified Mo_2C catalysts as toluene synthesis rates are the same on the fresh Mo_2C, H_2O–1 kPa (333 K)–Mo_2C, and CO_2–1 kPa (333 K)–Mo_2C catalysts, all of which have comparable values of O/Mo_{bulk} after HDO (Table 5.1, O/Mo_{bulk} ~ 0.06 ± 0.01).

Table 5.1 O/Mo_{bulk} ratios before and after m-cresol HDO; m-cresol conversion, toluene synthesis rates, and turnover frequencies of toluene synthesis from m-cresol HDO on fresh Mo_2C, O_2–1 kPa (333 K)–Mo_2C, H_2O–1 kPa (333 K)–Mo_2C, CO_2–1 kPa (333 K)–Mo_2C, and O_2–0.05 kPa (333 K)–Mo_2C catalysts and their corresponding BET surface area after m-cresol HDO. Feed = m-cresol (1%)/ He (10%)/ H_2 (balance) (mol%) at ~ 107 kPa total pressure and at 423 K; total flow rate 1.83 $cm^3\ s^{-1}$; 1 g_{cat}.

	O_2–0.05 kPa (333 K)–Mo_2C	O_2–1 kPa (333 K)–Mo_2C	H_2O–1 kPa (333 K)–Mo_2C	CO_2–1 kPa (333 K)–Mo_2C	Fresh Mo_2C
O/Mo_{bulk} before HDO	0.030 ± 0.005	0.23 ± 0.02	0.038 ± 0.010	0.035 ± 0.010	0
O/Mo_{bulk} after HDO	0.054 ± 0.005	0.23 ± 0.02	0.07 ± 0.01	0.06 ± 0.01	0.05 ± 0.01
Conversion (%)	~18	~1.5	~18	~18	~21
Toluene Rate ($\times 10^{-8}$ mol g_{cat}^{-1} s^{-1})	7.9	0.61	8.3	8.7	9.6
Toluene TOF ($\times 10^{-3}$ mol mol_{CO}^{-1} s^{-1})	3.8 ± 0.8	2.1 ± 0.4	3.4 ± 0.5	4.5 ± 0.8	4.5 ± 0.7
Site density (μmol g_{cat}^{-1})	21	3	25	19	21
BET surface area (m^2 g_{cat}^{-1})	83	76	n/a	81	96

[1] O_2–0.05 kPa (333 K)–Mo_2C treatment conditions: 0.083 $cm^3\ s^{-1}$ 1% O_2/He with 1.58 $cm^3\ s^{-1}$ Ar.

5.3.2.3. The roles of adsorbed oxygen on CO_2, H_2O, or O_2-modified Mo_2C for m-cresol HDO

In situ CO titration experiments were conducted to probe the identity and the density of active sites responsible for m-cresol HDO on fresh Mo_2C, O_2–1 kPa (333 K)–Mo_2C, H_2O–1 kPa (333 K)–Mo_2C, and CO_2–1 kPa (333 K)–Mo_2C catalysts. Turnover frequencies of toluene synthesis on fresh and oxygenate-modified Mo_2C catalysts are consistent (~ $2.1 \times 10^{-3} - 4.5 \times 10^{-3}$ mol mol_{CO}^{-1} s^{-1} at 423 K, Table 5.1, Figure 5.5, and Figure 5.11 in Section 5.5) and comparable to TOF of toluene synthesis measured on a Mo_2C formulation that had been passivated by 1% O_2/He but pretreated in H_2 prior to reaction studies (~ $(3.6 \pm 0.7) \times 10^{-3}$ mol mol_{CO}^{-1} s^{-1} at 423 K) as shown in Section 5.1.3, demonstrating that the incorporation of oxygen in Mo_2C alters the number and not the identity of sites for m-cresol HDO, similar to the observation reported for anisole HDO on O_2-treated Mo_2C catalyst.[54] The 10-fold decrease in toluene synthesis rates on O_2–1 kPa (333 K)–Mo_2C compared to that on fresh Mo_2C, H_2O–1 kPa (333 K)–Mo_2C, and CO_2–1 kPa (333 K)–Mo_2C catalysts could result from the active sites that are involved in toluene synthesis and can be titrated by CO being poisoned by the additional amount of oxygen adsorbed (> 0.06 ± 0.01 O/Mo_{bulk}) on the O_2–1 kPa (333 K)–Mo_2C catalyst (Table 5.1).

Oxygen adsorbed in amounts exceeding O/Mo_{bulk} ~ 0.06 ± 0.01 on O_2–1 kPa (333 K)–Mo_2C was found to inhibit HDO rate by poisoning the active sites as discussed above. The bulk structure of the spent and passivated fresh Mo_2C and O_2–1 kPa (333 K)–Mo_2C catalysts, however, remained as β-Mo_2C and no MoO_2 or MoO_3 peaks were observed (Figure 5.10 in Section 5.5), indicating that the decrease in HDO rate was not resulted from bulk oxidation of Mo_2C. The percentage of surface Mo in Mo^{5+} and/or Mo^{6+} (231.5 eV) states measured from XPS on the spent and passivated O_2–1 kPa (333 K)–Mo_2C (26.7%) was found to be higher than that on the spent and passivated fresh Mo_2C (15.5%) (Table 5.4 in Section 5.5), suggesting that (i) the decrease in the number of active sites on O_2–1 kPa (333 K)–Mo_2C compared to that on fresh Mo_2C could result from the surface Mo being

oxidized to higher oxidation states and (ii) the higher amount of oxygen deposited from 1 kPa of O_2 correlates with the higher fraction of surface Mo being in Mo^{5+} and/or Mo^{6+} oxidation states.

An O_2–0.05 kPa (333 K)–Mo_2C catalyst (O/Mo_{bulk} before HDO ~ 0.03) was prepared to investigate the effect of adsorbed oxygen from O_2 deposition compared to that deposited from H_2O and CO_2 as H_2O–1 kPa (333 K)–Mo_2C and CO_2–1 kPa (333 K)–Mo_2C catalysts have similar values of O/Mo_{bulk} before HDO and exhibit similar toluene synthesis rates, TOF of toluene synthesis, and O/Mo_{bulk} after HDO. Toluene synthesis rates (7.9×10^{-8} mol g_{cat}^{-1} s^{-1}) and TOF of toluene synthesis ($3.8 \pm 0.8 \times 10^{-3}$ mol mol_{CO}^{-1} s^{-1}) from m-cresol HDO at 423 K and the value of O/Mo_{bulk} after HDO (0.054 ± 0.005) on O_2–0.05 kPa (333 K)–Mo_2C catalyst were found to be similar to that measured on H_2O–1 kPa (333 K)–Mo_2C, CO_2–1 kPa (333 K)–Mo_2C, and fresh Mo_2C catalysts (Table 5.1), clearly demonstrating that the effect of adsorbed oxygen on Mo_2C is agnostic to the oxygen source under the reaction conditions investigated.[200]

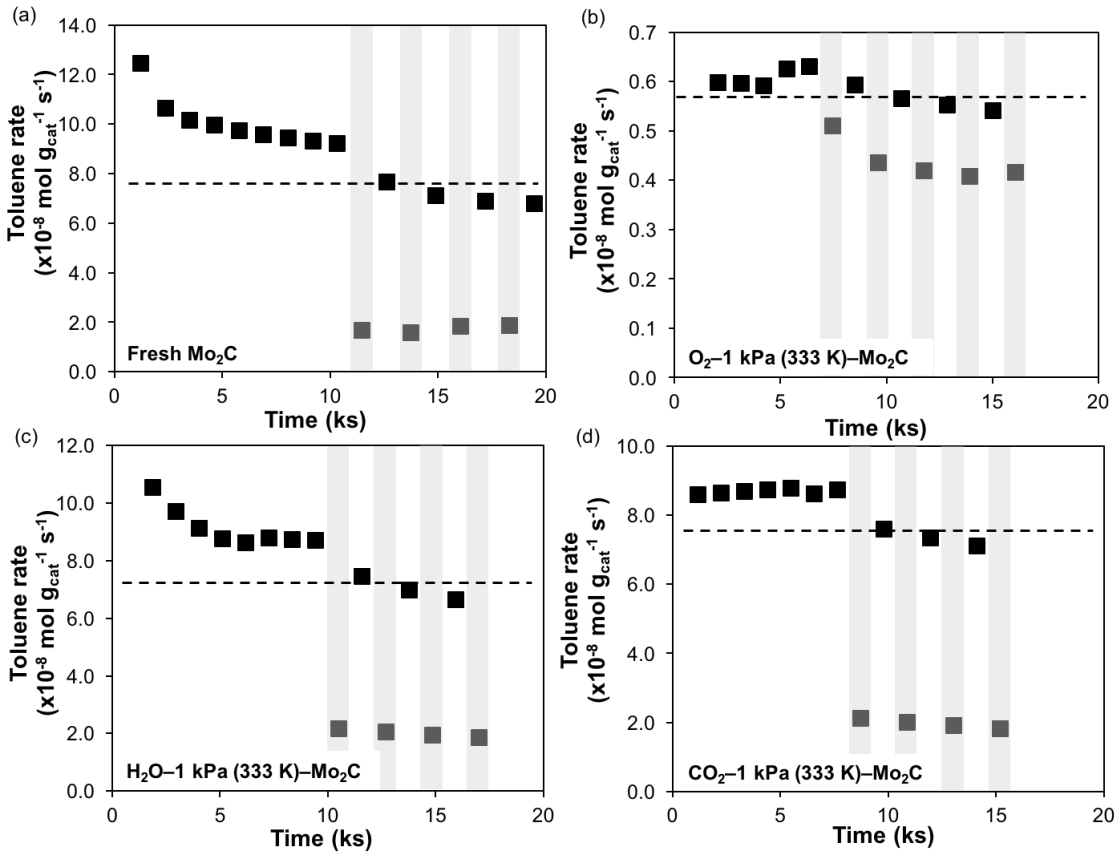

Figure 5.5 Toluene synthesis rates vs. time-on-stream for m-cresol HDO on (a) fresh Mo_2C, (b) O_2–1 kPa (333 K)–Mo_2C, (c) H_2O–1 kPa (333 K)–Mo_2C, and (d) CO_2–1 kPa (333 K)–Mo_2C catalysts. Feed = m-cresol (1%)/ Ar (10%)/ H_2 (balance) (mol%) at ~ 107 kPa total pressure and at 423 K; total flow rate 1.83 $cm^3\ s^{-1}$; 1 g_{cat}. CO co-feed: CO (0.5-0.93%)/ m-cresol (1%)/ He (10%)/ H_2 (balance) (mol%) at ~ 107 kPa total pressure and at 423 K; total flow rate 1.83 $cm^3\ s^{-1}$ (CO pressure for (b) is 0.05–0.07 kPa).5.3.2.4. Changing O/Mo_{bulk} ratios and HDO rates by varying O_2 pressure

We varied O_2 treatment pressure from 0.1 kPa to 0.4 kPa to study the effect of the amount of oxygen adsorbed exceeding O/Mo_{bulk} ~ 0.06 ± 0.01 on toluene synthesis rate. Figure 5.6a shows that the value of O/Mo_{bulk} before HDO increases monotonically with O_2 pressure. Toluene synthesis rates on oxygenate-modified Mo_2C catalysts are shown as a function of the value of O/Mo_{bulk} after HDO in Figure 5.6b. A 2-fold increase in the value of O/Mo_{bulk} after HDO (from ~ 0.07 to 0.13) results in a 10-fold decrease in the toluene

rate (from ~ 8×10^{-8} mol g_{cat}^{-1} s^{-1} to 8×10^{-9} mol g_{cat}^{-1} s^{-1}). The drop in toluene rates slows down as the value of O/Mo_{bulk} after HDO increased from ~ 0.13 to ~ 0.23 in which toluene synthesis rate on O_2–1 kPa (333 K)–Mo_2C (O/Mo_{bulk} after HDO ~ 0.23) is ~ 30% of that on O_2–0.4 kPa (333 K)–Mo_2C (O/Mo_{bulk} after HDO ~ 0.13). These results suggest that oxygen adsorption can occur on sites that are irrelevant to m-cresol HDO. Shi et al.[30] have shown from computational studies that the reaction energy of surface oxidation by O_2 at 0 K on Mo_2C(101) is ~ 2 eV stronger than that on Mo_2C(011), indicating that O_2 adsorption can preferentially occur on Mo_2C surfaces. We cannot, however, preclude the possibility that some adsorbed oxygen can be incorporated into the bulk structure of Mo_2C at higher values of O/Mo_{bulk} ratio.[8,201] The non-linear decrease in toluene rates observed could also result from a change in the surface morphology with a change in surface oxygen coverage as Shi et al.[195] reported from DFT calculations that the equilibrium crystal shape (ECS) of a polycrystalline β-Mo_2C with a low oxygen coverage (~ 1.6 oxygen atom nm^{-2}) at RT is similar to that with a clean surface, but becomes dominated by Mo_2C(111) and Mo_2C(101) surfaces at a higher oxygen coverage (~ 10 oxygen atom nm^{-2}).

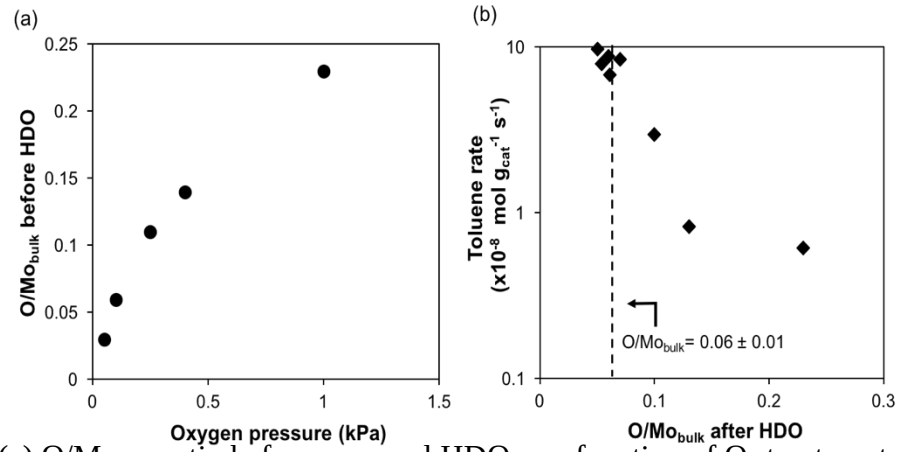

Figure 5.6 (a) O/Mo_{bulk} ratio before m-cresol HDO as a function of O_2 treatment pressure. (b) Toluene synthesis rate as a function of O/Mo_{bulk} ratio after m-cresol HDO. Oxygen treatment conditions for O_2–0.1 kPa (333 K)–Mo_2C: 0.167 cm^3 s^{-1} 1% O_2/He in 1.5 cm^3 s^{-1} Ar; O_2–0.25 kPa (333 K)–Mo_2C: 0.416 cm^3 s^{-1} 1% O_2/He in 1.25 cm^3 s^{-1} Ar; O_2–0.4 kPa (333 K)–Mo_2C: 0.67 cm^3 s^{-1} 1% O_2/He in 1 cm^3 s^{-1} Ar. m-Cresol HDO conditions: Feed = m-cresol (1%)/ Ar (10%)/ H_2 (balance) (mol%) at ~ 107 kPa total pressure and at 423 K; total flow rate 1.83 cm^3 s^{-1}; 1 g_{cat}.

5.3.2.5. m-Cresol adsorption on CO_2, H_2O, or O_2-modified Mo_2C

We analyzed the transient mass spectrometer signals of m-cresol (m/z = 107), toluene (m/z = 92), methylcyclohexane (m/z = 83), and water (m/z = 18) during the initial transient of m-cresol HDO on oxygenate-modified Mo_2C catalysts to investigate m-cresol adsorption properties on fresh Mo_2C and oxygenate-modified Mo_2C catalysts. No oxygen-containing compound was observed before m-cresol breakthrough on the fresh Mo_2C (Figure 5.7a); in contrast, a significant water peak was observed on every oxygenate-modified Mo_2C sample (Figure 5.7b–f), demonstrating that oxygen deposition occurred on the fresh Mo_2C catalyst during the initial transient. A signal of methylcyclohexane (m/z = 83) was observed initially but then dropped to almost zero during the course of oxygen deposition on fresh Mo_2C (Figure 5.7a) and was followed by an increase in the toluene signal (m/z = 92), suggesting that hydrogenation of toluene occurred and was inhibited by oxygen deposition. This observation is similar to that reported by Lee et al.[54] for anisole HDO on a passivated Mo_2C but pretreated with H_2 at ~ 750 K for 1 h before the reaction study at 423 K. Methylcycohexane signal from m-cresol HDO on every oxygenate-modified Mo_2C catalyst, however, is negligible (Figure 5.7b–f), consistent with prior reports that oxygen deposition on Mo_2C poisons aromatic hydrogenation functionality.[54,55,127]

A mass balance was employed to estimate the amount of m-cresol adsorbed and water desorbed during the initial transient of m-cresol HDO before m-cresol breakthrough as shown in Figure 5.7 in which time zero indicates the time when m-cresol was introduced to the catalyst. The amount of m-cresol adsorbed (~ 5.6×10^{-4} mol g_{cat}^{-1}) was found to be similar on the fresh and oxygenate-modified Mo_2C catalysts (Figure 5.8, black bar). The amount of water desorbed, however, correlates with the amount of oxygen pre-deposited (equal to or less than 5.6×10^{-4} mol g_{cat}^{-1}) from oxygenate treatments (Figure 5.8, white bar and white diamond). These results suggest that m-cresol adsorption occurs on the same site as the pre-deposited oxygen. We postulate that the site for m-cresol adsorption can be an oxygen vacancy site, which can be either empty or occupied by the pre-deposited

oxygen that can subsequently leave as water upon the introduction of m-cresol with H_2. We note that the pre-deposited oxygen on these sites cannot be further removed by H_2 at 423 K before m-cresol is introduced as demonstrated by the H_2 treatment procedure in the oxygenate treatment process before m-cresol HDO (Scheme 5.1). Prasomsri et al.[25,202] first proposed that a reverse Mars-van Krevelen (MvK) mechanism is involved in hydrodeoxygenation of biomass-derived oxygenates in which direct C–O bond cleavage occurs on the oxygen vacancy sites on MoO_3. Computational studies using a Mo_3O_9 cluster suggest that the regeneration of an oxygen vacancy site by H_2 is energetically feasible on a fully oxidized MoO_3.[202] A recent study by Schaidle et al.[180] showed that HDO of acetic acid on Mo_2C undergoes a reverse MvK mechanism as a Mo–O stretching peak (1008 cm^{-1}) was observed by in situ diffuse reflectance infrared Fourier transform spectroscopy (DRIFTS) for acetic acid adsorption on Mo_2C at 673 K. The involvement of oxygen vacancy sites for deoxygenation reactions on reducible metal oxides has also been reported in computational studies for m-cresol HDO on Pt/TiO_2[191] and C–O bond cleavage on Ru/RuO_2.[203]

Kinetic studies have clearly demonstrated that two distinct sites, H_2 dissociation and m-cresol adsorption, are involved in toluene synthesis. The invariance of the number of sites for m-cresol adsorption (Figure 5.8) with a concurrent decrease in the number of metal-like sites (Table 5.1) suggests that the two distinct sites are (i) metal-like sites for H_2 dissociation and (ii) m-cresol adsorption sites, presumably oxygen vacancy sites. The observation that metal-like sites responsible for H_2 dissociation are poisoned by oxygen adsorbed in amounts exceeding ~ 5.6×10^{-4} mol g_{cat}^{-1} (equivalent of ~ 0.06 ± 0.01 O/Mo_{bulk}) is consistent with that reported by Ko and Madix[28] in which H_2 dissociation was found to be inhibited by oxygen adlayers on a Mo(100) surface as inferred from the flash desorption spectra for H_2 on fresh Mo(100) and oxygen-covered Mo(100) (up to 1 monolayer) surfaces.

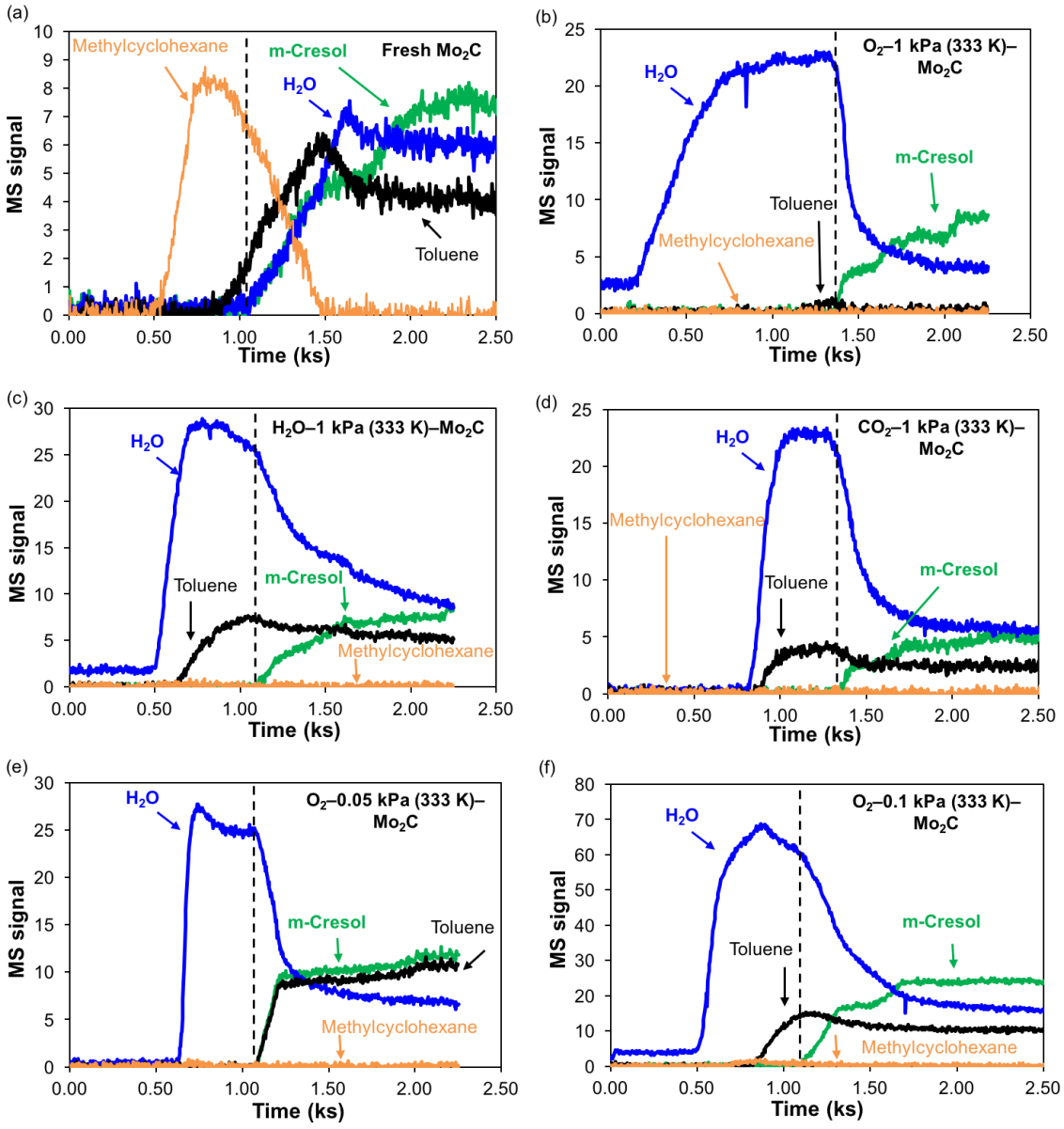

Figure 5.7 Transient mass spectrometer (MS) signals of m-cresol (m/z = 107), toluene (m/z = 92), methylcyclohexane (m/z = 83), H2O (m/z = 18) during m-cresol HDO on (a) fresh Mo_2C, (b) O_2–1 kPa (333 K)–Mo_2C, (c) H_2O–1 kPa (333 K)–Mo_2C, and (d) CO_2–1 kPa (333 K)–Mo_2C catalysts. Feed = m-cresol (1%)/ Ar (10%)/ H_2 (balance) (mol%) at ~ 107 kPa total pressure and at 423 K; total flow rate 1.83 $cm^3\ s^{-1}$; 1 g_{cat}.

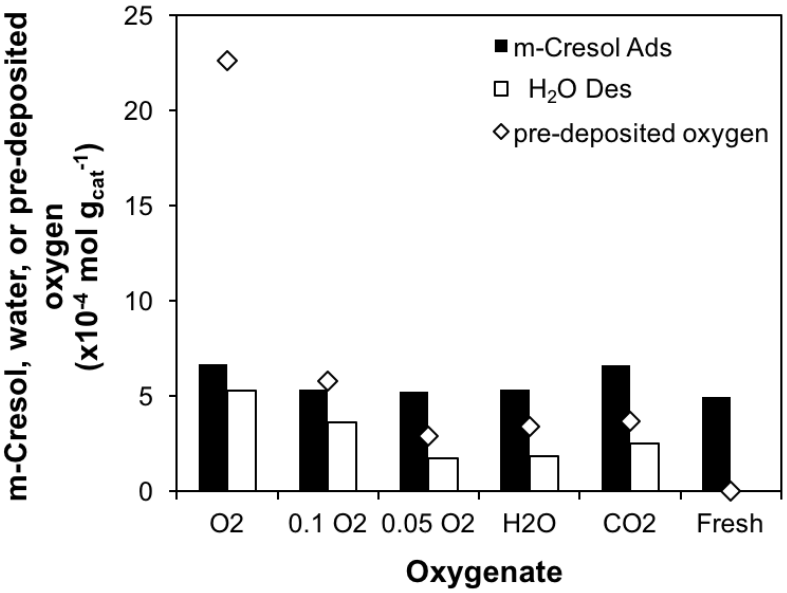

Figure 5.8 Amount of oxygen adsorbed on 1 g_{cat} of O_2–1 kPa (333 K)–Mo_2C, O_2–0.1 kPa (333 K)–Mo_2C, O_2–0.05 kPa (333 K)–Mo_2C, H_2O–1 kPa (333 K)–Mo_2C, CO_2–1 kPa (333 K)–Mo_2C, and fresh Mo_2C catalysts before m-cresol HDO (◇, pre-deposited oxygen); amount of m-cresol adsorbed (■), and amount of H_2O desorbed (□) during the transient of m-cresol HDO. Feed = m-cresol (1%)/ Ar (10%)/ H_2 (balance) (mol%) at ~107 kPa total pressure and at 423 K; total flow rate 1.83 $cm^3\ s^{-1}$; 1 g_{cat}.

We showed that O_2 can deposit approximately 0.04 O/Mo_{bulk} of oxygen on a fresh Mo_2C at 0.05 kPa treatment pressure whereas it requires 1 kPa of H_2O, CO_2, and m-cresol to achieve the same. We increased H_2O and CO_2 treatment pressures (5 – 6 kPa) and temperatures (333 K, 363 K, and 423 K) to investigate the amount of oxygen that H_2O and CO_2 can deposit under ambient pressure. The values of O/Mo_{bulk} before HDO on H_2O–5 kPa (423 K)–Mo_2C, CO_2–5 kPa (423 K)–Mo_2C, CO_2–6 kPa (363 K)–Mo_2C, and CO_2–6 kPa (333 K)–Mo_2C catalysts were found to be similar (Table 5.2, $O/Mo_{bulk} \sim 0.046 – 0.053$) and comparable to the amount of m-cresol adsorbed during the initial transient of m-cresol HDO (Figure 5.8, $\sim 0.06 \pm 0.01$ O/Mo_{bulk}). These results suggest that oxygenates like m-cresol, CO_2, and H_2O adsorb on the m-cresol adsorption site ($\sim 5.6 \times 10^{-4}$ mol g_{cat}^{-1}), presumably oxygen vacancy sites as discussed above, whereas O_2 can adsorb on oxygen

vacancy sites, metal-like sites, and other sites irrelevant to HDO, and can possibly be incorporated into the bulk structure.

Table 5.2 O/Mo_{bulk} before m-cresol HDO on H_2O-modified and CO_2-modified Mo_2C catalysts.

	H_2O–5 kPa (423 K)–Mo_2C	CO_2–5 kPa (423 K)–Mo_2C	CO_2–6 kPa (363 K)–Mo_2C	CO_2–6 kPa (333 K)–Mo_2C	CO_2–1 kPa (333 K)–Mo_2C
O/Mo_{bulk} before HDO	0.050 ± 0.004	0.046 ± 0.005	0.050 ± 0.002	0.053 ± 0.003	0.035 ± 0.010

5.5. Conclusions

Kinetics and in situ chemical titration studies on vapor phase m-cresol hydrodeoxygenation (HDO) showed that two distinct sites are required and metal-like sites are involved in toluene synthesis. m-Cresol HDO was used as a probe reaction to study the effect of oxygenate-modification on the metal-like function on Mo_2C. Oxygenate-modified Mo_2C catalysts, O_2–1 kPa (333 K)–Mo_2C, H_2O–1 kPa (333 K)–Mo_2C, and CO_2–1 kPa (333 K)–Mo_2C, were prepared by pretreating fresh Mo_2C catalysts in 1 kPa of O_2, CO_2, and H_2O at 333 K. The amount of adsorbed oxygen on these catalysts (O/Mo_{bulk}) was quantified using temperature-programmed surface reaction with H_2. The value of O/Mo_{bulk} before HDO on O_2–1 kPa (333 K)–Mo_2C (0.23 ± 0.02) is approximately 6 times higher than that on H_2O–1 kPa (333 K)–Mo_2C and CO_2–1 kPa (333 K)–Mo_2C (O/Mo_{bulk} before HDO ~ 0.036), demonstrating that molecular oxygen has a higher propensity to deposit oxygen on a fresh Mo_2C. The value of O/Mo_{bulk} after HDO was found to correlate with toluene synthesis rates, suggesting that the relevant surface environment for catalysis is the one that is measured under reaction conditions. A 10-fold decrease in toluene synthesis rates was observed on O_2–1 kPa (333 K)–Mo_2C compared to that on fresh Mo_2C, H_2O–1 kPa (333 K)–Mo_2C, and CO_2–1 kPa (333 K)–Mo_2C catalysts, however, turnover frequencies

of toluene synthesis measured from in situ CO titration on these samples are similar (~ 2.1×10^{-3} – 4.5×10^{-3} mol mol_{CO}^{-1} s^{-1}), indicating that adsorbed oxygen poisons the metal-like sites responsible for m-cresol. We demonstrated that the effect of adsorbed oxygen on toluene synthesis is agnostic to the source of oxygen, as inferred from in situ CO titration and m-cresol HDO reactions on O_2–0.05 kPa (333 K)–Mo_2C, H_2O–1 kPa (333 K)–Mo_2C, and CO_2–1 kPa (333 K)–Mo_2C catalysts. We also showed from transient mass spectrometry analysis that the amount of m-cresol adsorbed ~ 5.6×10^{-4} mol g_{cat}^{-1} (equivalent of ~ 0.06 ± 0.01 O/Mo_{bulk}) on fresh and oxygenate-modified Mo_2C catalysts is invariant with the amount of oxygen pre-deposited. These results suggest that the two distinct sites for m-cresol HDO are (i) metal-like sites for H_2 dissociation that can be poisoned by adsorbed oxygen and (ii) m-cresol adsorption sites that are independent of the amount of oxygen adsorbed.

5.6. Supporting information

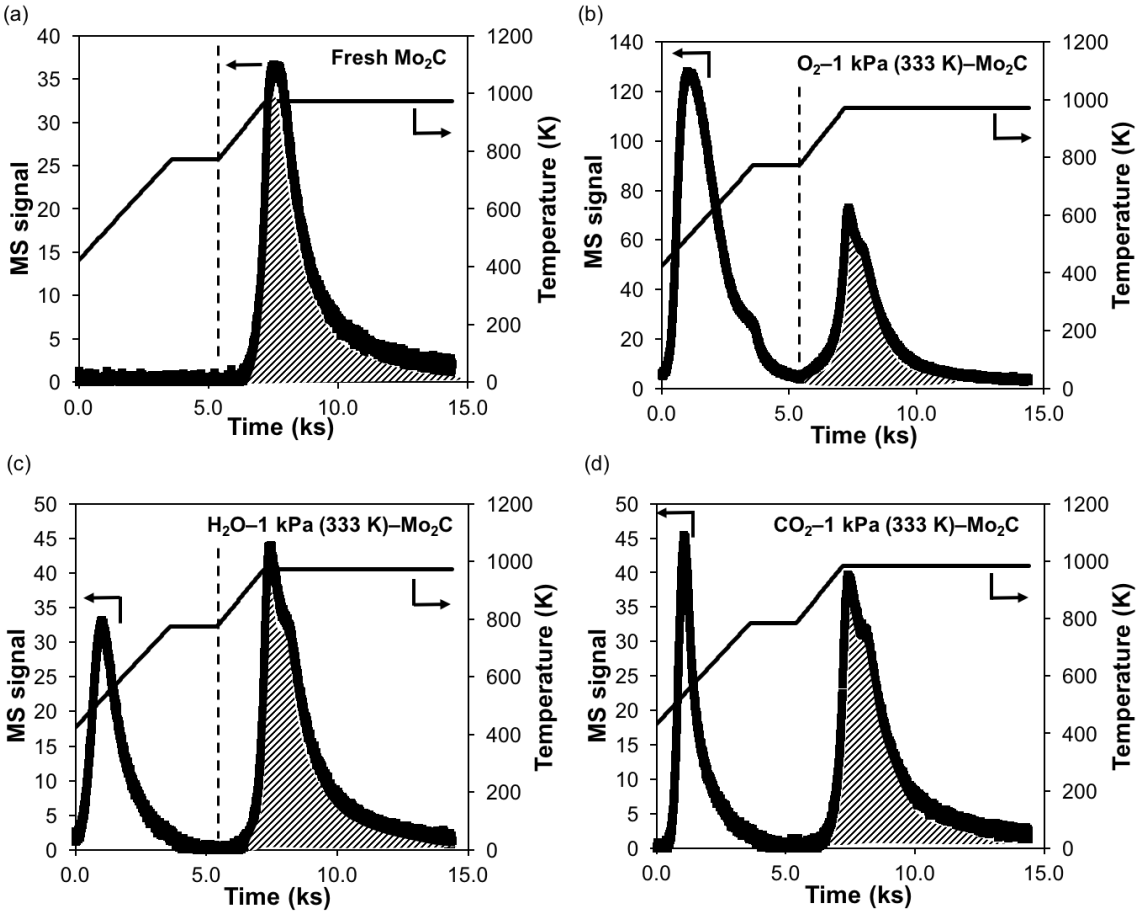

Figure 5.9 Temperature-programmed surface reaction with H_2 (TPSR) on (a) fresh Mo_2C, (b) O_2–1 kPa (333 K)–Mo_2C, (c) H_2O–1 kPa (333 K)–Mo_2C, and (d) CO_2–1 kPa (333 K)–Mo_2C catalysts, in which the sample was heated to 773 K in 1 h and held at 773 K for 0.5 h (white area), then heated to 973 K in 0.5 h and held at 973 K for 2 h (shaded area) in a flow of He (10%)/ H_2 (balance) (mol%) at a total flow rate of 1.83 $cm^3\ s^{-1}$ and at ambient pressure. An oxygenate treatment flow consisting of 1 kPa oxygenate (H_2O, CO_2, or O_2) in 1.67 $cm^3\ s^{-1}$ He was first introduced to a fresh Mo_2C catalyst for 2 h at 333 K and ambient pressure, which was subsequently heated to 423 K in 0.5 h and held at 423 K for 1.5 h in a flow of He (10%)/ H_2 (balance) (mol%) at a total flow rate of ~1.83 $cm^3\ s^{-1}$ and at ambient pressure.

Table 5.3 The values of O/Mo_{bulk} before HDO estimated from TPSR with H_2 at 773 K and TPSR with H_2 at 973 K on fresh and oxygenate-modified Mo_2C catalysts.

O/Mo_{bulk} before HDO	O_2–1 kPa (333 K)–Mo_2C	H_2O–1 kPa (333 K)–Mo_2C	CO_2–1 kPa (333 K)–Mo_2C	Fresh Mo_2C
TPSR at 773 K[a]	0.23 ± 0.02	0.038 ± 0.010	0.037 ± 0.010	0
TPSR at 973 K[b] and subtracting O/Mo_{bulk} = 0.07, the residual oxygen content on a freshly synthesized Mo_2C catalyst	0.25 ± 0.01	0.035 ± 0.010	0.039 ± 0.010	0

[a] The sample was heated to 773 K in 1 h and held at 773 K for 0.5 h in a flow of He (10%)/ H_2 (balance) (mol%) at a total flow rate of 1.83 $cm^3\ s^{-1}$ and at ambient pressure.

[b] The sample was heated to 773 K in 1 h and held at 773 K for 0.5 h, then heated to 973 K in 0.5 h and held at 973 K for 2 h in a flow of He (10%)/ H_2 (balance) (mol%) at a total flow rate of 1.83 $cm^3\ s^{-1}$ and at ambient pressure.

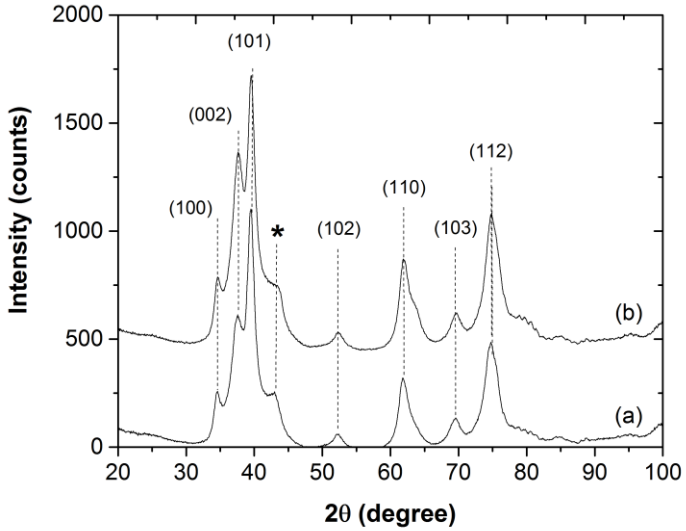

Figure 5.10 X-ray diffraction patterns of spent and passivated (a) O_2–1 kPa (333 K)–Mo_2C and (b) fresh Mo_2C from m-cresol HDO. (*) is the peak assignment for $MoO_xC_yH_z$.[25,205,206] The catalysts were passivated in 1% O_2/He at ~ 5.8 cm^3 s^{-1} for ~ 15 min at RT. Feed = m-cresol (1%)/ Ar (10%)/ H_2 (balance) (mol%) at ~ 107 kPa total pressure and at 423 K; total flow rate 1.83 cm^3 s^{-1}; 1 g_{cat}.

Table 5.4 X-ray photoelectron spectroscopy results for spent and passivated[c] fresh Mo_2C and O_2–1 kPa (333 K)–Mo_2C from vapor phase m-cresol HDO at 423 K.

Possible peak assignment[180,185,204]		Mo $3d_{5/2}$	Fresh Mo_2C (atom %)	O_2–1 kPa (333 K)–Mo_2C (atom %)
Mo^{3+}	Mo^{2+}	228.0 eV	62.8%	54.0%
Mo^{4+}	Mo^{3+}	229.1 eV	21.7%	19.3%
Mo^{6+}	Mo^{5+}	231.5 eV	15.5%	26.7%

[c] The spent catalysts were treated in 1% O_2/He at ~ 5.8 cm^3 s^{-1} for ~ 15 min at RT to passivate the pyrophoric Mo_2C.

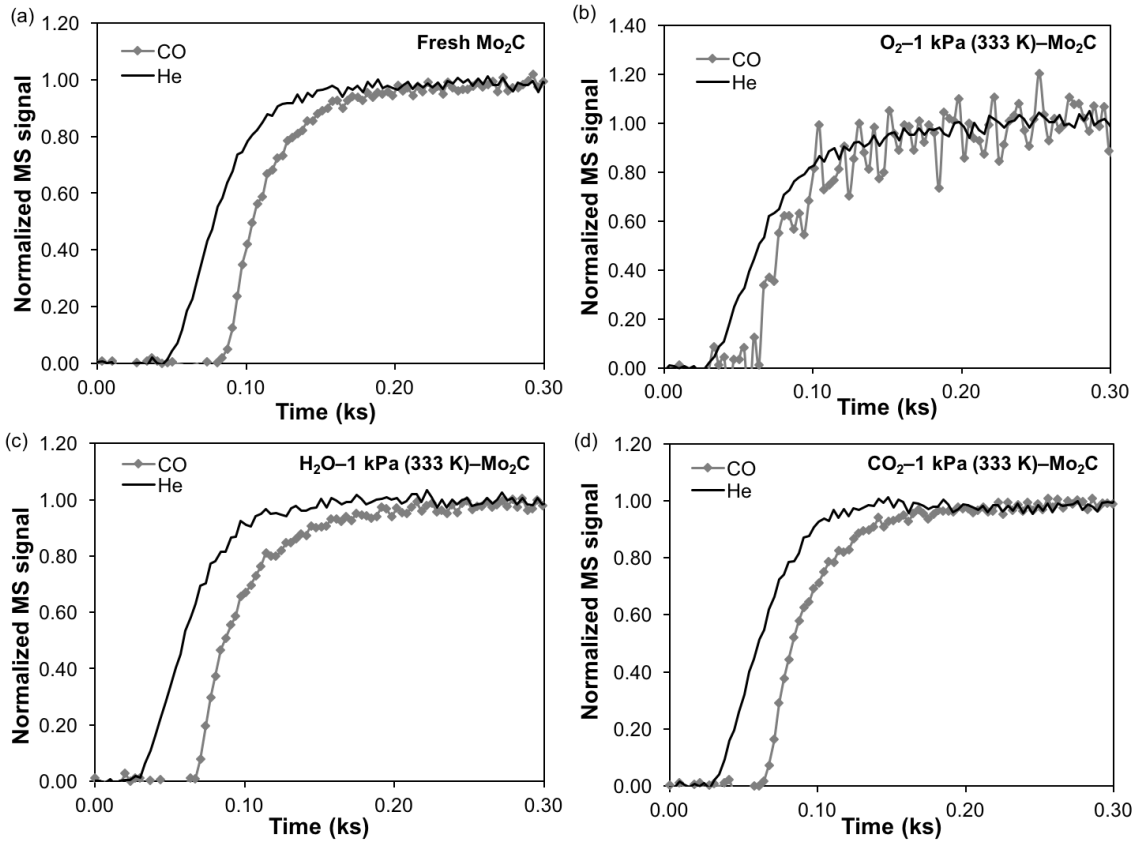

Figure 5.11 Typical transient spectrometric signals of helium and CO normalized to the signals at steady state as a function of time for in situ CO titration for m-cresol HDO on (a) fresh Mo_2C, (b) O_2–1 kPa (333 K)–Mo_2C, (c) H_2O–1 kPa (333 K)–Mo_2C, and (d) CO_2–1 kPa (333 K)–Mo_2C catalysts. Feed = m-cresol (1%)/ Ar (10%)/ H_2 (balance) (mol%) at ~ 107 kPa total pressure and at 423 K; total flow rate 1.83 $cm^3\ s^{-1}$; 1 g_{cat}. CO co-feed line: CO (0.5–0.93%)/ m-cresol (1%)/ He (10%)/ H_2 (balance) (mol%) at ~ 107 kPa total pressure and at 423 K; total flow rate 1.83 $cm^3\ s^{-1}$ (CO pressure for O_2–1 kPa (333 K)–Mo_2C catalyst is 0.05–0.07 kPa).

5.6. Acknowledgements

This research was supported by National Science Foundation Catalysis and Biocatalysis Program (CBET Award 1510661) Parts of this work were carried out in the Characterization Facility, University of Minnesota, which receives partial support from

NSF through the MRSEC program. We thank Ms. Seema Thakral for assistance with the X-ray diffraction and Bing Luo for X-ray photoelectron spectroscopy measurements.

Bibliography

1 J. S. Lee, S. Locatelli, S. T. Oyama and M. Boudart, *J. Catal.*, 1990, **125**, 157–170.

2 G. S. Ranhotra, A. T. Bell and J. A. Reimer, *J. Catal.*, 1987, **108**, 40–49.

3 C. Liu, M. Lin, K. Fang, Y. Meng and Y. Sun, *RSC Adv.*, 2014, **4**, 20948–20954.

4 H. Shou and R. J. Davis, *J. Catal.*, 2013, **306**, 91–99.

5 J. A. Schaidle and L. T. Thompson, *J. Catal.*, 2015, **329**, 325–334.

6 Y. Aoki, H. Tominaga and M. Nagai, *Catal. Today*, 2013, **215**, 169–175.

7 J.-S. Choi, G. Bugli and G. Djéga-Mariadassou, *J. Catal.*, 2000, **193**, 238–247.

8 G. S. Ranhotra, G. W. Haddix, A. T. Bell and J. A. Reimer, *J. Catal.*, 1987, **108**, 24–39.

9 C. Pham-Huu, M. J. Ledoux and J. Guille, *J. Catal.*, 1993, **143**, 249–261.

10 F. H. Ribeiro, M. Boudart, R. A. Dalla Betta and E. Iglesia, *J. Catal.*, 1991, **513**, 498–513.

11 E. Iglesia, J. E. Baumgartner, F. H. Ribeiro and M. Boudart, *J. Catal.*, 1991, **131**, 523–544.

12 F. H. Ribeiro, R. A. Dalla Betta, M. Boudart, J. Baumgartner and E. Iglesia, *J. Catal.*, 1991, **130**, 86–105.

13 P. C. K. Vesborg, B. Seger and I. Chorkendorff, *J. Phys. Chem. Lett.*, 2015, **6**, 951–957.

14 B. Sljukic, M. Vujkovic, L. Amaral, D. M. F. Santos, R. P. Rocha, C. A. C. Sequeira and J. L. Figueiredo, *J. Mater. Chem. A*, 2015, **3**, 15505–15512.

15 S. T. Hunt, T. Nimmanwudipong and Y. Román-Leshkov, *Angew. Chemie Int. Ed.*,

2014, **53**, 5131–5136.

16 S. K. Bej and L. T. Thompson, *Appl. Catal. A Gen.*, 2004, **264**, 141–150.

17 K. Xiong, W. Yu, D. G. Vlachos and J. G. Chen, *ChemCatChem*, 2015, **7**, 1402–1421.

18 K. Xiong, W. Yu and J. G. Chen, *Appl. Surf. Sci.*, 2014, **323**, 88–95.

19 H. Ren, W. Yu, M. Salciccioli, Y. Chen, Y. Huang, K. Xiong, D. G. Vlachos and J. G. Chen, *ChemSusChem*, 2013, **6**, 798–801.

20 J. Han, J. Duan, P. Chen, H. Lou, X. Zheng and H. Hong, *ChemSusChem*, 2012, **5**, 727–733.

21 J. Han, J. Duan, P. Chen, H. Lou, X. Zheng and H. Hong, *Green Chem.*, 2011, **13**, 2561.

22 S. A. W. Hollak, R. W. Gosselink, D. S. van Es and J. H. Bitter, *ACS Catal.*, 2013, **3**, 2837–2844.

23 R. W. Gosselink, D. R. Stellwagen and J. H. Bitter, *Angew. Chem. Int. Ed.*, 2013, **52**, 5089–5092.

24 A. L. Jongerius, R. W. Gosselink, J. Dijkstra, J. H. Bitter, P. C. A. Bruijnincx and B. M. Weckhuysen, *ChemCatChem*, 2013, **5**, 2964–2972.

25 T. Prasomsri, M. Shetty, K. Murugappan and Y. Román-Leshkov, *Energy Environ. Sci.*, 2014, **7**, 2660–2669.

26 S. Boullosa-Eiras, R. Lødeng, H. Bergem, M. Stöcker, L. Hannevold and E. A. Blekkan, *Catal. Today*, 2014, **223**, 44–53.

27 S. T. Oyama, *The Chemistry of Transition Metal Carbides and Nitrides*, London : Blackie Academic, 1996.

28 E. I. Ko and R. J. Madix, *Surf. Sci.*, 1981, **109**, 221–238.

29 A. L. Stottlemyer, T. G. Kelly, Q. Meng and J. G. Chen, *Surf. Sci. Rep.*, 2012, **67**, 201–232.

30 X.-R. Shi, S.-G. Wang, J. Hu, Z. Qin and J. Wang, *Surf. Sci.*, 2012, **606**, 1187–1194.

31 T. Wang, S. Wang, Y.-W. Li, J. Wang and H. Jiao, *J. Phys. Chem. C*, 2012, **116**, 6340–6348.

32 T. Wang, Y. W. Li, J. G. Wang, M. Beller and H. J. Jiao, *J. Phys. Chem. C*, 2014, **118**, 3162–3171.

33 T. Wang, Y.-W. Li, J. Wang, M. Beller and H. Jiao, *J. Phys. Chem. C*, 2014, **118**, 8079–8089.

34 T. Wang, Q. Luo, Y.-W. W. Li, J. Wang, M. Beller and H. Jiao, *Appl. Catal. A Gen.*, 2014, **478**, 146–156.

35 K. J. Leary, J. N. Michaels and M. Stacy, *J. Catal.*, 1986, **101**, 301–313.

36 E. Furimsky, *Appl. Catal. A Gen.*, 2000, **199**, 147–190.

37 C. Zhao, Y. Kou, A. A. Lemonidou, X. Li and J. A. Lercher, *Angew. Chem. Int. Ed.*, 2009, **48**, 3987–3990.

38 M. Saidi, F. Samimi, D. Karimipourfard, T. Nimmanwudipong, B. C. Gates and M. R. Rahimpour, *Energy Environ. Sci.*, 2014, **7**, 103–129.

39 H. Wang, J. Male and Y. Wang, *ACS Catal.*, 2013, **3**, 1047–1070.

40 J.-S. Choi, G. Bugli and G. Djéga-Mariadassou, in *12th International Congress on Catalysis: Proceedings of the 12th ICC, Granada, Spain, July 9-14, 2000*, eds. A. Corma, F. V. Melo, S. Mendioroz and J. L. G. Fierro, Elsevier, 2000, vol. 130, pp. 2885–2890.

41 J. S. Lee, S. T. Oyama and M. Boudart, *J. Catal.*, 1987, **106**, 125–133.

42 F. H. Ribeiro, R. A. Dalla Betta, G. J. Guskey and M. Boudart, *Chem. Mater.*, 1991, **3**, 805–812.

43 M. K. Neylon, S. Choi, H. Kwon, K. E. Curry and L. T. Thompson, *Appl. Catal. A Gen.*, 1999, **183**, 253–263.

44 L. Delannoy, J. M. Giraudon, P. Granger, L. Leclercq and G. Leclercq, *Catal. Today*, 2000, **59**, 231–240.

45 J. A. Schaidle, A. C. Lausche and L. T. Thompson, *J. Catal.*, 2010, **272**, 235–245.

46 B. M. Wyvratt, J. R. Gaudet and L. T. Thompson, *J. Catal.*, 2015, **330**, 280–287.

47 D. A. Ruddy, J. A. Schaidle, J. R. I. Ferrell, J. Wang, L. Moens and J. E. Hensley, *Green Chem.*, 2014, **16**, 454–490.

48 P. Liu and J. A. Rodriguez, *J. Phys. Chem. B*, 2006, **110**, 19418–19425.

49 A. J. Medford, A. Vojvodic, F. Studt, F. Abild-Pedersen and J. K. Nørskov, *J. Catal.*, 2012, **290**, 108–117.

50 H. Tominaga and M. Nagai, *J. Phys. Chem. B*, 2005, **109**, 20415–20423.

51 K. D. Sabnis, Y. Cui, M. C. Akatay, M. Shekhar, W.-S. Lee, J. T. Miller, W. N. Delgass and F. H. Ribeiro, *J. Catal.*, 2015, **331**, 162–171.

52 T. Namiki, S. Yamashita, H. Tominaga and M. Nagai, *Appl. Catal. A Gen.*, 2011, **398**, 155–160.

53 P. M. Mortensen, H. W. P. de Carvalho, J.-D. Grunwaldt, P. A. Jensen and A. D. Jensen, *J. Catal.*, 2015, **328**, 208–215.

54 W.-S. Lee, A. Kumar, Z. Wang and A. Bhan, *ACS Catal.*, 2015, **5**, 4104–4114.

55 C.-J. Chen, W.-S. Lee and A. Bhan, *Appl. Catal. A Gen.*, 2016, **510**, 42–48.

56 M. M. Sullivan, J. T. Held and A. Bhan, *J. Catal.*, 2015, **326**, 82–91.

57 J. Patt, D. J. Moon, C. Phillips and L. Thompson, *Catal. Letters*, 2000, **65**, 193–195.

58 J. D. Moon and J. W. Ryu, *Catal. Letters*, 2004, **92**, 2–9.

59 J.-S. Choi, V. Schwartz, E. Santillan-Jimenez, M. Crocker, S. Lewis, M. Lance, H. Meyer and K. More, *Catalysts*, 2015, **5**, 406–423.

60 H. Koempel and W. Liebner, in *Studies in Surface Science and Catalysis*, eds. M. S. Fábio Bellot Noronha and S.-A. Eduardo Falabella, Elsevier, 2007, vol. Volume 167, pp. 261–267.

61 F. J. Keil, *Microporous Mesoporous Mater.*, 1999, **29**, 49–66.

62 R. J. Quann, L. A. Green, S. A. Tabak and F. J. Krambeck, *Ind. Eng. Chem. Res.*, 1988, **27**, 565–570.

63 H. Pines, *The chemistry of catalytic hydrocarbon conversions*, New York: Academic Press, 1981.

64 S. Bessell and D. Seddon, *J. Catal.*, 1987, **105**, 270–275.

65 M. Guisnet, P. Andy, N. S. Gnep, E. Benazzi and C. Travers, *Oil Gas Sci. Technol.*, 1999, **54**, 23–28.

66 A. Corma and A. V Orchillés, *Microporous Mesoporous Mater.*, 2000, **35–36**, 21–30.

67 B. S. Greensfelder and H. H. Voge, *Ind. Eng. Chem.*, 1945, **37**, 1038–1043.

68 C. L. Thomas, *Ind. Eng. Chem.*, 1949, **41**, 2564–2573.

69 J. S. Buchanan, *Appl. Catal. A Gen.*, 1991, **74**, 83–94.

70 M. N. Mazar, S. Al-Hashimi, M. Cococcioni and A. Bhan, *J. Phys. Chem. C*, 2013, **117**, 23609–23620.

71 J. Weitkamp, P. A. Jacobs and J. A. Martens, *Appl. Catal. A Gen.*, 1983, **8**, 123–141.

72 J. S. Buchanan, J. G. Santiesteban and W. O. Haag, *J. Catal.*, 1996, **158**, 279–287.

73 M. V Frash, V. B. Kazansky, A. M. Rigby and R. A. van Santen, *J. Phys. Chem. B*,

1998, **102**, 2232–2238.

74 A. M. Rigby, G. J. Kramer and R. A. van Santen, *J. Catal.*, 1997, **170**, 1–10.

75 M. V Frash and R. A. van Santen, *Top. Catal.*, 1999, **9**, 191–205.

76 D. Lesthaeghe, J. Van der Mynsbrugge, M. Vandichel, M. Waroquier and V. Van Speybroeck, *ChemCatChem*, 2011, **3**, 208–212.

77 M. A. Natal-Santiago, R. Alcalá and J. A. Dumesic, *J. Catal.*, 1999, **181**, 124–144.

78 D. A. Simonetti, J. H. Ahn and E. Iglesia, *J. Catal.*, 2011, **277**, 173–195.

79 Y. V Kissin, *Catal. Rev.*, 2001, **43**, 85–146.

80 W. E. Garwood, American Chemical Society, Washington, DC , 1983, vol. 218, pp. 383–396.

81 S. Berend and L. M. M. Theo, *Nature*, 2008, **451**, 671–678.

82 S. W. Benson, *Thermochemical Kinetics; Methods for the Estimation of Thermochemical Data and Rate Parameters*, Wiley, New York, 1968.

83 I. Marsi, B. Viskolcz and L. Seres, *J. Phys. Chem. A*, 2000, **104**, 4497–4504.

84 N. Cohen and S. W. Benson, *Chem. Rev.*, 1993, **93**, 2419–2438.

85 S. W. Benson, *Chem. Rev.*, 1978, **78**, 23–35.

86 J. Kua, F. Faglioni and W. A. Goddard, *J. Am. Chem. Soc.*, 2000, **122**, 2309–2321.

87 M. Salciccioli, Y. Chen and D. G. Vlachos, *J. Phys. Chem. C*, 2010, **114**, 20155–20166.

88 M. Salciccioli, S. M. Edie and D. G. Vlachos, *J. Phys. Chem. C*, 2012, **116**, 1873–1886.

89 E. M. Fernández, P. G. Moses, A. Toftelund, H. A. Hansen, J. I. Martínez, F. Abild-

Pedersen, J. Kleis, B. Hinnemann, J. Rossmeisl, T. Bligaard and J. K. Nørskov, *Angew. Chemie Int. Ed.*, 2008, **47**, 4683–4686.

90 F. Abild-Pedersen, J. Greeley, F. Studt, J. Rossmeisl, T. R. Munter, P. G. Moses, E. Skúlason, T. Bligaard and J. K. Nørskov, *Phys. Rev. Lett.*, 2007, **99**, 16105.

91 C. M. Nguyen, B. A. De Moor, M. F. Reyniers and G. B. Marin, in *2nd International Workshop (NAPEN - 2011)*, Ghent University, Department of Chemical engineering and technical chemistry, Rodos, Greece, 2011, pp. 28–32.

92 C. M. Nguyen, B. A. De Moor, M. F. Reyniers and G. B. Marin, *J. Phys. Chem. C*, 2011, **115**, 23831–23847.

93 C. M. Nguyen, B. A. De Moor, M. F. Reyniers and G. B. Marin, *J. Phys. Chem. C*, 2012, **116**, 18236–18249.

94 B. A. De Moor, M. F. Reyniers, O. C. Gobin, J. A. Lercher and G. B. Marin, *J. Phys. Chem. C*, 2011, **115**, 1204–1219.

95 B. A. De Moor, M. F. Reyniers and G. B. Marin, *Phys. Chem. Chem. Phys.*, 2009, **11**, 2939–2958.

96 S. Rangarajan, A. Bhan and P. Daoutidis, *Comput. Chem. Eng.*, 2012, **45**, 114–123.

97 S. Rangarajan, A. Bhan and P. Daoutidis, *Comput. Chem. Eng.*, 2012, **46**, 141–152.

98 S. Rangarajan, A. Bhan and P. Daoutidis, *Ind. Eng. Chem. Res.*, 2010, **49**, 10459–10470.

99 M. K. Sabbe, F. De Vleeschouwer, M.-F. Reyniers, M. Waroquier and G. B. Marin, *J. Phys. Chem. A*, 2008, **112**, 12235–12251.

100 M. K. Sabbe, M. Saeys, M.-F. Reyniers, G. B. Marin, V. Van Speybroeck and M. Waroquier, *J. Phys. Chem. A*, 2005, **109**, 7466–7480.

101 S. S. Khan, X. Yu, J. R. Wade, R. D. Malmgren and L. J. Broadbelt, *J. Phys. Chem. A*, 2009, **113**, 5176–5194.

102 H. Chiang and A. Bhan, *J. Catal.*, 2010, **271**, 251–261.

103 R. J. Berger, J. Pérez-Ramírez, F. Kapteijn and J. A. Moulijn, *Chem. Eng. Sci.*, 2002, **57**, 4921–4932.

104 M. Vandichel, D. Lesthaeghe, J. Van der Mynsbrugge, M. Waroquier and V. Van Speybroeck, *J. Catal.*, 2010, **271**, 67–78.

105 Y. H. Guo, M. Pu, B. H. Chen and F. Cao, *Appl. Catal. A Gen.*, 2013, **455**, 65–70.

106 D. X. Liu, A. Bhan, M. Tsapatsis and S. Al Hashimi, *ACS Catal.*, 2011, **1**, 7–17.

107 H. S. Fogler, *Elements of Chemical Reaction Engineering*, Prentice Hall Professional Technical Reference, Upper Saddle River, NJ, 4th edn., 2006.

108 J. R. Welty and R. E. Welty, J. R.; Wicks, C. E.; Rorrer, G. L.; Wilson, *Fundamentals of Momentum, Heat, and Mass Transfer*, Chichester: Wiley, Hoboken, N.J., 5th edn., 2008.

109 E. Bird, R., Stewart, W., Lightfoot, *Transport phenomena (Rev. 2nd ed.)*, J. Wiley, New York, 2007.

110 W. O. Haag, R. M. Lago and P. B. Weisz, *Faraday Discuss. Chem. Soc.*, 1981, **72**, 317–330.

111 A. Bhan, R. Gounder, J. Macht and E. Iglesia, *J. Catal.*, 2008, **253**, 221–224.

112 R. N. Olcese, J. Francois, M. M. Bettahar, D. Petitjean and A. Dufour, *Energy Fuels*, 2013, **27**, 975–984.

113 S. Wan, T. Pham, S. Zhang, L. Lobban, D. Resasco and R. Mallinson, *AIChE J.*, 2013, **59**, 2275–2285.

114 V. K. Venkatakrishnan, W. N. Delgass, F. H. Ribeiro and R. Agrawal, *Green Chem.*, 2015, **17**, 178–183.

115 K. L. Deutsch and B. H. Shanks, *Appl. Catal. A Gen.*, 2012, **447**, 144–150.

116 R. J. Evans and T. A. Milne, *Energy Fuels*, 1987, **1**, 123–137.

117 T. Nimmanwudipong, R. C. Runnebaum, D. E. Block and B. C. Gates, *Energy Fuels*, 2011, **25**, 3417–3427.

118 P. T. M. Do, A. J. Foster, J. G. Chen and R. F. Lobo, *Green Chem.*, 2012, **14**, 1388–1397.

119 M. A. Gonzalez-Borja and D. E. Resasco, *Energy Fuels*, 2011, **25**, 4155–4162.

120 A. Ausavasukhi, Y. Huang, A. T. To, T. Sooknoi and D. E. Resasco, *J. Catal.*, 2012, **290**, 90–100.

121 S. K. Wu, P. C. Lai and Y. C. Lin, *Catal. Letters*, 2014, **144**, 878–889.

122 D. J. Rensel, S. Rouvimov, M. E. Gin and J. C. Hicks, *J. Catal.*, 2013, **305**, 256–263.

123 H. Y. Zhao, D. Li, P. Bui and S. T. Oyama, *Appl. Catal. A Gen.*, 2011, **391**, 305–310.

124 E. Shin and M. A. Keane, *Solutions*, 2000, **39**, 883–892.

125 C. Zhao, J. He, A. A. Lemonidou, X. Li and J. A. Lercher, *J. Catal.*, 2011, **280**, 8–16.

126 R. Olcese, M. M. Bettahar, B. Malaman, J. Ghanbaja, L. Tibavizco, D. Petitjean and A. Dufour, *Appl. Catal. B Environ.*, 2013, **129**, 528–538.

127 W.-S. Lee, Z. Wang, R. J. Wu and A. Bhan, *J. Catal.*, 2014, **319**, 44–53.

128 W.-S. Lee, Z. Wang, W. Zheng, D. G. Vlachos and A. Bhan, *Catal. Sci. Technol.*, 2014, **4**, 2340–2352.

129 E. a. Blekkan, C. Pham-Huu, M. J. Ledoux and J. Guille, *Ind. Eng. Chem. Res.*, 1994, **33**, 1657–1664.

130 L. Nie, P. M. de Souza, F. B. Noronha, W. An, T. Sooknoi and D. E. Resasco, *J. Mol. Catal. A Chem.*, 2014, **388–389**, 47–55.

131 J. M. Sun, A. M. Karim, H. Zhang, L. Kovarik, X. H. S. Li, A. J. Hensley, J. S. McEwen and Y. Wang, *J. Catal.*, 2013, **306**, 47–57.

132 J. S. Lee, M. H. Yeom, K. Y. Y. Park, I.-S. Nam, J. S. Chung, Y. G. Kim and S. H. Moon, *J. Catal.*, 1991, **128**, 126–136.

133 M.-L. Frauwallner, F. López-Linares, J. Lara-Romero, C. E. Scott, V. Ali, E. Hernández and P. Pereira-Almao, *Appl. Catal. A Gen.*, 2011, **394**, 62–70.

134 A. S. Mamède, J.-M. Giraudon, A. Löfberg, L. Leclercq and G. Leclercq, *Appl. Catal. A Gen.*, 2002, **227**, 73–82.

135 D. Mohan, C. U. Pittman and P. H. Steele, *Energy Fuels*, 2006, **20**, 848–889.

136 H. Yang, R. Yan, H. Chen, D. H. Lee and C. Zheng, *Fuel*, 2007, **86**, 1781–1788.

137 S. L. Shannon and J. G. Goodwin, *Chem. Rev.*, 1995, **95**, 677–695.

138 K. Xiong, W. S. Lee, A. Bhan and J. G. Chen, *ChemSusChem*, 2014, **7**, 2146–2149.

139 S. H. Pang and J. W. Medlin, *ACS Catal.*, 2011, **1**, 1272–1283.

140 A. H. Zacher, M. V Olarte, D. M. Santosa, D. C. Elliott and S. B. Jones, *Green Chem.*, 2014, **16**, 491–515.

141 T. V. Choudhary and C. B. Phillips, *Appl. Catal. A Gen.*, 2011, **397**, 1–12.

142 S. Sitthisa and D. E. Resasco, *Catal. Letters*, 2011, **141**, 784–791.

143 A. D. Sutton, F. D. Waldie, R. Wu, M. Schlaf, L. A. Silks and J. C. Gordon, *Nat. Chem.*, 2013, **5**, 428–432.

144 S. K. Kim, D. Yoon, S.-C. Lee and J. Kim, *ACS Catal.*, 2015, **5**, 3292–3303.

145 M. M. Nair, S. Kaliaguine and F. Kleitz, *ACS Catal.*, 2014, **4**, 3837–3846.

146 D. Gu, C.-J. Jia, C. Weidenthaler, H.-J. Bongard, B. Spliethoff, W. Schmidt and F. Schüth, *J. Am. Chem. Soc.*, 2015, **137**, 11407–11418.

147 T. Grewe, X. Deng, C. Weidenthaler, F. Schüth and H. Tüysüz, *Chem. Mater.*, 2013, **25**, 4926–4935.

148 T. Brezesinski, J. Wang, S. H. Tolbert and B. Dunn, *Nat. Mater.*, 2010, **9**, 146–151.

149 Y. Shi, Y. Wan and D. Zhao, *Chem. Soc. Rev.*, 2011, **40**, 3854–3878.

150 Y. Ren, Z. Ma and P. G. Bruce, *Chem. Soc. Rev.*, 2012, **41**, 4909–4927.

151 B. T. Yonemoto, G. S. Hutchings and F. Jiao, *J. Am. Chem. Soc.*, 2014, **136**, 8895–8898.

152 L. Borchardt, M. Oschatz, S. Graetz, M. R. Lohe, M. H. Rümmeli and S. Kaskel, *Microporous Mesoporous Mater.*, 2014, **186**, 163–167.

153 X. Cui, X. Zhou, H. Chen, Z. Hua, H. Wu, Q. He, L. Zhang and J. Shi, *Int. J. Hydrogen Energy*, 2011, **36**, 10513–10521.

154 C.-H. Huang, D. Gu, D. Zhao and R.-A. Doong, *Chem. Mater.*, 2010, **22**, 1760–1767.

155 F. Kleitz, S. H. Choi and R. Ryoo, *Chem. Commun.*, 2003, 2136–2137.

156 D. C. LaMont, A. J. Gilligan, A. R. . Darujati, A. S. Chellappa and W. J. Thomson, *Appl. Catal. A Gen.*, 2003, **255**, 239–253.

157 C. O. Preiss, H., B. Meyer, *J. Mater. Sci.*, 1998, 33, 713–722.

158 B. Ravel and M. Newville, *J. Synchrotron Radiat.*, 2005, **12**, 537–541.

159 Y. Ren, F. Jiao and P. G. Bruce, *Microporous Mesoporous Mater.*, 2009, **121**, 90–94.

160 Q. Lu, Y. Chen, W. Li, J. G. Chen, J. Q. Xiao and F. Jiao, *J. Mater. Chem. A*, 2013, **1**, 2331–2336.

161 J. Rosen, G. S. Hutchings and F. Jiao, *J. Am. Chem. Soc.*, 2013, **135**, 4516–4521.

162 F. Jiao, A. H. Hill, A. Harrison, A. Berko, A. V Chadwick and P. G. Bruce, *J. Am. Chem. Soc.*, 2008, **130**, 5262–5266.

163 W.-F. Chen, S. Iyer, S. Iyer, K. Sasaki, C.-H. Wang, Y. Zhu, J. T. Muckerman and E. Fujita, *Energy Environ. Sci.*, 2013, **6**, 1818.

164 W.-F. Chen, C.-H. Wang, K. Sasaki, N. Marinkovic, W. Xu, J. T. Muckerman, Y. Zhu and R. R. Adzic, *Energy Environ. Sci.*, 2013, **6**, 943–951.

165 J. G. Chen, *Chem. Rev.*, 1996, **96**, 1477–1498.

166 H. Shou and R. J. Davis, *J. Catal.*, 2011, **282**, 83–93.

167 G. Wang, J. A. Schaidle, M. B. Katz, Y. Li, X. Pan and L. T. Thompson, *J. Catal.*, 2013, **304**, 92–99.

168 J. Chang, T. Danuthai, S. Dewiyanti, C. Wang and A. Borgna, *ChemCatChem*, 2013, **5**, 3041–3049.

169 K. Oshikawa, M. Nagai and S. Omi, *J. Phys. Chem. B*, 2001, **105**, 9124–9131.

170 D. A. Gómez-Gualdrón and P. B. Balbuena, *Nanotechnology*, 2009, **20**, 215601.

171 G. Ramírez-Caballero, J. Burgos and B. Perla, *J. Phys. Chem. C*, 2009, 15658–15666.

172 J. S. Lee and M. Boudart, *Catal. Letters*, 1993, **20**, 97–106.

173 J. H. Sinfelt and D. J. C. Yates, *Nat. Phys. Sci.*, 1971, **229**, 27–28.

174 I. Kojima, E. Miyazaki, Y. Inoue and I. Yasumori, *J. Catal.*, 1979, **59**, 472–474.

175 C. Márquez-Alvarez, J. B. Calridge, A. P. E. York, J. Sloan and M. L. H. Green, in *Hydrotreatment and Hydrocracking of Oil FractionsProceedings of the 1st International Symposium/6th European Workshop*, ed. B. D. and P. G. B. T.-S. in S. S. and C. G.F. Froment, Elsevier, 1997, vol. Volume 106, pp. 485–490.

176 D. R. Stellwagen and J. H. Bitter, *Green Chem.*, 2015, **17**, 582–593.

177 H. Tominaga and M. Nagai, *Bull. Chem. Soc. Jpn.*, 2010, **83**, 1501–1503.

178 G. DeMaria, R. P. Burns, J. Drowart and M. G. Inghram, *J. Chem. Phys.*, 1960, **32**, 1373–1377.

179 P. Grathwohl, *Diffusion in Natural Porous Media : Contaminant Transport, Sorption/Desorption and Dissolution Kinetics*, Kluwer Academic, Boston, 1998.

180 J. A. Schaidle, J. Blackburn, C. A. Farberow, C. Nash, K. X. Steirer, J. Clark, D. J. Robichaud and D. A. Ruddy, *ACS Catal.*, 2016, **6**, 1181–1197.

181 A. L. Jongerius, P. C. A. Bruijnincx and B. M. Weckhuysen, *Green Chem.*, 2013, **15**, 3049–3056.

182 Q. Lu, C.-J. Chen, W. W. Luc, J. G. Chen, A. Bhan and F. Jiao, *ACS Catal.*, 2016, **6**, 3506–3514.

183 W. Wu, Z. Wu, C. Liang, P. Ying, Z. Feng and C. Li, *Phys. Chem. Chem. Phys.*, 2004, **6**, 5603–5608.

184 T. P. St. Clair, S. T. Oyama, D. F. Cox, S. Otani, Y. Ishizawa, R.-L. Lo, K. Fukui and Y. Iwasawa, *Surf. Sci.*, 1999, **426**, 187–198.

185 L. Óvári, J. Kiss, A. P. Farkas and F. Solymosi, *J. Phys. Chem. B*, 2005, **109**, 4638–4645.

186 Y. Hong, H. Zhang, J. Sun, K. M. Ayman, A. J. R. Hensley, M. Gu, M. H. Engelhard, J. S. McEwen and Y. Wang, *ACS Catal.*, 2014, **4**, 3335–3345.

187 Q. Sun, G. Chen, H. Wang, X. Liu, J. Han, Q. Ge and X. Zhu, *ChemCatChem*, 2016, **8**, 551–561.

188 X. Zhu, L. Nie, L. L. Lobban, R. G. Mallinson and D. E. Resasco, *Energy Fuels*, 2014, **28**, 4104–4111.

189 A. Foster, P. M. Do and R. Lobo, *Top. Catal.*, 2012, **55**, 118–128.

190 M. Shetty, K. Murugappan, T. Prasomsri, W. H. Green and Y. Román-Leshkov, *J. Catal.*, 2015, **331**, 86–97.

191 M. B. Griffin, G. A. Ferguson, D. A. Ruddy, M. J. Biddy, G. T. Beckham and J. A. Schaidle, *ACS Catal.*, 2016, 2715–2727.

192 B. Hammer, Y. Morikawa and J. Nørskov, *Phys. Rev. Lett.*, 1996, **76**, 2141–2144.

193 J. A. Rodriguez and D. W. Goodman, *Science*, 1992, **257**, 897–903.

194 K. Edamoto, M. Sugihara, K. Ozawa and S. Otani, *Surf. Sci.*, 2004, **561**, 101–109.

195 X.-R. Shi, S.-G. Wang and J. Wang, *J. Mol. Catal. A Chem.*, 2016, **417**, 53–63.

196 E. Iglesia, F. H. Ribeiro, M. Boudart and J. E. Baumgartner, *Catal. Today*, 1992, **15**, 307–337.

197 M. D. Porosoff, X. Yang, J. A. Boscoboinik and J. G. Chen, *Angew. Chem. Int. Ed.*, 2014, **53**, 6705–6709.

198 I. Barin, *Thermochemical Data of Pure Substances*, Weinheim, Federal Republic of Germany; New York, N.Y., USA: VCH, 1989.

199 I. Barin and O. Knacke., *Thermochemical Properties of Inorganic Substances*, Springer-Verlag, New York, 1973.

200 M. M. Sullivan, C.-J. Chen and A. Bhan, *Catal. Sci. Technol.*, 2016, **6**, 602–616.

201 D. J. Sajkowski and S. T. Oyama, *Appl. Catal. A Gen.*, 1996, **134**, 339–349.

202 T. Prasomsri, T. Nimmanwudipong and Y. Román-Leshkov, *Energy Environ. Sci.*, 2013, **6**, 1732–1738.

203 A. V. Mironenko and D. G. Vlachos, *J. Am. Chem. Soc.*, 2016, **138**, 8104–8113.

204 J. G. Choi and L. T. Thompson, *Appl. Surf. Sci.*, 1996, **93**, 143–149.

205 C. Bouchy, C. Pham-Huu, B. Heinrich, C. Chaumont and M. J. Ledoux, *J. Catal.*, 2000, **190**, 92–103.

206 C. Bouchy, C. Pham-Huu, B. Heinrich, E. G. Derouane, S. B. Derouane-Abd Hamid

and M. J. Ledoux, *Appl. Catal. A Gen.*, 2001, **215**, 175–184.

Appendix A

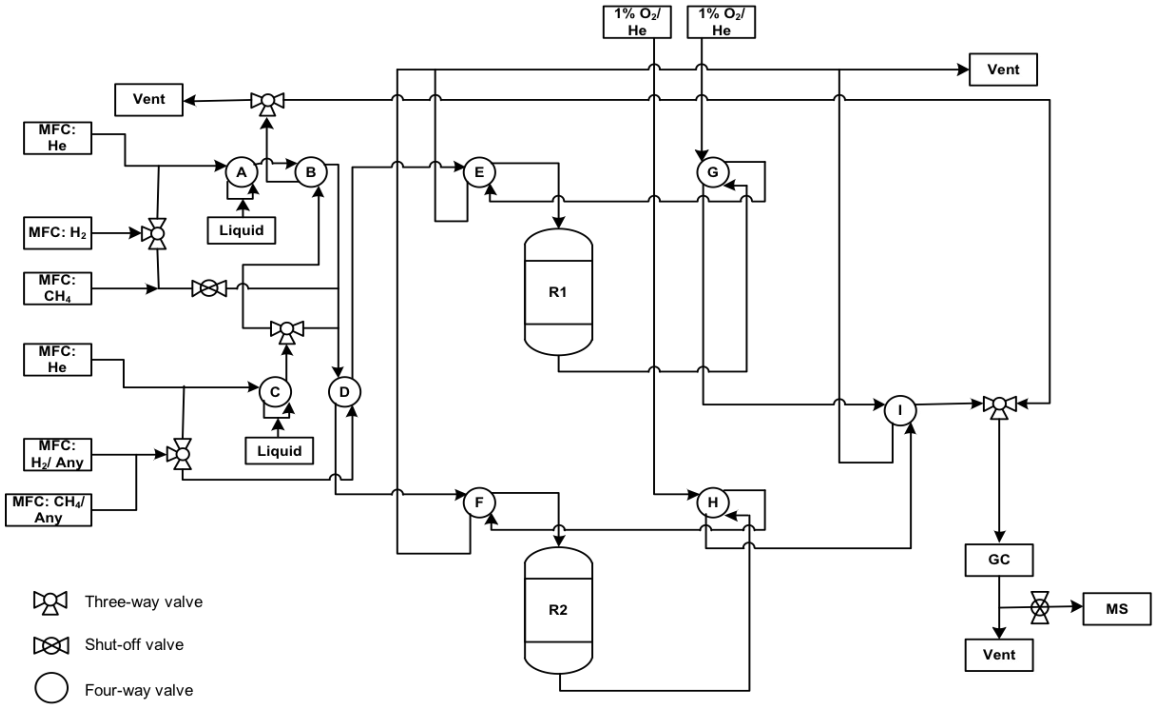

Scheme A.1 A schematic of the reactor unit used for the HDO studies in this work.